Investigation on the THM Behavior of a Heated Bentonite Barrier by Measurements and Numerical Calculations

- MUSTER -

Final Report

DBE TECHNOLOGY GmbH

The reported research work has been funded by the Federal Ministry of Economics and Technology (BMWi = Bundesministerium für Wirtschaft und Technologie) under the contract No. FKZ 02E 9743. However, the authors are responsible for all the content.

TABLE OF CONTENTS

ACKNOWLEDGEMENTS

Special thanks go to the French National Radioactive Waste Management Agency (ANDRA, Project Leader; Michel de Combarieu) for giving an opportunity to participate in the experiment TBT (Temperature Buffer Test) and thanks go to Clay Technology for providing all necessary data and compacted bentonite samples, and also for hosting the monitoring system.

EXECUTIVE SUMMARY

This report contains the results of the research and development activities performed between 01.08.2003 and 30.06.2008 in the framework of the research project:

“ Investigation on the Thermal, Hydraulic and Mechanic (THM) Behavior of the Bentonite Barrier by Measurements and Numerical Calculations” - MUSTER

This work focused on the Temperature Buffer Test (TBT). The experiment is a heating test operated by ANDRA and SKB with the scale 1:1 consisting of two canisters installed in a short vertical borehole in granite in the ÄSPÖ Hard Rock Laboratory Sweden. The canister below is covered by bentonite, the upper one with sand layer and with bentonite respectively. The ongoing THM processes were extensively monitored with sensors for measurements of temperature, capillary pressure, total pressure, pore water pressure and relative humidity. For evaluation purposes a few fiber optic sensors have been installed by DBE Technology in two measurement levels since they have never been tested under such a strong thermal load (>150°C). Three-quarter of the sensors failed in the period of 5 years. Being installed in a strong temperature gradient, the temperature compensation of the pressure signal caused significant problems and some doubts in the absolute accuracy are still remaining.

Results of laboratory tests on the bentonite used as a buffer are presented. Thermo-physical properties of MX-80 bentonite samples such as thermal conductivity, specific heat capacity, thermal diffusivity and thermal expansion have been analyzed and applied for further modeling work. The empirical formulations indicate that the water content and temperature development has strong influence on these properties especially on thermal expansion (shrinkage).

The code TOUGH2 (Transport of Unsaturated Groundwater and Heat) was applied to calculate the TH (thermo-hydraulic) coupled two-phase flow in bentonite whereas a good fit of calculated and measured temperature and suction values has been achieved and for hydraulic and thermal calculations plausible parameter sets have been obtained so far. The TH coupled calculations were performed by means of simplified axisymmetric 2D (quasi 3D) model. Suction controlled saturation process is simulated by using van Genuchten`s formula and thermal conductivity is determined as a function of temperature and water content. Good fits between measured and computed temperature values around both heaters have been obtained. Subsequent to thermal calculations, the thermal-only calibrated model was selected as an initial model for hydraulic analyses and approximately two hundred and thirty simulations were performed. In the framework of sensitivity analyses, the hydraulic parameters related to capillary pressure were used in order to calibrate the results of simulations with the in-situ data. Finally, for suction the most sensitive parameters were obtained, these are; saturation of the liquid phase S_L, Van Genuchten`s notation m and intrinsic permeability along the x direction k_x in turn. For different distances to the heaters, suitable fittings of the simulated and the observed capillary pressure values were obtained by using designated statistical methods. Finally, it can be concluded that participating in the modeling work of the TBT yields a significant increase of understanding the processes of water and heat flow in compacted bentonite.

1 INTRODUCTION AND OBJECTIVES

At the Äspö Hard Rock Laboratory (HRL) in Sweden, experiments are currently performed to investigate final disposal of heat generating waste under real conditions. The Temperature Buffer Test (TBT) is a joint project between SKB/ANDRA, the latter has the lead, and DBE Tec (on behalf of BMWi in the framework of the Swedish-German agreement on research in the HRL Äspö. The TBT aims at investigating the behavior of a bentonite buffer under a thermal load of up to 200°C, during the water saturation process and over a time period of 5 to 10 years. The thermal impact is recorded by a huge amount of geotechnical instrumentation as a basis for detailed evaluation. This is the first test of a bentonite barrier under a thermal load of more than 100°C using both pure bentonite and a sand-bentonite layered buffer construction. A full scale deposition hole at the HRL in Äspö is used for the experiment. An important part of the work is to measure the thermal, hydraulic and mechanical processes in the bentonite during the saturation and afterwards.

In order to characterize the thermal behavior of the bentonite at more than 100°C (up to 200°C), measurements by geotechnical instrumentation and laboratory investigations are performed. The geotechnical instrumentation consists of different sensors measuring total pressure, pore water pressure, relative humidity, suction and temperature to analyze the relevant physical processes. The use of special sensor material was necessary due to the high temperatures and the corrosive environment. Since under these conditions fiber optic sensors have never been implemented before, a few optical pressure and temperature sensors have been installed for evaluation purposes. Moreover these sensors are used to obtain plausible temperature and pressure measurements near to the heaters. In the following chapters evaluation results from fiber optic sensors were presented and discussed in comparison with other sensors. Laboratory and literature investigations on samples from Äspö are done to identify and observe the material properties of compacted MX-80 bentonite, Äspö diorite and sand. These parameters are used as an input for further modeling works.

All measurements are accompanied by numerical calculations and statistical methods to simulate the relevant physical processes and to determine the material parameters by fitting the calculation and measurement results. The main focus is put on the analysis of the material behaviors as a response to the high thermal load over longer periods of time. Back analyses of thermal and hydraulic processes are performed to obtain an acceptable fittings between in-situ and computed values.

As a summary, the thermal behavior of the bentonite MX-80 under thermal load ranging 100°C to 200°C is determined by laboratory investigations. Following this, temperature and suction data from related sensors are gathered and beside fiber optic sensor data results are analyzed. All these in-situ data from corresponding sensors are modified in order to generate a model then, for suction and temperature data plausible calibration results between model outputs and in-situ measurements are obtained by using statistical methods mentioned in the following chapters. The results are intended to give a contribution to the evaluation whether heat generating waste can be disposed of much earlier as currently assumed for granite host rock by exceeding the 100°C temperature criterion.

2 THE TEMPERATURE BUFFER TEST (TBT)

2.1 Location and experimental design

The Temperature Buffer Test simulates a part of a repository for heat generating waste and is carried out in the Äspö Hard Rock Laboratory. An overview regarding the whole installation of the TBT is given in Figure 2-1.

Two canisters have been placed in a deposition borehole of 8.0 m depth and 1.75 m borehole diameter (see Figure 2-1). The material of the French canisters is not copper as foreseen in the Swedish concept but carbon steel. The wall thickness is 50 millimeters. The canisters are much smaller than the Swedish ones and they are 3000 mm in length and 610 mm in diameter. They are equipped with heating elements simulating the heat generation of radioactive waste decay and heated with 1500 W so that the temperature on the canister surface exceeds more than 100°C. Thermocouples are placed inside the canisters and on the surface for continuous temperature measurement.

According to ÅKESSON et al. (2007b) measuring systems and transducers work well and except some relative humidity sensors, almost all of them deliver reliable values.

Two different buffer designs are considered: The lower canister is covered by a bentonite buffer and the upper canister is first covered by a sand buffer in order to reduce the temperature load on the outer bentonite cover. The bentonite used in the TBT is MX-80. This bentonite is commercial clay containing about 80% montmorillonite and 20% other minerals.

To facilitate the supply of water, the slot between the wall of the deposition hole and the buffer is filled with compacted sand and works as a filter. Titanium water tubes equipped with filter tips are installed in the sand on two levels, 250 and 6750 mm from bottom (four at each level). An artificial water pressure is applied within this slot and the filling is completed after 60 – 80 days (ÅKESSON et al. 2007b).

The demands on the bentonite buffer are to serve as mechanical support for the canister, to reduce the effects of a possible rock displacement on the canister and to minimize water flow through the deposition holes and in direction to the canister.

The buffer material is instrumented with pressure cells (total and water pressure), temperature sensors and moisture (relative humidity) gauges. By this instrumentation the temperature distribution, the progress of water saturation and the build-up of swelling pressure in the bentonite can be measured. Temperature sensors are also installed in the rock.

Measurements are performed in 7 measuring sections placed at different levels. The bentonite blocks are called cylinders and rings. The cylinders are numbered C1-C4 and the rings R1-R12, respectively (see Figure 2-1). On each level, sensors are placed in different directions. The angle in the defined coordinate system is described counter-clockwise from the direction A. The z-coordinate is counted from the bottom of the deposition hole.

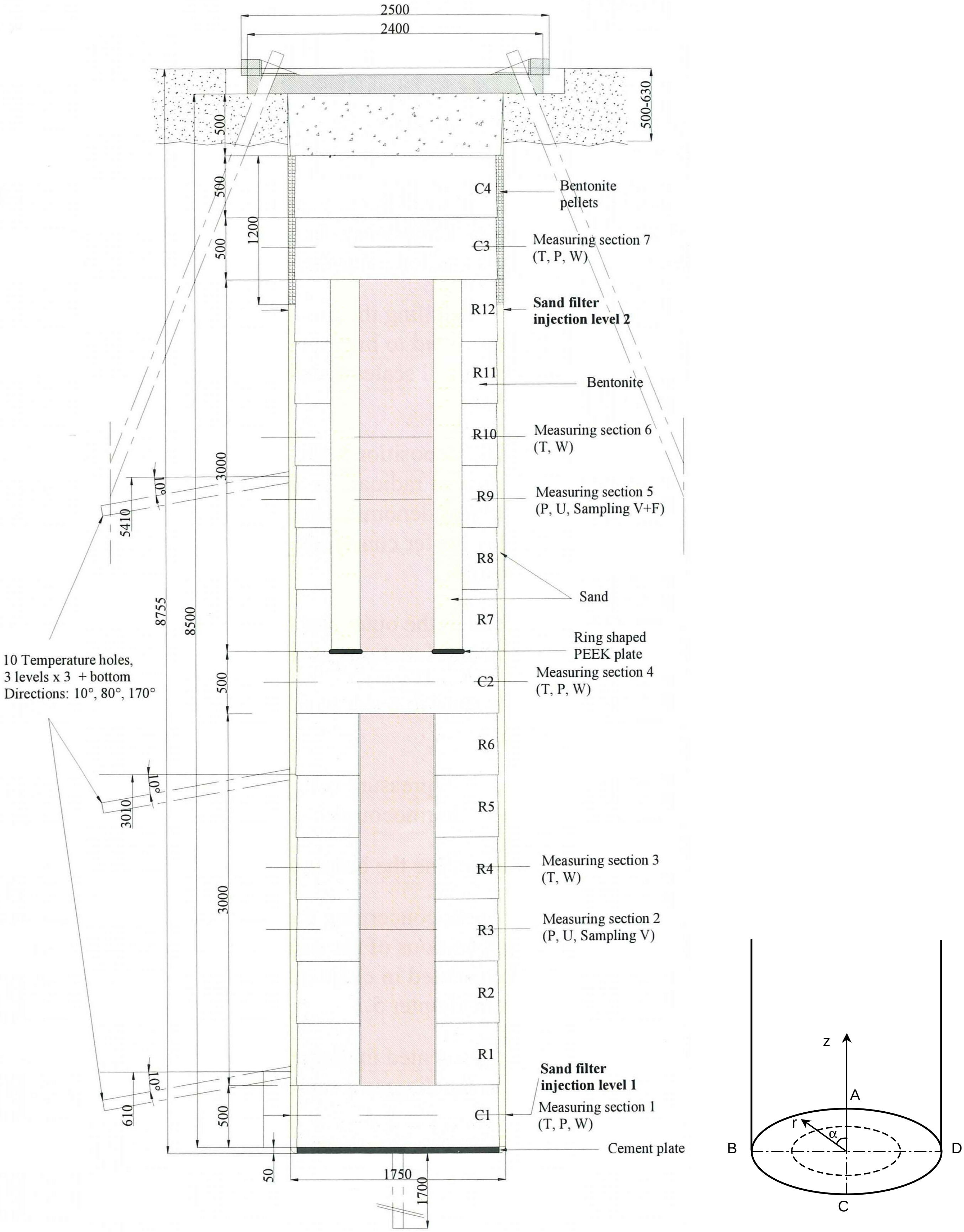

Figure 2-1 Schematic illustration showing the experiment layout and coordinate system, the lower heater is denominated as No.1 and the upper as No.2 (ÅKESSON et al. 2007b)

A list of selected sensors considered for numerical investigations and their positions are given in Table 2-1 and in Appendix-1. Sensors used in the hydraulic calibration are shown in Appendices 3 to 8. Every sensor is entitled with a unique name consisting of two letters describing the type of measurement (T=temperature, P=total pressure, U=pore pressure, W=water content) and the location (B=bentonite). The position is described within three coordinates according to the coordinate system of Figure 2-1. The r-coordinate is the horizontal distance from the center of the hole; the z-coordinate is the height from the bottom of the hole and α is the angle of the coordinate system.

The heating of both canisters started with an initially applied constant power of 900 W on the 26.03.03. The power was raised to 1200 W on the 03.04.03. The power was further raised to 1500 W on 10.04.03. Several power failures have occurred so far. Finally, the power was raised to 1600 W on the 09.06.06 (ÅKESSON et al. 2007b). The power output for both of the heaters can be found in Figure 2-2. It should be considered that Figure 2-2 shows the power output data only with main failures.

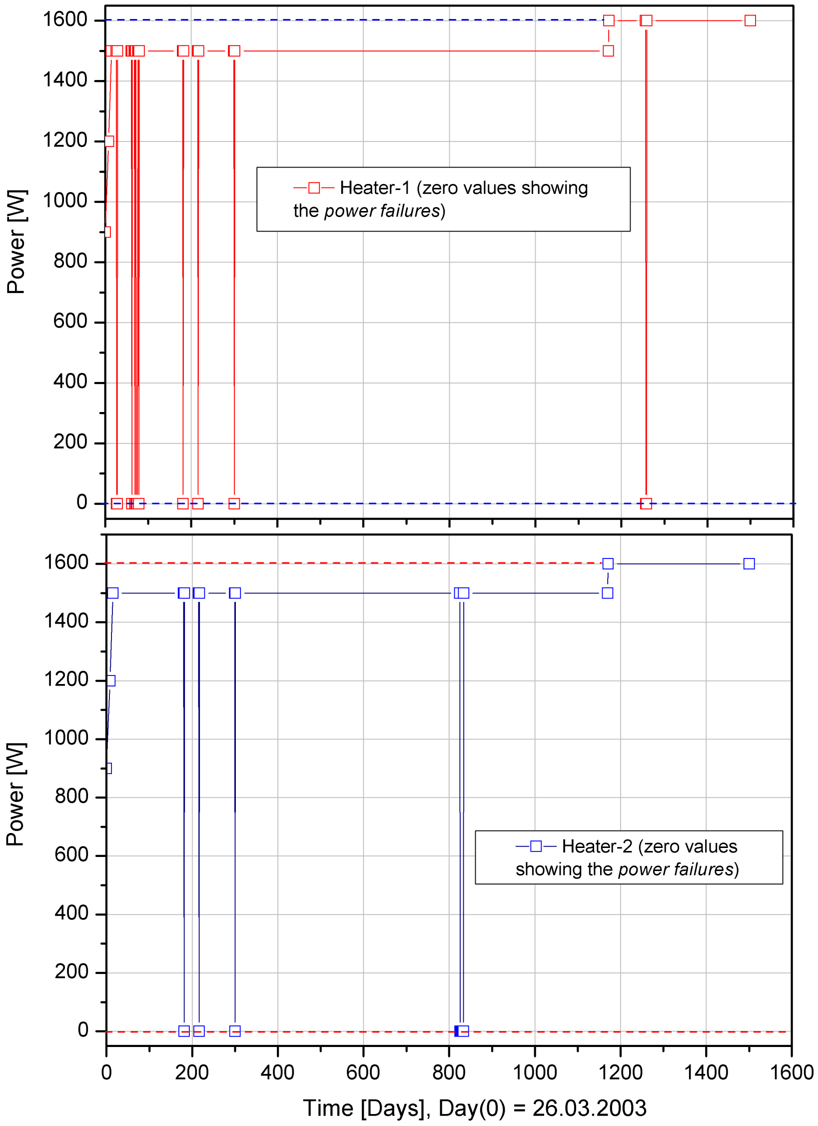

Figure 2-2 **In-situ power output graphs for heater-1 and heater-2**

Table 2-1: Numbering and positions of the instruments in TBT Experiment (ÅKESSON et al. 2007b)

Mark	Measuring section	Block	α - Degree	r [mm]	z [mm]	Direction of measurement / Remark
PB204	2	Ring 3	250	420	1950	Total pressure radial
PB205	2	Ring 3	290	420	2000	Total pressure axial
PB206	2	Ring 3	8	535	1950	Total pressure radial
PB207	2	Ring 3	20	535	1950	Total pressure tangential
PB208	2	Ring 3	45	585	2000	Total pressure axial
PB209	2	Ring 3	100	635	1950	Total pressure tangential
PB210	2	Ring 3	170	710	1950	Total pressure tangential
PB211	2	Ring 3	180	710	1950	Total pressure radial
PB212	2	Ring 3	260	748	2000	Total pressure axial
PB213	2	Ring 3	270	875	1950	Total pressure radial on the rock
PB217	5	Ring 9	270	535	5450	Total pressure radial, against sand
PB218	5	Ring 9	340	635	5500	Total pressure axial
PB219	5	Ring 9	0	635	5450	Total pressure radial
PB220	5	Ring 9	20	635	5450	Total pressure tangential
PB221	5	Ring 9	70	710	5500	Total pressure axial
PB222	5	Ring 9	110	710	5450	Total pressure radial
PB223	5	Ring 9	160	745	5500	Total pressure axial
PB224	5	Ring 9	180	770	5450	Total pressure radial
PB225	5	Ring 9	200	740	5450	Total pressure tangential
PB226	5	Ring 9	270	875	5450	Total pressure radial on the rock
PB230a	2	Ring 3	180	376	1950	Fiber optic total pressure sensor / radial
PB230b	2	Ring 3	180	428	1950	Fiber optic temperature sensor
PB231a	5	Ring 9	180	573	5450	Fiber optic total pressure sensor / radial
PB231b	5	Ring 9	180	608	5450	Fiber optic temperature sensor
UB201	2	Ring 3	270	420	1750	Pore Pressure
UB202	2	Ring 3	350	535	1750	Pore Pressure
UB203	2	Ring 3	90	635	1750	Pore Pressure
UB204	2	Ring 3	280	785	1750	Pore Pressure
UB205	5	Ring 9	270	420	5250	Pore Pressure in the sand
UB206	5	Ring 9	315	635	5250	Pore Pressure
UB207	5	Ring 9	90	710	5250	Pore Pressure
UB208	5	Ring 9	225	785	5250	Pore Pressure
UB209a	2	Ring 3	190	495	1750	Fiber optic pore pressure sensor
UB209b	2	Ring 3	190	555	1750	Fiber optic temperature sensor
UB210	5	Ring 9	160	420	5190	Fiber optic pore pressure and temperature sensor
TB 215	3	Ring 4	97.5	320	2450	Pentronic thermocouple thermometer
TB 216	3	Ring 4	82.5	360	2450	Pentronic thermocouple thermometer
TB 217	3	Ring 4	97.5	390	2450	Pentronic thermocouple thermometer
TB 218	3	Ring 4	92.5	420	2450	Pentronic thermocouple thermometer
TB 222	3	Ring 4	92.5	480	2450	Pentronic thermocouple thermometer
TB 226	3	Ring 4	92.5	540	2450	Pentronic thermocouple thermometer
TB 229	3	Ring 4	97.5	585	2450	Pentronic thermocouple thermometer

TB 235	3	Ring 4	87.5	690	2450	Pentronic thermocouple thermometer
TB 238	3	Ring 4	92.5	780	2450	Pentronic thermocouple thermometer
TB 239	3	Ring 4	87.5	810	2450	Pentronic thermocouple thermometer
TB 254	6	Ring 10	90	343	6056	Pentronic thermocouple thermometer
TB 255	6	Ring 10	90	420	5950	Pentronic thermocouple thermometer
TB 256	6	Ring 10	90	480	5950	Pentronic thermocouple thermometer
TB 257	6	Ring 10	97.5	540	5950	Pentronic thermocouple thermometer
TB 260	6	Ring 10	82.5	585	5950	Pentronic thermocouple thermometer
TB 267	6	Ring 10	87.5	690	5950	Pentronic thermocouple thermometer
TB 273	6	Ring 10	97.5	780	5950	Pentronic thermocouple thermometer
TB 275	6	Ring 10	87.5	810	5950	Pentronic thermocouple thermometer

2.2 Results of in-situ measurements

Results of measurements used for model comparison are shown in Appendices 3 to 8 and Appendices 16 and 18 and explained in the following chapters.

2.2.1 Temperature

2.2.1.1 Temperature in the buffer

For measuring the temperature evolution in the buffer, temperature sensors from Pentronic have been installed. The sensors are used in 3 cylinders (C1,C2,C3) and 2 rings (R4 and R10) with a total of 92 measurement points in the test hole. It should be noted that, 9 of 92 transducers are out of order (ÅKESSON et al. 2007b).

The highest temperature at the canister surface is 140°C, and 138°C in the bentonite measured by sensor TB215 located in the mid-plane of canister-1 at the distance of 15 mm from the canister surface. These two values are showing a very small temperature drop (2 K) in between the canister and the bentonite ring. Temperature is also measured in the sand buffer around canister-2, and it is found that the temperature drop is quite large (approximately 2.5 K/cm). The highest temperature (130-140°C) in bentonite was observed in ring R4 (Figure 2-3) while the lowest (87°C) can be found in cylinder C3. The injection of water into the sand buffer led to the temperature decrease around the upper heater.

In the beginning of June 2006 (day~1171) the increase in temperature is due to a power raise of about 100 W (Figure 2-2). In addition the raise in ventilation temperature (in summer) yields an increase in temperature of about 1 K which was observed in the upper part of the buffer in the beginning of June (day~435) (ÅKESSON et al. 2007b).

After about 200 days, the temperature results generally show consistent trends up to the maximum values. However for inner parts of cylinder C2 and inner sand buffer at ring R10, the maximum values were reached after only about 40 and 60 days respectively (see Figure 2-3).

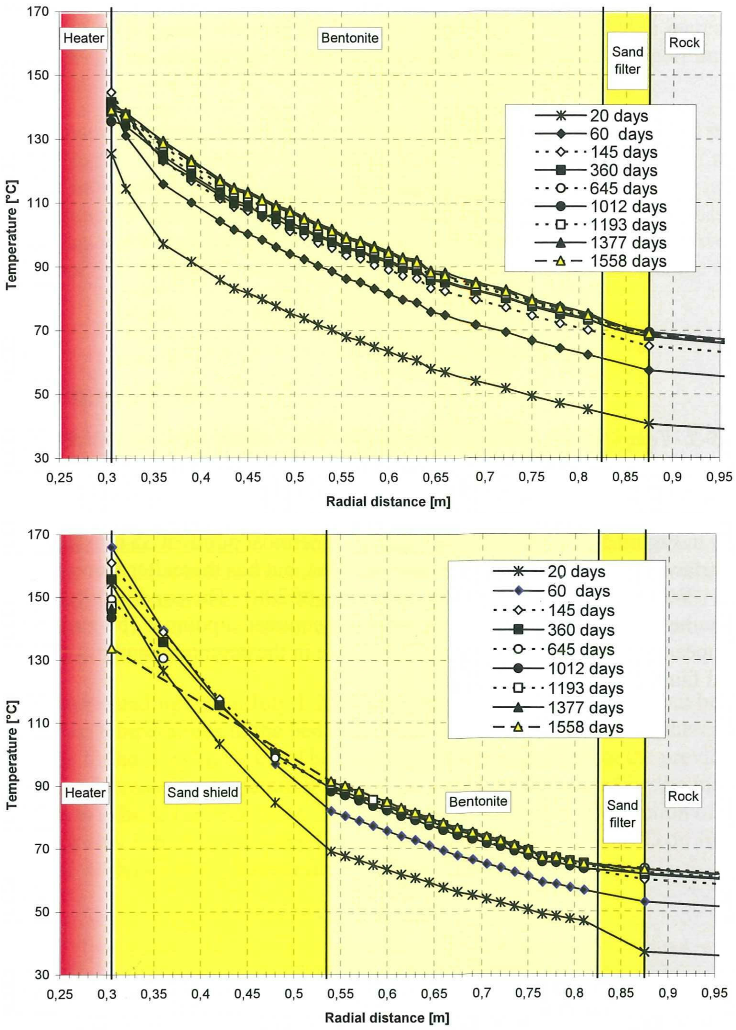

Figure 2-3 **Measured temperatures at mid-height of heater-1 (ring R4, z=2 m) and heater-2 (ring R10, z=5.5 m), day(0)=26.03.2003 (ÅKESSON et al. 2007b)**

2.2.1.2 Temperature in the rock

Thermocouples are used to measure temperature in the rock and on the rock surface of the hole, measurements were done at 40 points. The maximum measured temperature in the rock is 71°C, it is measured in the central section at the surface of the deposition hole.

Another experiment, the Canister Retrieval Test (CRT) is located 6 m from the TBT experiment and it was started approximately 880 days before the TBT and hence, it has a definite heat flux influence on TBT. This influence causes the deviation from axial symmetry of the temperature recorded in the rock in TBT. In order to compensate the heat loss caused by the CRT experiment, the power output of TBT heaters was raised from 1500 to 1600 W on June 2006 (see Figure 2-2). Finally, the CRT was terminated on October 2005.

2.2.2 Total pressure

The total pressure is measured with pressure cells by means of vibrating wire transducers and twenty nine cells of this type (ÅKESSON et al. 2007b). The measured pressure varies from 6.0 to 9.0 MPa due to the injection of water. It should be considered that except one transducer in the rock, all of them in ring R9 around the heater-2 show decreasing total pressure in a period roughly between day 230 and day 370 even though heating is still continuing.

In the lower and mid-section, stress distributions are quite isostatic. In the sections around the heaters, stress distributions indicate deviatoric stresses with relatively low radial stresses. This leads to the occurrence of largest displacements in radial direction around the heaters. Except the conditions in cylinder C3 in which one sensor still presents an increasing trend, all recorded total pressures are quite stable. This increasing trend in cylinder C3 is also confirmed by the increasing cable forces.

The injection of water into the sand buffer yields the pressure drop in ring R9. Between January 1st and July 1st, the most considerable drop was recorded by the innermost axial sensor, which decreased from 8.7 to 7.9 MPa.

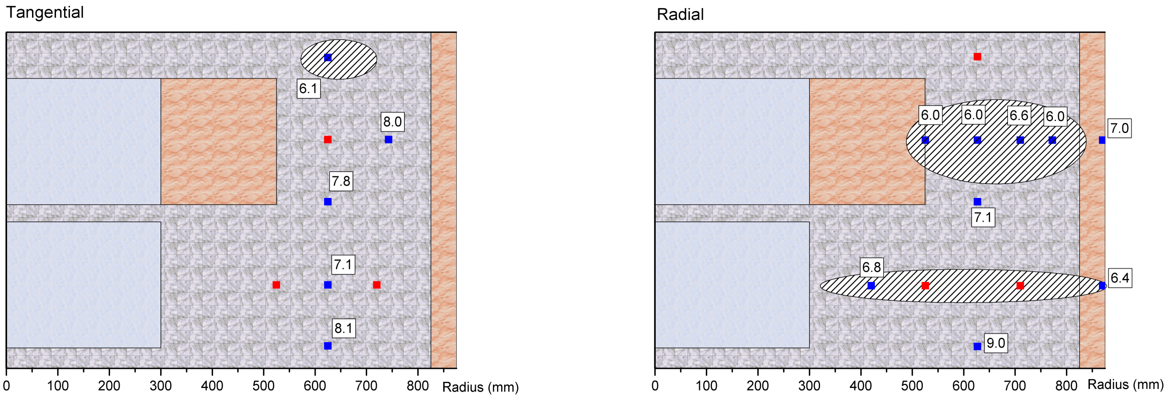

Figure 2-4: **Overview of total pressure in MPa (data on 01.07.2007). Pressure levels below 7 MPa marked with shaded pattern, blue boxes are sensor positions and red boxes indicate sensors out of order. The axial pressure results can not be shown due to the sensor failure as a result of the filter mat activation (ÅKESSON et al. 2007b)**

Some kind of grouping can be found, which implies that the vertical forces are mainly transmitted in a section corresponding to the buffer rings around the upper heater. Throughout the test period, the stress level around the heaters and in the lower cylinders is significantly higher than in the upper part of the experiment. However, this difference has decreased during the test period. According to ÅKESSON et al. (2006c), this has been evaluated as a balance between the vertical forces acting on ring R10 and the lid.

2.2.3 Pore water pressure

Pore water pressure is measured with pore pressure cells by vibrating wire transducer and eight cells of this type (ÅKESSON et al. 2007b). At the end of this measuring period, transducers UB206, UB207 and UB208 located in ring R9 show pore water pressure of about 0.3 – 0.5 MPa and transducer UB204 located in ring R3 presents pore pressure of about 0.1 MPa. As an example, a plot of the UB204 measurements is given in Appendix-16.

In principle, when pores are fully-saturated with water, the pore water pressure sensors should give a remarkable pulse which is above zero pressure (see Appendix-16). At present time, all sensors in ring R9 and four outermost sensors which are located in ring R3 clearly show positive values, which means that these parts are fully saturated. One problem with the pore pressure sensors which might put their accuracy into question, is that their absolute pressure value is though higher than the sand filter pressure.

2.2.4 Suction

Suction (negative water pressure) is measured with psychrometers operating at suction values below the limit of 7 MPa which corresponds to relative humidity higher than 95%. Six out of twelve transducers which have delivered interpretable values, are used to observe the ongoing suction process. Locations of these transducers are listed in Appendix-1 and their results are shown in Appendices 3 to 8.

It should be highlighted that during a period of about 80 days, two transducers around heater-2 are delivering increasing suction which actually indicates drying. This is consistent with the measured decrease in total pressure mentioned above. Furthermore, during the last 2 months the suction values of those transducers show a decrease, which is also consistent with the total pressure measurements (ÅKESSON et al. 2007b).

During the experiment, decreasing suction values between 6 and 1 MPa have been measured. Unfortunately, due to a general decrease in stresses in parts of ring R9, a suction increase is recorded in ring R10 at radius 785 and 735 mm after day 225 (Appendices 6&7). This unexpected increase in ring R10 can be explained by a localized extreme drying cycle, which is probably caused by a shortage in water supply in ring R9. Another incident which may support the water supply interpretation is the reversing of this trend when water injection through the upper tubes (injection level-2) was introduced.

2.2.5 Fiber optic sensing systems

Since a sand buffer plays a significant role for disposal of heat generating waste in clay host rock, numerical analyses have been carried on the temperature development to identify the impact of the sand buffer in comparison with direct canister emplacement in bentonite. Since under these conditions fiber optic sensors have never been implemented before, a few optical pressure and temperature sensors (8 sensors/4 sensor couples) have been installed for evaluation purposes. According to the latest in-situ data updates (ÅKESSON et al. 2007b), 3 of 4 fiber optic sensors are out of order, however in this report all of the sensor data have been presented. Appendix-18 shows the latest updated (26.03.2003 - 01.06.2008) results for temperature and total pressure evolution of the last sensor PB231 which still delivers data.

Two total pressure and two pore water pressure sensors have been installed each including a low resolution temperature grating for compensation purposes. Figures 2-5 and 2-6 show the location of each sensor together with all the other sensors.

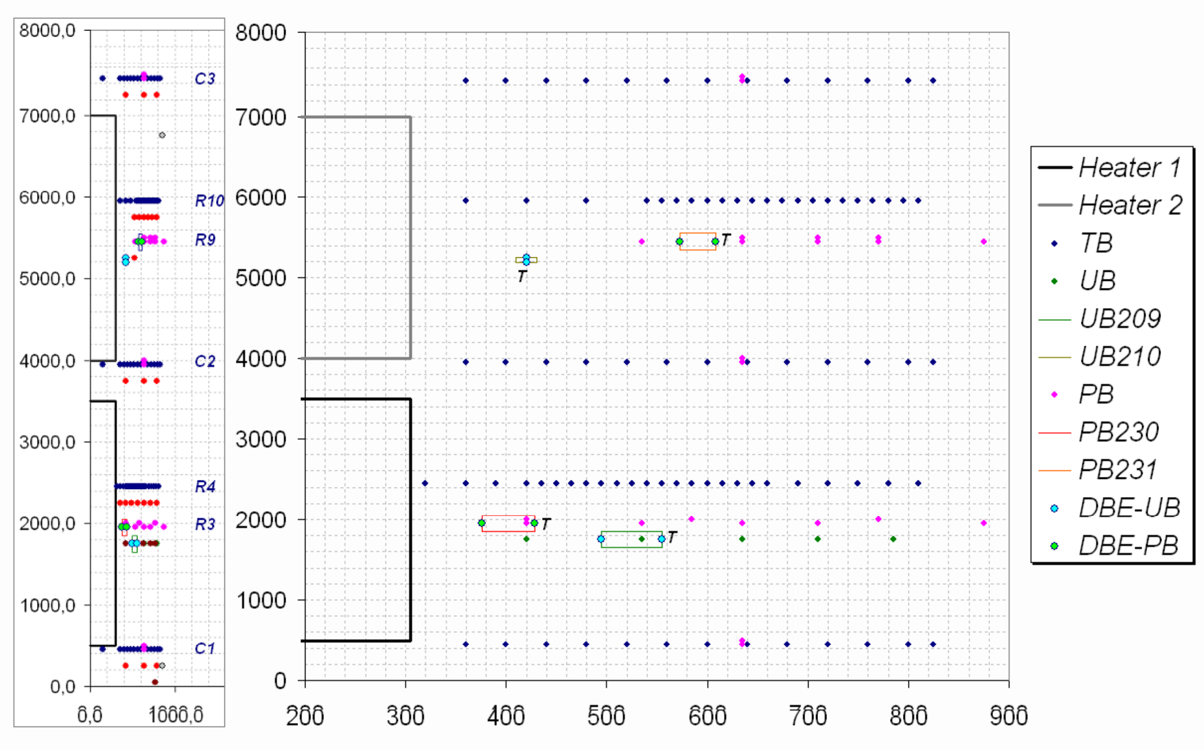

Figure 2-5: **Vertical locations and radial distances of each sensor in mm**

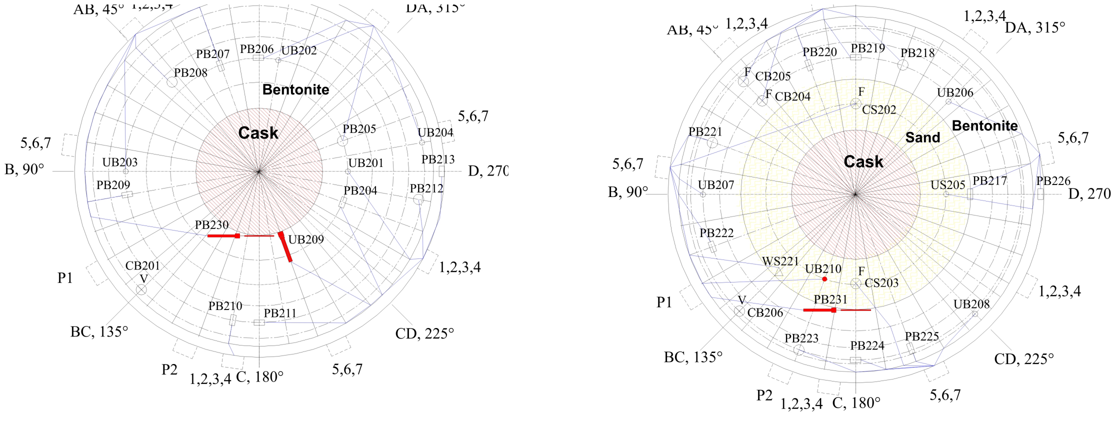

tion 2

ection 5

Figure 2-6: Radial location of sensors in horizontal cross-sections for ring R3 (left) and ring R9 (right)

Looking at Figure 2-7, it can be seen that the temperature of UB209 is higher than the other sensors, especially as time increases. The sensor is embedded in radial direction with the temperature grating at the outer end of the sensor housing, as shown in Figure 2-5. Thus, the reason for the higher temperature seems to be the high thermal conductivity of the metal housing. That means the temperature at the T-grating increases much faster due to the thermal conduction through the housing than it would do in case of temperature conduction through pure bentonite only.

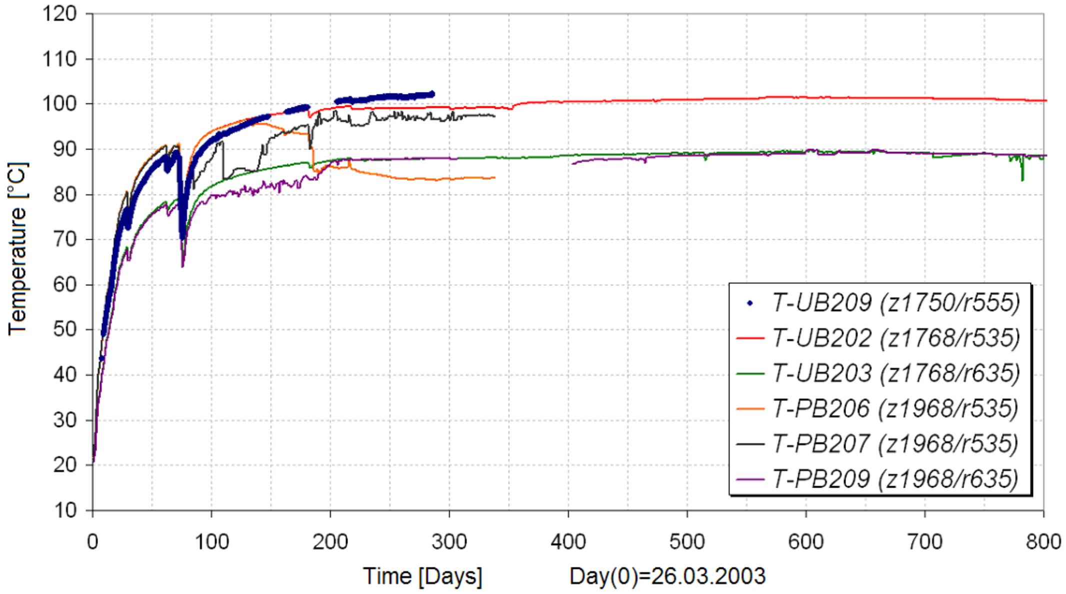

Figure 2-7: **Results of the temperature grating of sensor UB209 (ring R3)**

The same effect can be observed if we look at the results of PB230 and PB231. In Figure 2-8 and 2-9 results of the temperature gratings of PB230 are given. In addition, the measurements of other sensors in a comparable radial distance and vertical location are plotted. In case of PB230, the temperature difference is higher which can be explained by the nearer distance of this sensor to the heater that causes a higher temperature gradient. Normally the high thermal conductivity of the housing is good to achieve temperature equilibrium for compensation purposes but if we look at the pressure results later on, in this case it is even not good enough due to the high temperature gradient.

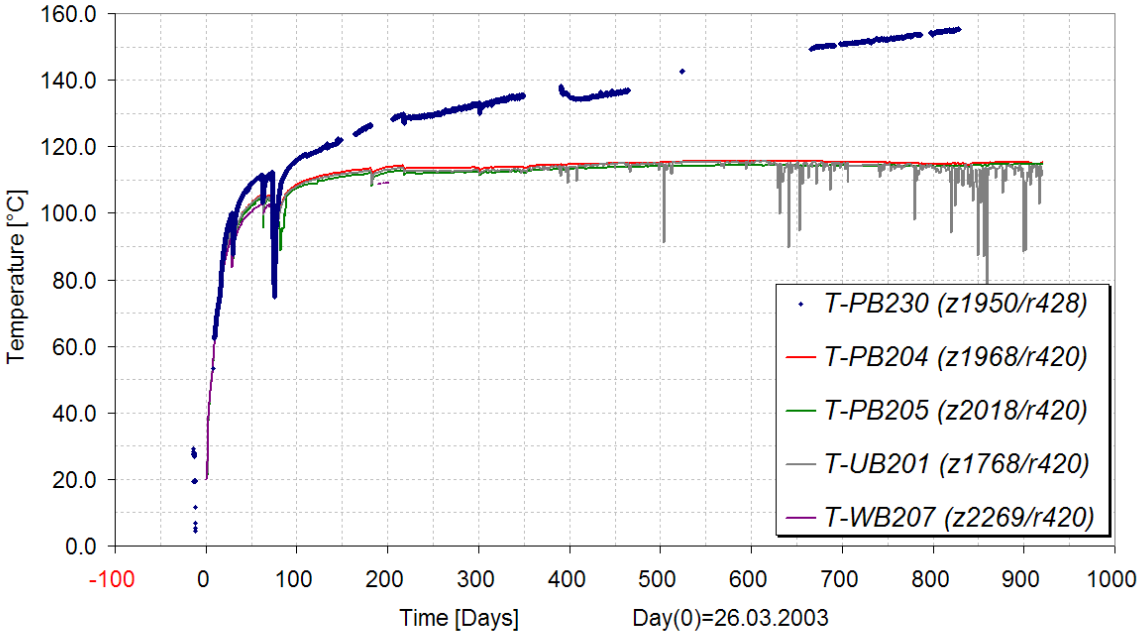

Figure 2-8: **Results of the temperature grating of sensor PB230 (ring R3)**

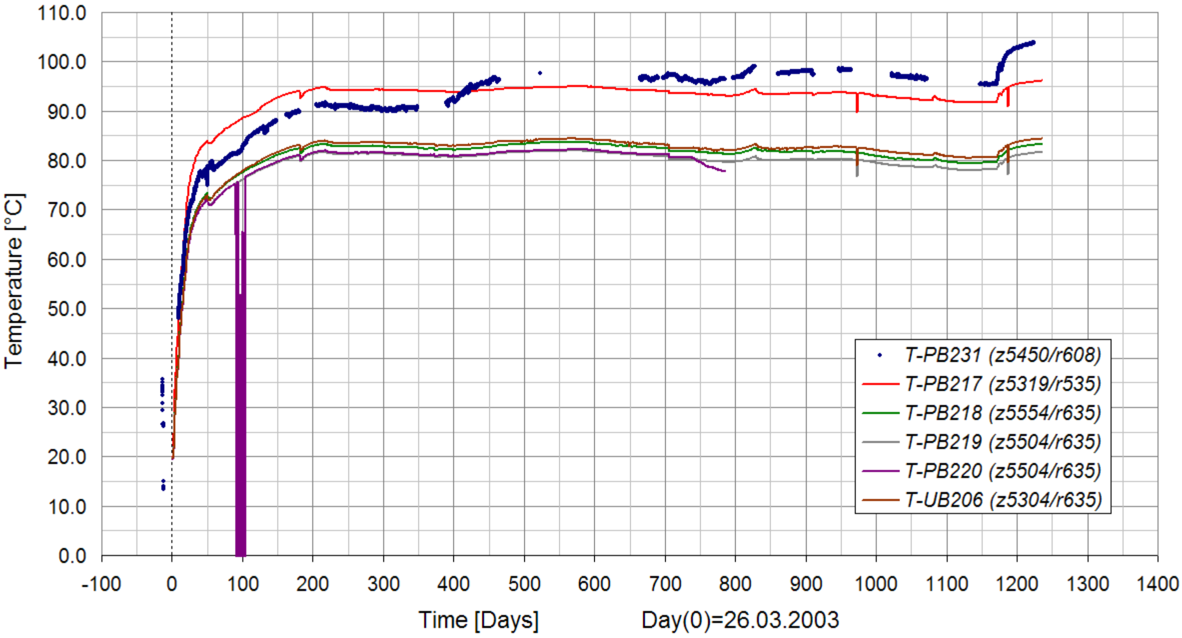

Figure 2-9: **Results of the temperature grating of sensor PB231 (ring R9)**

That means the temperature grating is located in about the same radial distance. In Figure 2-10 the results are plotted together with other sensor results for comparison. The problem of comparison is due to the different locations of the sensors. Mean values of different sensors have been calculated in order to improve the possibility of comparison. The temperature seems to be plausible at least for later times. Line 4 (violet) is the mean value of lines 1,2 and 3, and line 5 (orange) is the mean value of the two marked sensors more far away. In the beginning, there seems to be some inertia in the signal reaction that might be due to a less good contact of the T-grating.

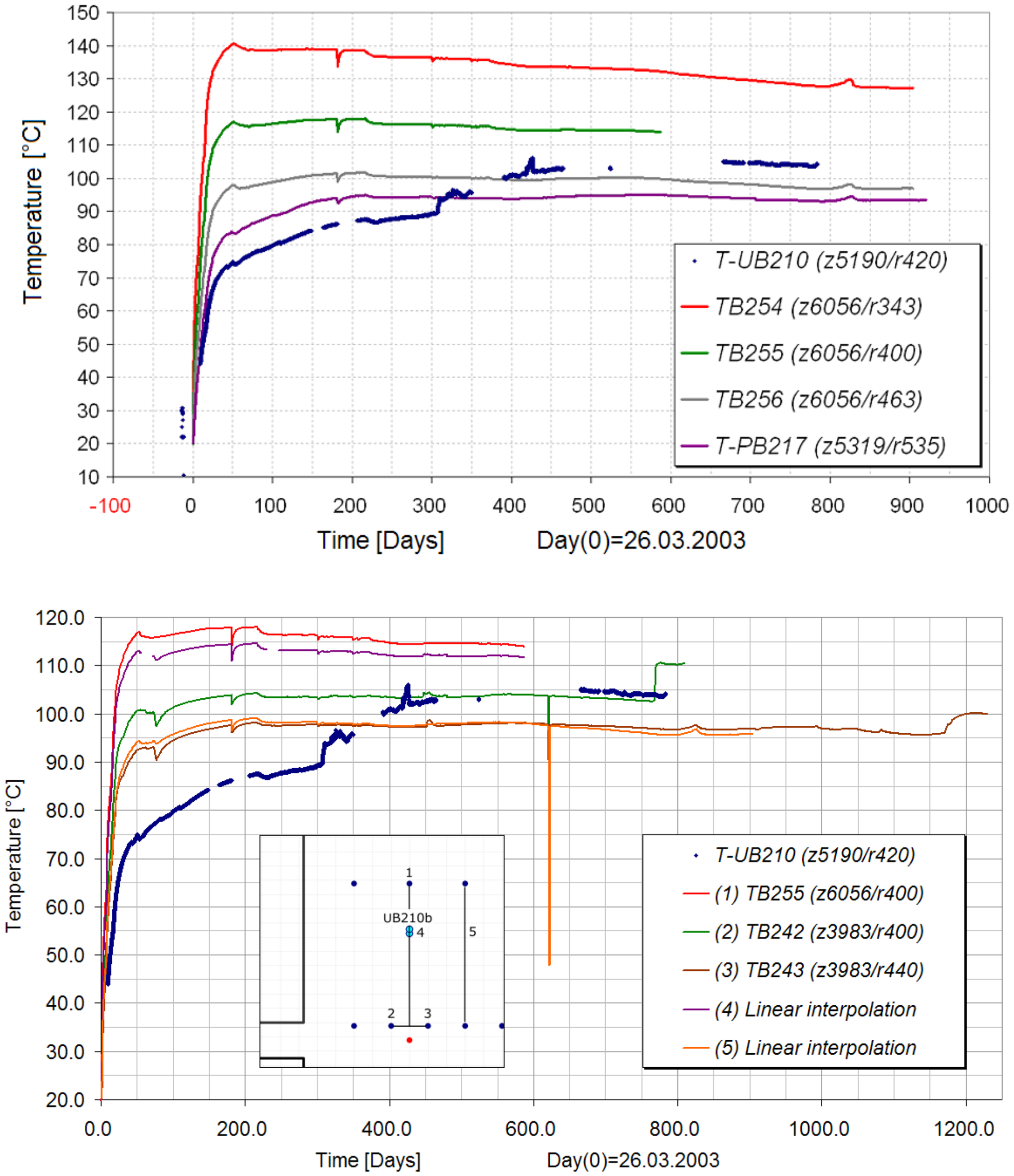

Figure 2-10: **Results of the temperature grating of sensor UB210 (ring R9) compared to results of other adjacent sensors and mean values of corresponding sensors**

In case of sensor UB210, the situation is different since this sensor is embedded more or less parallel to the heaters surface.

Figure 2-11 shows the results of pressure sensor PB230 that measures the pressure horizontally in radial direction. The sensor is located very close to the lower heater. The pressure reached a maximum value of about 8.8 MPa and goes down to about 4.6 MPa at the time being.

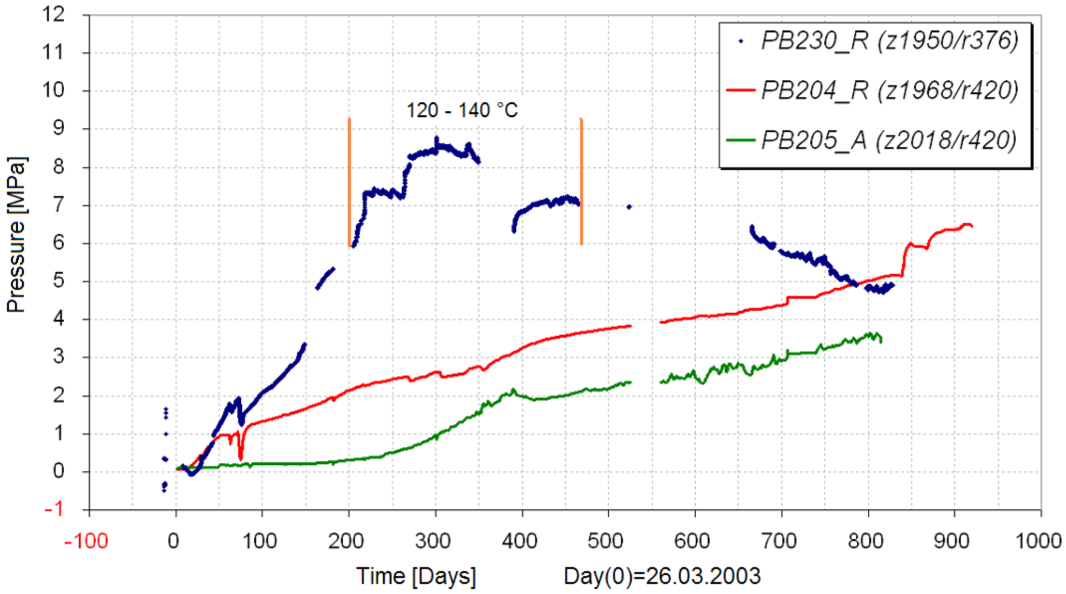

Figure 2-11: **Results of pressure sensor PB230 (ring R3)**

In Figure 2-11 the maximum pressure has been measured after the temperature exceeded 120°C. The reason for this pressure peek is due to the fact that sensor PB230 is located more or less directly at the canister surface while the other sensors are more far away as to be seen on Figure 2-5. In this case the canister acts as an abutment and the sensor takes the entire load and this can cause thermal induced water loss or evaporation occurred in direct vicinity of canister then the pressure started to decrease down to a value that is measured by the other sensors more far away. In laboratory investigations regarding thermal expansion, a strong dependency of the shrinking as a function of water content has been observed. The results of thermal expansion measurements are shown in *Section 3.1.4, Figure 3-6*. In that figure the lower graph clearly indicates the temperature range where water release takes place.

Results of pressure sensor PB231 are plotted in Figure 2-12. In the beginning some negative pressure values have been observed. These negative values occurred due to the strong temperature gradient within the housing which could not be compensated for. It has been tried to use some other sensors for compensation, but due to the fact that the vertical position has also an influence on the real temperatures, the exact temperature evolution at the pressure grating has still some uncertainties. The sensor is located at the boundary between the sand and the bentonite of the upper heater, thus not as close as PB230 at the lower heater. The effect is less for sensor PB230 due to the fact that the real pressure increase is much higher that close to the heater surface making the temperature effect less significant. The pressure of PB231 reaches a maximum value of about 9.0 MPa at the time being. This is about the same maximum value as measured by PB230 but at a later time.

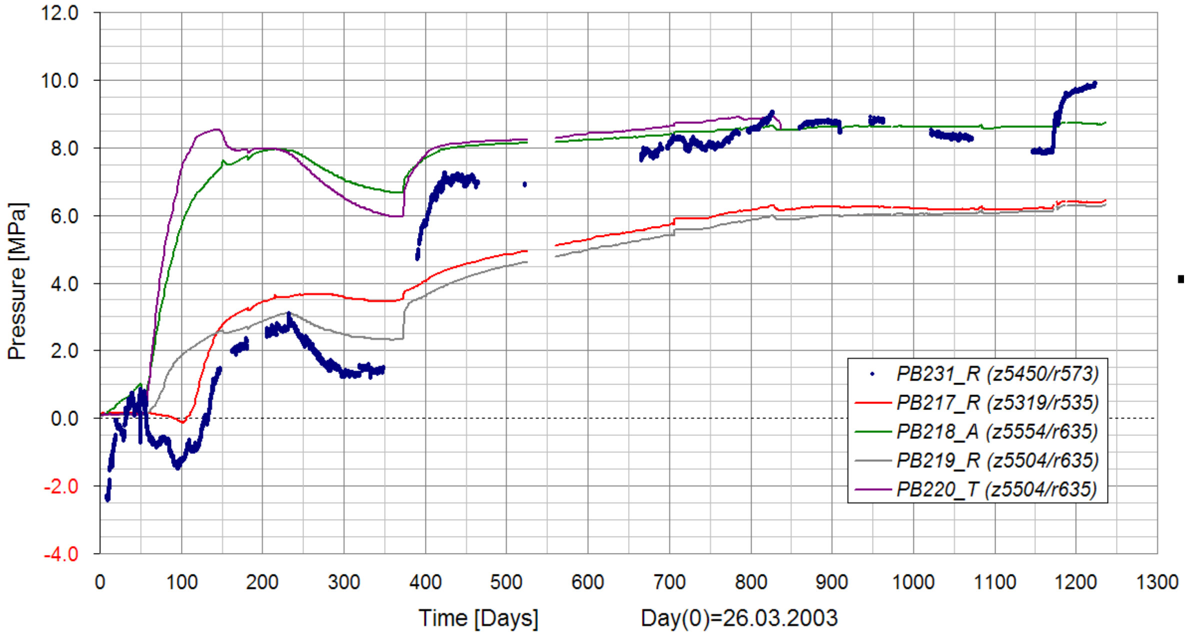

Figure 2-12: Results of pressure on sensor PB231 (ring R9), R=Radial, A=Axial, T=Tangential

3 LABORATORY AND LITERATURE INVESTIGATIONS

3.1 Laboratory investigations

Laboratory investigations were performed on MX-80 bentonite samples taken from Äspö Hard Rock Laboratory (BUNTEBARTH 2004). The following thermo-physical properties were determined:

- Thermal conductivity
- Thermal diffusivity
- Specific heat capacity
- Thermal expansion

3.1.1 Thermal conductivity

The thermal conductivity was measured at uni-axial pressure of 2 MPa and at temperatures up to 200°C. For the determination of the thermal conductivity, the heat flow meter apparatus was used. One-dimensional (1D) steady state heat flow is established through a test specimen between two parallel plates at constant but different temperatures. The thermal conductivity is determined by measuring thickness, temperature gradient and heat flow through the sample.

The thermal conductivity was measured at temperatures between 35°C and 200°C. Three different water contents were considered: one sample with a water content of 10%, another sample with a water content of 17% and the last sample which was dried for several hours in the apparatus at a pressure of 1 MPa and at a temperature of 98°C. The measuring results are shown in Figure 3-1.

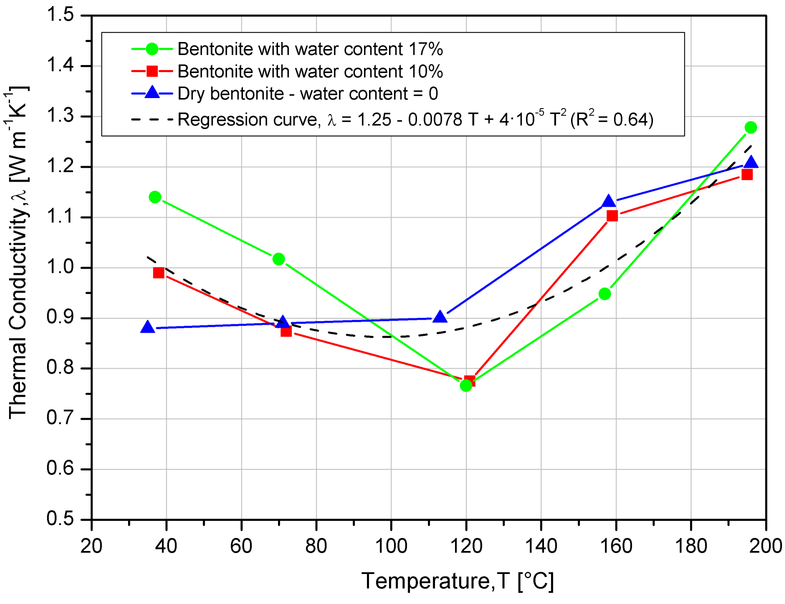

Figure 3-1: **Evolution of thermal conductivity curves with temperature for different water contents (Na-bentonite samples)**

Equation 3.1 is proposed to describe the thermal conductivity as a function of the temperature (see also Figure 3-1). In this consideration all samples are taken into account.

$$\lambda = 1.25 - 0.0078 \cdot T + 4 \cdot 10^{-5} T^2 \tag{3-1}$$

with: λ Thermal conductivity [W m^{-1} K^{-1}]
T Temperature [°C]

3.1.2 Thermal diffusivity

The thermal diffusivity was determined at uni-axial pressure of 2 MPa and at temperatures up to 200°C. For the determination of the thermal diffusivity, the heat flow meter apparatus was used as well. Following a temperature equilibrium, the temperature on one side of the sample was increased linearly.

When both thermal conductivity and thermal diffusivity values are determined at the same sample, then specific heat capacity can be calculated by means of known density.

The measurement results are shown in Figure 3-2. There is no clear relationship between thermal diffusivity and water content. In addition the water content has less influence on the thermal diffusivity than on the thermal conductivity. Although thermal conductivity and thermal diffusivity are being calculated only through a scalar value, they show a different behavior. Thermal conductivity decreases up to a temperature of 100°C however thermal diffusivity increases up to 130°C. Above a temperature of 130°C, the thermal diffusivity decreases slightly, but above 100°C thermal conductivity increases clearly. Finally, thermal diffusivity can be assumed as a constant within the uncertainty of measurement.

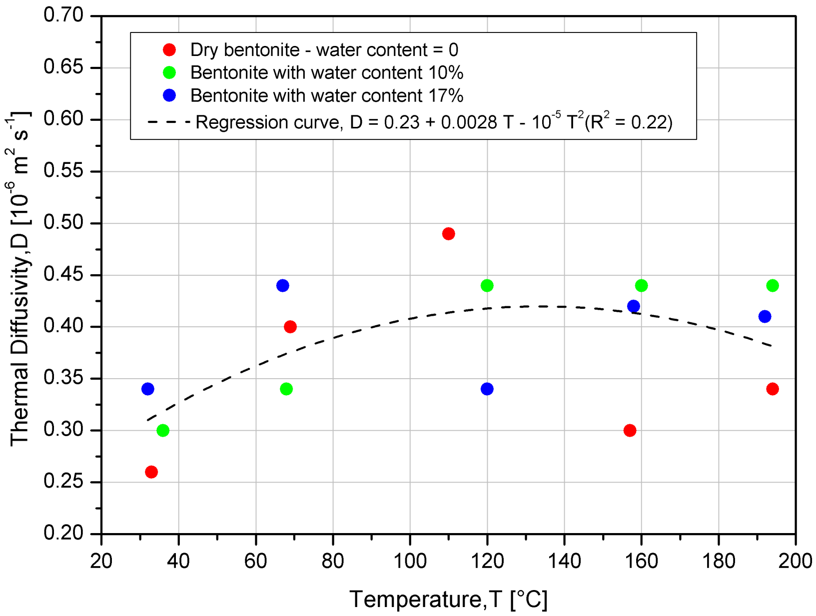

Figure 3-2: **Thermal diffusivity as a function of temperature**

Equation 3-2 is proposed to describe the thermal diffusivity as a function of the temperature (see also Figure 3-2). In this consideration all samples are taken into account.

$$D = 0.23 + 0.0028 \cdot T - 10^{-5} T^2 \tag{3-2}$$

with: D Thermal diffusivity [10^{-6} m^2 s^{-1}]
T Temperature [°C]

3.1.3 Specific heat capacity

The specific heat capacity, *c* is the amount of heat per unit mass required to raise the temperature by one Kelvin. Because of the expansion during the temperature rise, specific heat capacity is distinguished between the specific heat capacity at constant volume c_v and at constant pressure c_p. In case of solids the difference is negligible and then it can be assumed as; c_v=c_p. The specific heat capacity is measured with a heat flow difference calorimeter which is developed for a temperature range from ambient temperature to a temperature of 250°C. Both a sample and a reference sample are heated at a constant rate, then the temperature difference between them is measured. The amplitude of the measurement signal depends on the heat capacity of the two samples.

Several water contents were considered: one sample with a water content of 9.5%, a second sample with a water content of 16.1% and a third sample was dried one day at a temperature of 98°C resulting in a water content of 1.2%. To achieve an even lower water content a second sample was dried a bit longer resulting in a water content of 0.2%.

The results of the measurement are given in Figure 3-3. The two samples with a water content of 16,1% and 9,5% show a large increase of the specific heat capacity up to temperatures of 110°C, that is obvious due to the necessary energy for water release. The dried samples show another maximum at temperatures between 70°C and 80°C, which does not correlate with residual water contents. This indicates endothermic reactions which depend on the embedded cations at the interstitial surfaces.

The specific heat capacity values at a temperature of 30°C show a linear dependency on water content w (see Figure 3-4 and Equation 3-3). The slope of the fitting line contains both the specific heat of the water (c_p=4.2 kJ kg^{-1} K^{-1})) and the adsorption energy, which makes a contribution to the specific heat capacity of c_p = 0.028 kJ kg^{-1} K^{-1} per 1% water content.

$$c = c_p = 0.07w + 0.95 \tag{3-3}$$

c Specific heat capacity [kJ kg^{-1} K^{-1}]
w Water content [%]

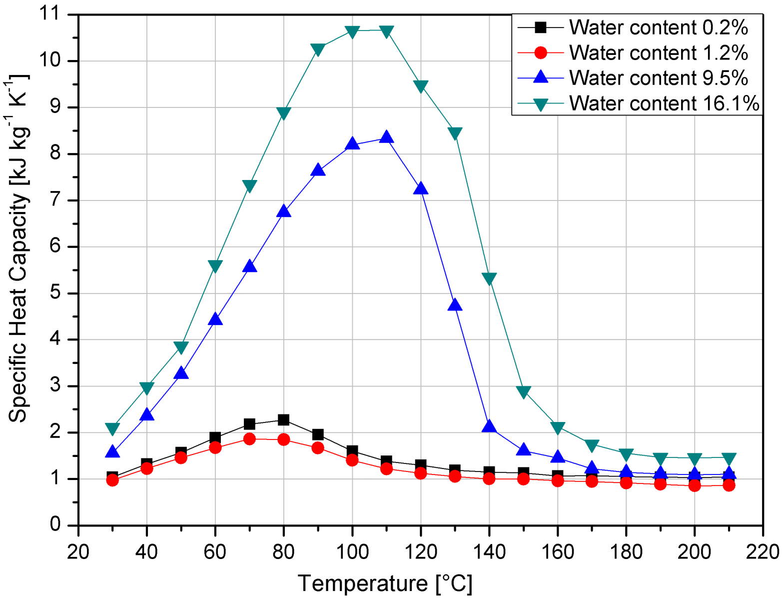

Figure 3-3: **Evolution of apparent specific heat capacity curves with temperature for different water contents**

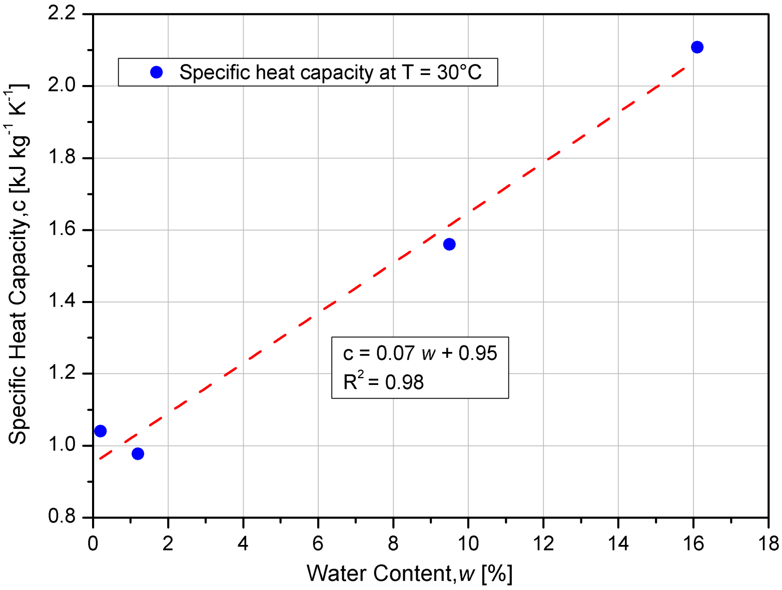

Figure 3-4: **Dependency between apparent specific heat capacity and water content at the prescribed temperature T=30°C**

3.1.4 Thermal expansion

The thermal expansion is measured with a Netzsch-Dilatometer (Type 402 E). The measurement of temperature is carried out directly on the sample with a thermocouple. The measurement readings of the heat expansion are recorded dynamically at a heating rate of 2 K min^{-1} from ambient temperature to a temperature of 210°C.

The samples consist of quite homogeneous material, which contains clay minerals of the montmorillonite group and show no obvious bedding. The samples maintain their structure even after the test, and a loss of 17.4% water. The water content of the samples is 17.4%, 10.8% and 3.3%. The sample with the water content of 3.3% was vacuum dried at a temperature of 97°C for one day but during the heating up to 210°C the sample lost 3.3% water. Therefore, the test was performed with this sample again. During this test, no loss of water was observed.

The samples expand up to a temperature of 65°C and then shrink with increasing temperatures (see Figures 3-5 and 3-6). In some temperature ranges the samples neither expand nor shrink. This effect depends on the water content of the sample and appears especially at high temperatures. Most of the water was released below 100°C during the heating.

Looking at the thermal expansion results, it seems that the samples differ in their mineralogical composition. Whereas the sample with a water content of 17.4% lost a significant amount of water at a temperature of about 140°C, this effect is negligible for the sample with a water content of 10.8%.

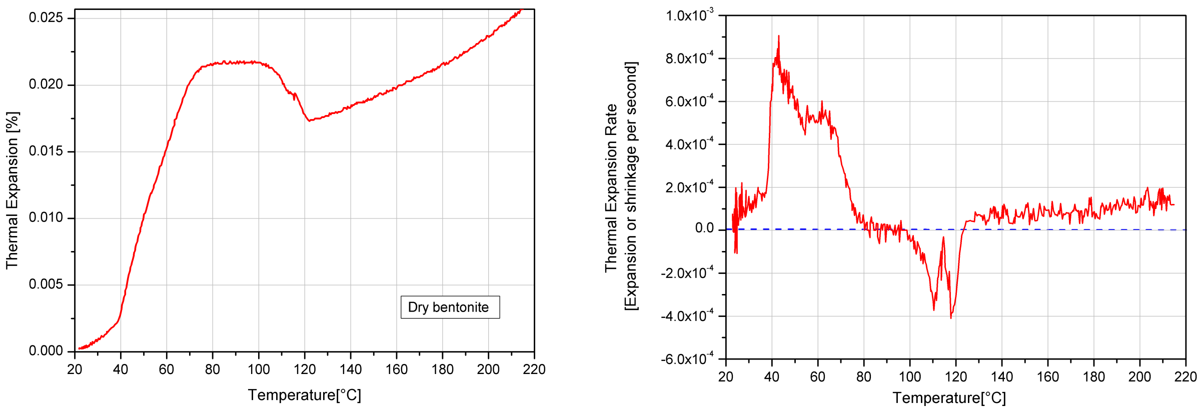

Figure 3-5: **Evolution of thermal expansion (shrinkage) of montmorillonite clay with temperature**

Figure 3-6 gives an overview of the measurement results showing the strong dependency of the shrinkage on water content. The lower graph, showing the first derivative of the expansion curve, clearly indicates the temperature range (approximately 70 – 120°C) where water release takes place.

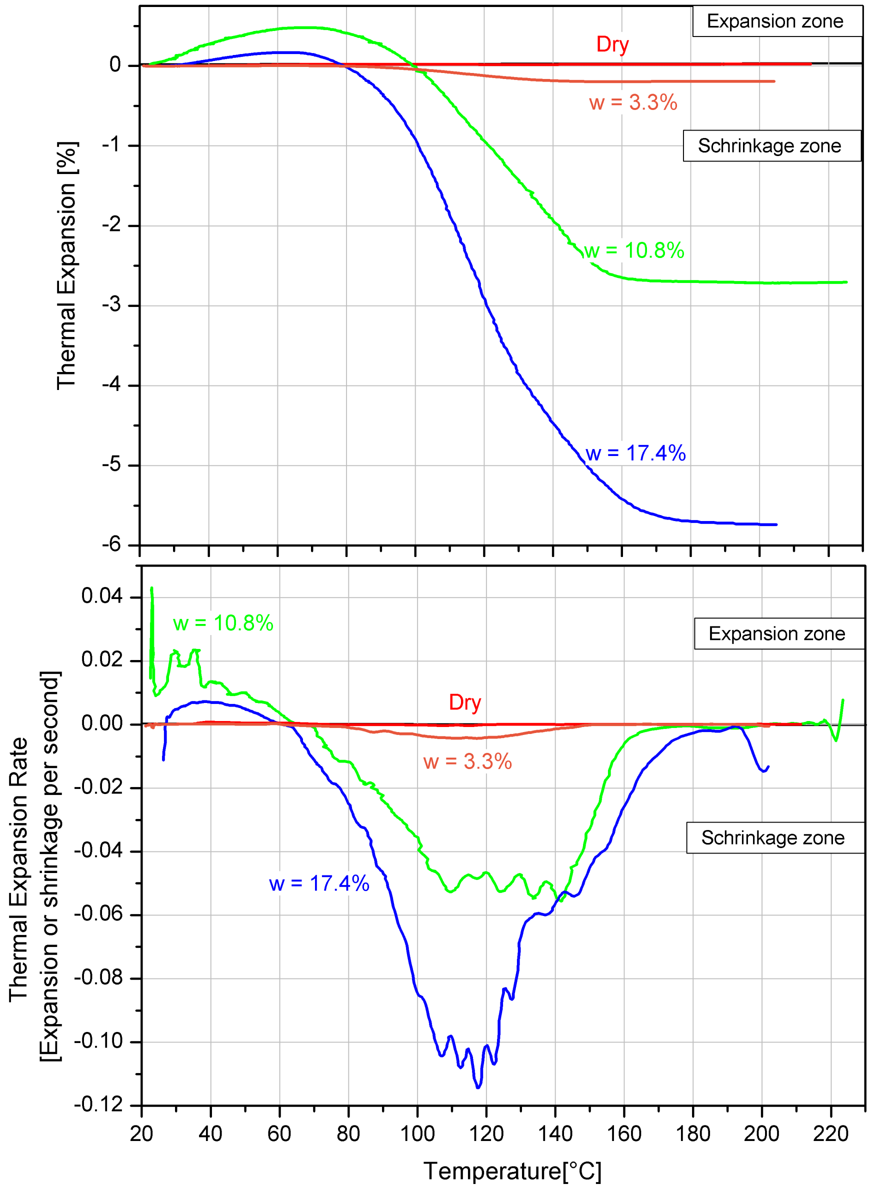

Figure 3-6: **Thermal expansion (shrinkage) rate at different water contents**

3.2 Literature investigations

Literature investigations were done in order to determine the thermo-hydraulic properties of the sand, Äspö diorite and bentonite from Äspö Hard Rock Laboratory for comparison with the laboratory investigations described above.

3.2.1 Sand

The thermal conductivity of sand depends on the liquid saturation. The following values are taken from BÖRGESSON (1982). At full liquid saturation the thermal conductivity of sand is 2.0 W m^{-1} K^{-1} and at the initial state of saturation (S_L=0.8) the thermal conductivity of sand is 0.3 W m^{-1} K^{-1}. Assuming a linear correlation between saturation and thermal conductivity of sand, the following formula was given as:

$$\lambda_{sand} = 8.5 S_L - 6.5 \tag{3-4}$$

λ_{Sand} Thermal conductivity of sand [W m^{-1} K^{-1}]
S_L Saturation of the liquid phase [-]

According to HÖKMARK et. al (2005) the density of sand is 1800 kg m^{-3} and the specific heat capacity is 800 J kg^{-1} K^{-1}.

3.2.2 Äspö diorite

According to SUNDBERG&GABRIELSSON (1999) and SUNDBERG (2002) the median density of the fresh Äspö diorite is 2753 kg m^{-3}. No significant dependency of thermal conductivity on liquid saturation has been detected because of the low porosity.

The thermal properties at Äspö HRL have been studied by SUNDBERG&GABRIELSSON (1999) and SUNDBERG (2002). The measurements of thermal conductivity gave a value of λ_{Host_rock}=2.57 W m^{-1} K^{-1} and the volumetric heat capacity was determined as c_V=2.16 MJ m^{-3} K^{-1}. The specific heat capacity was calculated as follows:

$$c_p = \frac{c_v}{\rho_{Host\_rock}} = 785 \text{ J kg}^{-1}\text{ K}^{-1} \tag{3-5}$$

c_p	Specific heat capacity [J kg^{-1} K^{-1}]
c_v	Volumetric heat capacity [10^6 J m^{-3} K^{-1}]
ρ_{Host_rock}	Density of the host rock [kg m^{-3}]

3.2.3 Bentonite

The properties of the MX-80 bentonite strongly depend on the temperature and the water content (see *Chapter 3.1*). At the initial state of the water content w=0.17, the density is 2000 kg m^{-3}. The specific heat capacity is assumed as c_p=1300 KJ kg^{-1} K^{-1}.

KAHR&MÜLLER-von MOOS (1982) investigated the thermal conductivity of MX-80 bentonite and developed the following equation:

$$\lambda = 0.004w\rho^3 + 0.6\rho + 0.01\sqrt{T} - 0.6 \tag{3-6}$$

λ Thermal conductivity [W m^{-1} K^{-1}]
ρ Density [10^6 g m^{-3}]
w Water content [%]
T Temperature [°C]

In scope of design calculations, HÖKMARK et. al (2005) assumed constant values for thermal conductivity λ=1.2 at the initial state of the liquid saturation S_L=0.8 and λ=1.3 at the full liquid saturation state S_L=1. So this assumption is summarized as follows:

If S_L=0.8 then λ=1.2 (3-7)
If S_L=1 then λ=1.3

Table 3-1: Summarized paramater values from laboratory and literature investigation results (BÖRGESSON 1982, BÖRGESSON 1992 and SCHNEIDER&BERTIG 1994)

Parameter	**Canister**	**Äspö diorite**	**Bentonite MX-80**	**Sand**
Density [kg m^{-3}]	7850	2750	2000	1800
Thermal conductivity [W m^{-1} K^{-1}]	50	2.57	Equations 3-1, 3-6 and 3-7	0.3 (S_L=0.8) 2.0 (S_L=1) (From Equation 3-4)
Specific heat capacity [J kg^{-1} K^{-1}]	460	785 (From Equation 3-5)	1300 and Equation 3-3	800
Thermal expansion coefficient [10^6 K^{-1}]	12	8.3	30	12
Thermal diffusivity [10^{-6} m^2 s^{-1}]	NA*	NA*	Equation 3-2	NA*

Note: *(Not Available) means that the related parameter was not investigated yet.

4 NUMERICAL CALCULATIONS

As the temperature is one of the main forces of hydro-mechanical changes within the bentonite/sand barrier, the simulation of the temperature development is of major importance. The thermal parameter approach presented in this report is the result of various parameter variation calculations and of the adaptation of calculation values to the values measured in-situ. Subsequent to the thermal-only parameter approach, the hydraulic calculations were performed by means of capillary pressure (suction) due to its vital role for the water inflow throughout the bentonite. Finally based on the simulations, the development of the computed capillary pressures and temperatures compared with the measured capillary pressures and temperatures are evaluated through thermo-hydraulically coupled calculations.

4.1 Code description

The calculations described were performed by using the computer code TOUGH2 (Transport of Unsaturated Groundwater and Heat). TOUGH2 has been developed at the Ernest Orlando Lawrence Berkeley National Laboratory (LBNL) since 1991. The program allows the generation of one-, two-, and three-dimensional models of non-isothermal groundwater flow and transport processes in loose and solid rock, i.e. flow in porous media and along fracture planes. TOUGH2 also comprises the so-called EOS (Equation of State) modules. Within these modules the number and types of substances (components and phases) are defined and the thermo-physical properties of the flowing media are initialized. There are different EOS modules which can be applied depending on the problem type to be examined. For a complete system, the main program has to be combined with one of the various EOS modules. For the present work with TOUGH2, the EOS3 module (water, air) was used for the simulation of the temperature-dependent saturation of the bentonite/sand barrier. Unfortunately in this module, outputs for the parameters “relative humidity”, “pore pressure” and “total pressure” are not yet supported (PRUESS et al. 1999).

TOUGH2 uses an extended equation based on Darcy's law for multiphase flow to simulate the flow (Equation 4-1) and the energy equation (Equation 4-3) including conduction, convection and radiation (optional) for thermal transport (PRUESS et al. 1990,1999). The calculation of relative permeabilities for different phases and capillary pressure formulation are adjusted in the Equation 4-1 (see also Equation 4-2). For calculations of the heat flux TOUGH2 uses the Equation 4-3, in this equation only conductive and convective components are included. It should be considered that in TOUGH2, thermal conductivity is assumed as isotropic (see Table 4-1). TOUGH2 uses the “Integral Finite Difference Method (IFDM)” for space discretization and uses “fully implicit differencing method” for time discretization.

$$F_\beta = \rho_\beta u_\beta = -k \frac{k_{r\beta}\rho_\beta}{\mu_\beta}\left(\nabla P_\beta - \rho_\beta g\right) \tag{4-1}$$

F_β	Mass flux in phase β [kg m^2 s^{-1}]
u_β	Darcy velocity in phase β [m s^{-1}]
k	Absolute permeability [m^2]

$k_{r\beta}$	Relative permeability of phase β [-]
ρ_β	Density of phase β [kg m^{-3}]
μ_β	Dynamic viscosity of phase β [Pa·s]
g	Vector of gravitational acceleration [m s^{-2}]
∇P_β	Fluid pressure gradient in phase β [Pa m^{-1}]

Index β = The phase (liquid or gas)

$$P_\beta = P + P_{cap,\beta} \tag{4-2}$$

P	Pressure of a reference phase (usually taken to be the gas phase) [Pa]
$P_{cap,\beta}$	Capillary pressure in phase β (≤ 0) [Pa]

$$F^{NK+1} = -\lambda \nabla T + \sum_\beta h_\beta F_\beta \tag{4-3}$$

F	Heat flux includes conductive and convective components [W m^{-2}]
F_β	Mass flux in phase β [kg m^{-2} s^{-1}]
λ	Thermal conductivity [W m^{-1} °C^{-1}]
h_β	Specific enthalpy in phase β [J kg^{-1}]
∇T	Temperature gradient [°C m^{-1}]

Index NK = Mass components (water, air, H_2, solutes…etc.) and "1" indicates the heat component

PetraSim was used as a pre- and post-processor of the calculations with TOUGH2. This program allows interactive model generation including grid generation as well as the visualization of 3D iso-surface, vector, and contour plots. In addition to this, it allows the analysis of time-dependent parameters at freely chosen recording points (THUNDERHEAD ENGINEERING 2007).

4.2 Model description

The thermo-hydraulic (TH) calculations were performed using a simplified 2D (quasi 3D) axis symmetric model geometry (Figure 4-1) which is similar to a UPC model (ÅKESSON 2006b). The cylindrical coordinate system is used to locate the sensors and materials in the model domain. The model consists of 11346 zones. Along the x-axis the model ranges from the symmetry axis (center of heater) until 58.0 m, along the z-axis from -53.5 m until 61.5 m and along the y-axis from the symmetry axis until 0.5 m. This covers the essential elements of the TBT-experiment. The z-coordinate is counted from the top of the cement plate and α-axis is neglected owing to the model limitations. For the sake of simplicity, the section above the test room was modeled with a height and width of 5 m each. Furthermore, the surrounding solid rock was first configured as hydraulically impermeable and later as low permeable (see Table 4-5).

The definition of the model parameters was based on the TBT modeling guidelines (HÖKMARK&FÄLT 2003; ÅKESSON et al. 2004 and ÅKESSON 2006a). The material characteristics of this first calculation approach were taken from published data (LEDESMA et al. 2005) and some were adapted for application in the relative permeability and capillary pressure laws implemented in TOUGH2 (e.g. VAN GENUCHTEN 1980). Based on in-situ measurement values, the sand filter surrounding the borehole was saturated depending on time. The heat power was simulated according to the experimental values including down times, see Table 4-7 and Appendix-2. Calculations using different parameter settings to improve the model-to-measurement fit were performed through two sections; “thermal” and “hydraulics”.

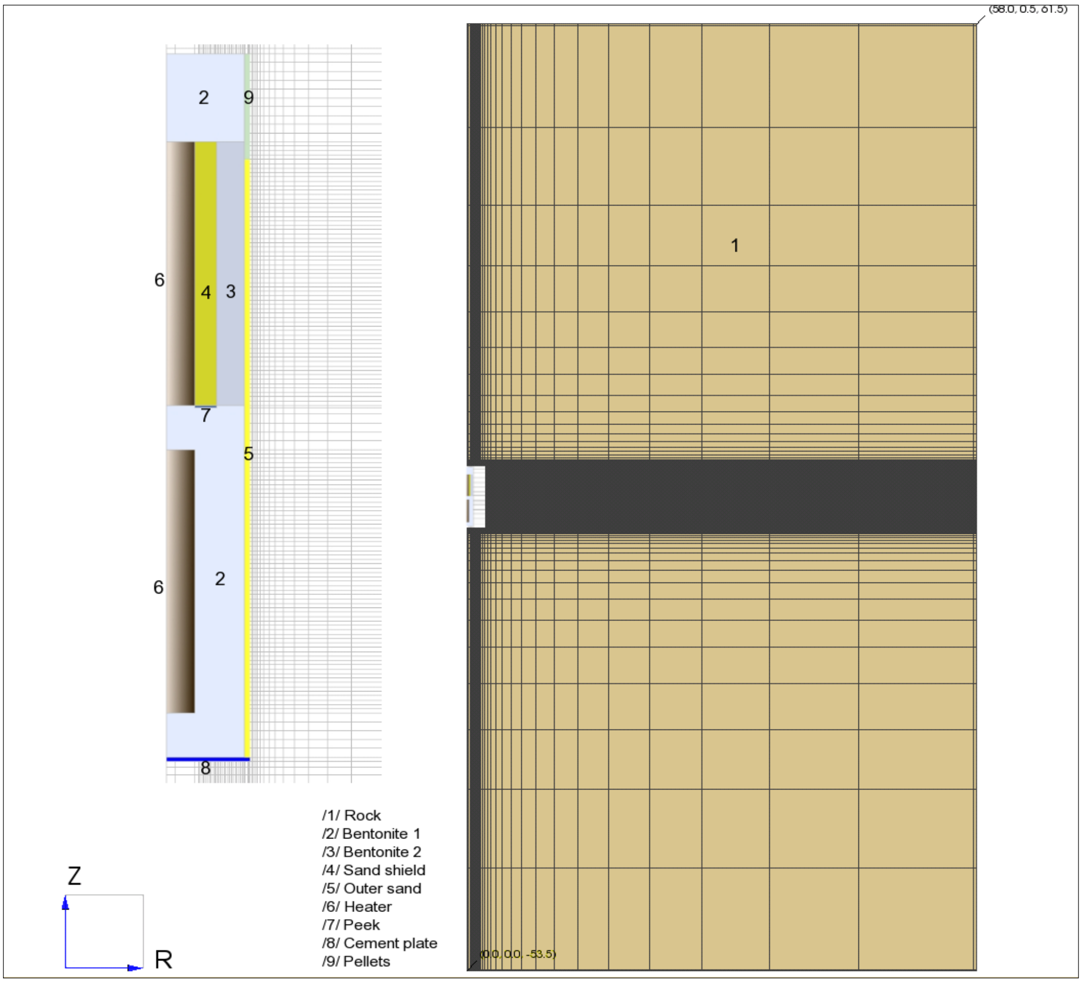

Figure 4-1: **Model geometry and materials considered (2D axisymmetric)**

4.3 Constitutive laws

The tables 4-1 to 4-3 list the parameters used as well as the starting variables and assumptions made for the calculations.

4.3.1 Thermal approach

Table 4-1: Thermal conductivity λ [W $m^{-1}K^{-1}$] and specific heat capacity c_p [J $kg^{-1}K^{-1}$] values used for the simulations (PRUESS et al. 1999)

	λ [W m^{-1} K^{-1}]			**c_p [J kg^{-1} K^{-1}]**
Material	**Law**	**λ_{dry}**	**λ_{sat}**	
Bentonite 1	$\lambda = \lambda_{dry} + \sqrt{S_L \cdot (\lambda_{sat} - \lambda_{dry})}$ (4-4) Note: In the code *thermal anisotropy factor* is not implemented.	0.57	1.36	1091
Bentonite 2		0.57	1.36	1091
Solid rock		1.73	3.0	800
Pellets		0.6	0.81	1091
Sand buffer		0.4	1.38	900
Sand filter		0.6	1.7	900
Concrete		1.7	1.7	900
Heater		50.16	50.16	480

4.3.2 Hydraulic approach

In the current simulation, the surrounding solid rock is modeled as a continuum with a low permeability and gas saturation, without capillary pressure properties and with heat conduction. This is to avoid liquid flow from sand filter into the rock.

Table 4-2: Capillary pressure function and parameters used for the simulations (VAN GENUCHTEN 1980; RODWELL et al. 1999; JOBMANN 2000; SCHAAP&VAN GENUCHTEN 2005 and ZHANG et al. 2007)

Material	**Law**	**m [-]**	**S_{lr} [-]**	**P_0^{-1} [Pa^{-1}]**	**P_{max} [Pa]**	**S_{ls} [-]**
Bentonite 1	$P_{cap} = -P_0\left(\left(S^*\right)^{-1/m} - 1\right)^{1-m}$ $S^* = \frac{(S_l - S_{lr})}{(S_{ls} - S_{lr})}$ $-P_{\max} \le P_{cap} \le 0$ $0 < m < 1$ $S_{lr} < S_l < S_{ls} < 1$ (4-5)	0.33	0.001	2.33•10^{-8}	9.0•10^{7}	1.0
Bentonite 2		0.33	0.001	2.33•10^{-8}	9.0•10^{7}	1.0
Solid rock		-	-	-	-	-
Pellets		0.4	0.001	5.00•10^{-5}	8.0•10^{7}	1.0
Sand buffer		0.3	0.001	1.00•10^{-5}	8.0•10^{7}	1.0
Sand filter		0.3	0.001	1.00•10^{-5}	8.0•10^{7}	1.0
Concrete		0.3	0.001	3.33•10^{-6}	9.0•10^{7}	1.0
Heater		-	-	-	-	-

Table 4-3: **Relative permeability equations used for the simulations (COREY 1954; FATT and KLIKOFF 1959; MUALEM 1976; GRANT 1977 and VAN GENUCHTEN 1980)**

Material	Law	m [-]	S_{lr} [-]	S_{ls} [-]	S_{gr} [-]
Bentonite 1	$k_{rl} = \begin{cases} \sqrt{S^*}\left\{1-\left(1-\left(S^*\right)^{1/m}\right)^m\right\}^2 & if\ S_l < S_{ls} \\ 1 & if\ S_l \geq S_{ls} \end{cases}$ $k_{rg} = \begin{cases} 1-k_{rl} & if\ S_{gr} = 0 \\ \left(1-\hat{S}\right)^2 \cdot \left(1-\hat{S}^2\right) & if\ S_{gr} \geq 0 \end{cases}$ (4-6)	0.8	0.05	1.0	0.1
Bentonite 2		0.8	0.05	1.0	0.1
Solid rock		0.3	0.1	1.0	0.1
Pellets		0.8	0.1	1.0	0.1
Sand buffer		0.8	0.05	1.0	0.1
Sand filter		0.8	0.05	1.0	0.1
Concrete		0.8	0.05	1.0	0.1
Heater	$k_{rl} = (S^*)^3$ $k_{rg} = (1-S^*)^3$ (4-7)	-	0.3	-	-
$0 \leq k_{rl}, k_{rg} \leq 1;\quad S^* = \left(S_l - S_{lr}\right)/\left(S_{ls} - S_{lr}\right),\quad \hat{S} = \left(S_l - S_{lr}\right)/\left(1 - S_{lr} - S_{gr}\right)$ (4-8)					

Figure 4-2 shows the adjustment of the capillary pressure curve to the data determined in experiments based on bentonite MX-80 (ÅKESSON 2006b). Clay Technology points out that recent experimental data indicate even higher values for the capillary suction pressure. In thermal only calculations the strict limitation of P_{max} to values below $1 \cdot 10^8$ Pa was introduced after repeated calculation aborts with higher P_{max} values. For the bentonite saturation range relevant to this case (> 0.7) this limitation has no effect.

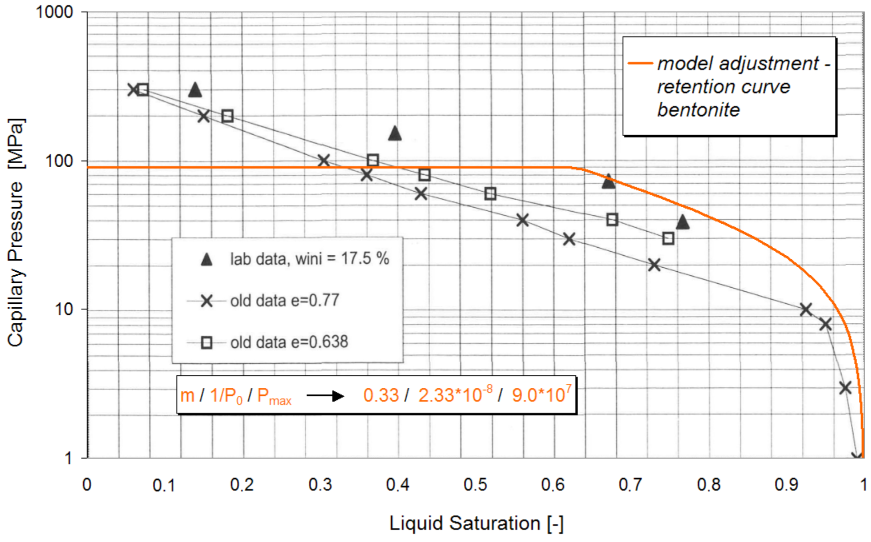

Figure 4-2: **Capillary pressure – liquid saturation relation used for model parameter adjustment of bentonite MX-80 (ÅKESSON 2006b)**

In addition to this, the implemented functions to determine the relative permeability are shown in Figure 4-3.

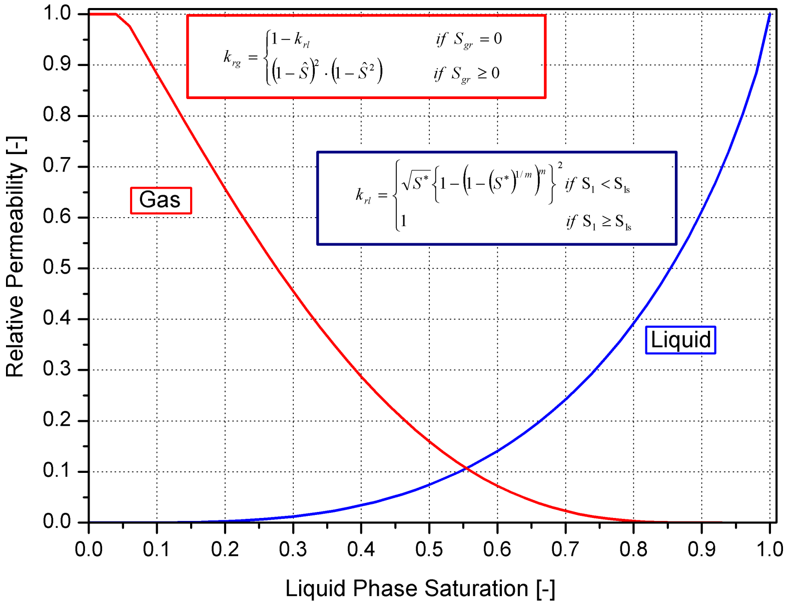

Figure 4-3: **Relative permeability – liquid saturation relation used for model parameter adjustment of bentonite MX-80 (MUALEM 1976, VAN GENUCHTEN 1980)**

Figure 4-4 shows the retention curves for the sand (filter and buffer), concrete, bentonite (1&2) and the bentonite pellets. These are, however, only first estimates, as reliable data to determine the water retention curves is not yet available.

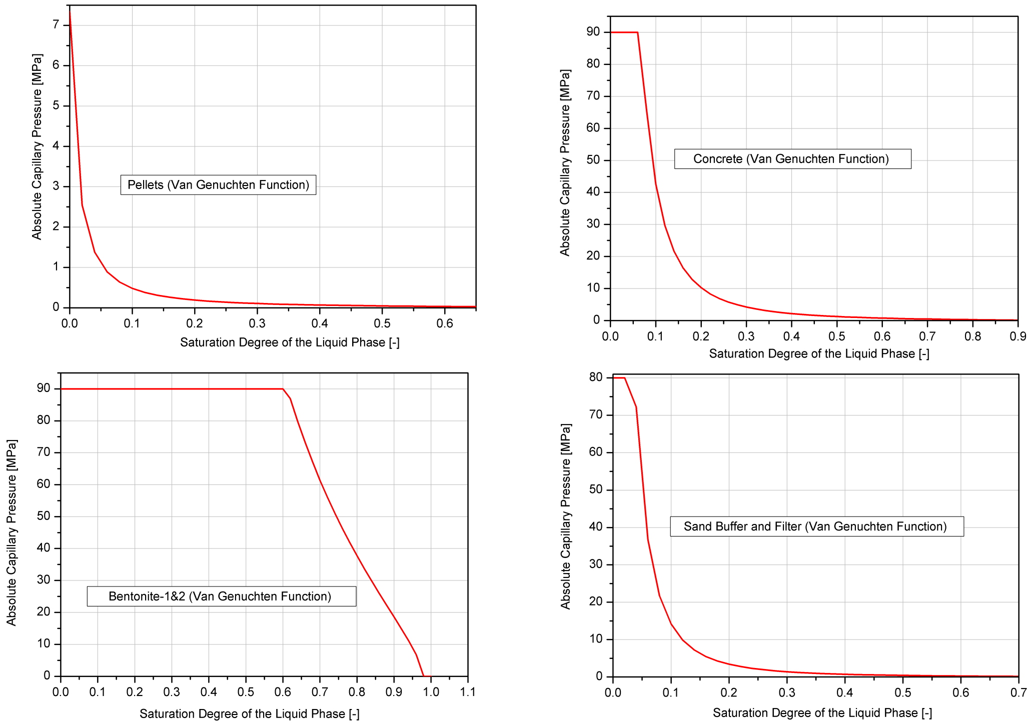

Figure 4-4: **Retention curves for bentonite, pellets, and sand**

4.3.3 Binary gas diffusion / molecular diffusion

For diffusion of vapor and air in the gas phase the code uses the binary gas diffusion as described below. According to KRÖHN (2004) and PRUESS et al. (1999), for practical purposes the coefficient of binary gas diffusion d_β^κ can be calculated with the semi-empirical approach;

$$d_\beta{}^\kappa(P,T) = d_\beta{}^\kappa(P_0,T_0)\frac{P_0}{P}\left[\frac{T+273.15}{273.15}\right]^\theta \tag{4-9}$$

$d_\beta{}^\kappa$	Coefficient of binary gas diffusion for the component κ (water or air) in phase β (gas) [$2.13 \bullet 10^{-5}$ m^2/s]
P	Pressure of the gas phase [Pa]
P_0	Gas phase pressure under reference conditions [101300 Pa]
T	Temperature [K]
T_0	Temperature under reference conditions [273.15 K]
θ	Constant fit parameter [1.8]

4.3.4 Pore compressibility

For the definition of pore compressibility the code employs the formula given below. According to PRUESS et al. (1999) pore compressibility depends on porosity, pressure and temperature changes through an empirical approach;

$$\beta = \frac{1}{\phi}\left(\frac{\partial\phi}{\partial P}\right)_T \tag{4-10}$$

β	Pore compressibility [default: 0 Pa^{-1}]
ϕ	Porosity [-]
P	Pressure [Pa]

Index T = Temperature [K]

4.4 Initial and boundary conditions

The tables 4-4 to 4-6 list the initial and boundary conditions used for the calculations.

4.4.1 Initial conditions

Table 4-4: Initial condition values

Material	Temperature [°C]	Gas phase pressure [Pa]	Porosity [-]	Saturation degree of the gas phase [-]	Saturation degree of the liquid phase [-]
Bentonite 1	20	$1\bullet10^{5}$	0.39	0.202	0.798
Bentonite 2			0.37	0.202	0.798
Solid rock			0.05	0.1	0.9
Pellets			0.57	0.789	0.211
Sand buffer			0.30	0.9421	0.06
Sand filter			0.36	0.9421	0.06
Concrete			0.3	0.5	0.5
Heater			-	0.98	0.02

Table 4-5: Initial condition values - continued

Material	Density [kg m^{-3}]	Intrinsic permeability –x direction [m²]	Intrinsic permeability –y direction [m²]	Intrinsic permeability –z direction [m²]
Bentonite 1	2750	$3.2\bullet10^{-21}$	$3.2\bullet10^{-21}$	$3.2\bullet10^{-21}$
Bentonite 2	2750	$3.2\bullet10^{-21}$	$3.2\bullet10^{-21}$	$3.2\bullet10^{-21}$
Solid rock	2700	$1.0\bullet10^{-21}$	$1.0\bullet10^{-21}$	$1.0\bullet10^{-21}$
Pellets	2500	$2.0\bullet10^{-19}$	$2.0\bullet10^{-19}$	$2.0\bullet10^{-19}$
Sand buffer	2500	$1.0\bullet10^{-15}$	$1.0\bullet10^{-15}$	$1.0\bullet10^{-15}$
Sand filter	2500	$2.0\bullet10^{-15}$	$2.0\bullet10^{-15}$	$2.0\bullet10^{-15}$
Concrete	2800	$1.0\bullet10^{-18}$	$1.0\bullet10^{-18}$	$1.0\bullet10^{-18}$
Heater	7800	-	-	-

4.4.2 Boundary conditions

Table 4-6: Fixed boundary condition (Dirichlet type) values for the model

Location in the model domain	Temperature [°C]	Gas phase pressure [Pa]	Saturation degree of the gas phase [-]
Outer boundary of the rock (drift contour)	20	$1\bullet10^{5}$	0.1
Drift boundary	20	$1\bullet10^{5}$	0.1

4.4.3 Power output

Power output data is adapted from ÅKESSON et al. (2007b) in order to simulate the different heat output values of heaters (1&2) including down times. The modified power output data is given in Table 4-7 and is shown in Appendix-2.

Table 4-7: Heater phases and failures in model domain

Time [Days]	Heater 1 - W [J/s]	Heater 2 - W [J/s]	Time [Days]	Heater 1 - W [J/s]	Heater 2 – W [J/s]
0.04	1108	1108	78.08	1847	1847
7.00	1477	1477	78.17	1847	1847
15.00	1847	1847	181.08	0	0
28.00	0	1847	181.33	1847	1847
28.90	1847	1847	216.04	1108	1108
61.63	0	1847	216.33	1847	1847
62.08	1847	1847	300.25	1108	1847
69.08	0	1847	300.38	1847	1108
69.17	1847	1847	300.42	1847	1847
72.38	0	1847	819.00	1847	1908
75.00	1847	1847	828.00	1847	1847

4.4.4 Water injection

The sand filter in the annular gap between bentonite and rock mass (see Figure 4-1) was filled by means of an injection pipe which ended at the bottom of the filter (injection level-1, x=0.85 m/ z=0.053 m). The water inflow rate was thus designated as a hydraulic boundary condition at the sand filter and set according to the following inflow diagram (Table 4-8). If the measured inflow rate was set to the in-situ data (Figure 4-6) in combination with the currently chosen initial conditions and material parameters, the model encountered stress peaks which in turn led to a program abort. Using the hydraulic parameter sets already mentioned above and a reduced water inflow rate, which corresponds to 85% of the measured rate which is valid until the day 240 (see Figure 4-5 and 4-6), at the day 74 a complete saturation of the sand filter is achieved in the thermal-only model. According to ÅKESSON et al. (2007b) the time for the complete filling of the sand filter is approximately 60-80 days. The development of the saturation in the sand filter is shown in Figure 4-5.

Table 4-8: Water inflow rates for the model at injection level-1 (x = 0.85 m/ z = 0.053 m)

Time [Days]	Water volume [L]	Enthalpy [J/kg]
0	0	83950
25	267	83950
73	286	83950
114	30	83950
240	198	83950
387	626	83950
658	2370	83950

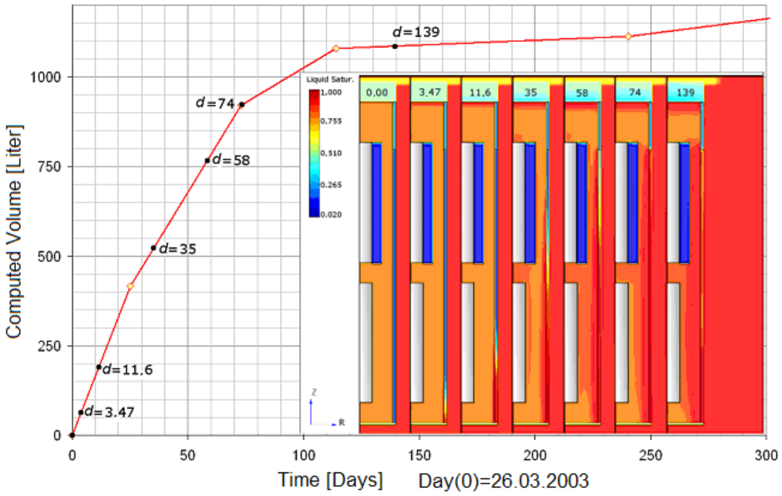

Figure 4-5: **Water inflow and time-dependent saturation of the sand filter (z = 0.25 m)**

Due to the developing of high gas pressure during the water injection along the sand filter, the top filter cell in the model is set to a fixed pressure (atmospheric pressure, 10^5 Pa) thus gas escaping is achieved. This adjustment allows to represent the upper tubes (injection level-2, z=6.775 m/ x=0.85 m) which have been introduced after the day 377 at the TBT site. According to the in-situ data, sand filter starts to be filled and pressurized through the upper tubes after the day 377. At TBT experiment filling and pressurization through different tubes and injection levels were applied on different time steps (ÅKESSON et al. 2007b) however, these incidents have not been considered in the model. For the duration of the simulations, the quantity and pressure of the water inflow was monitored continuously. During the filling phase, i.e. until the "complete" saturation of the sand filter and afterwards the pressure dropped numerous times due to injection level-2 (see Appendix-19).

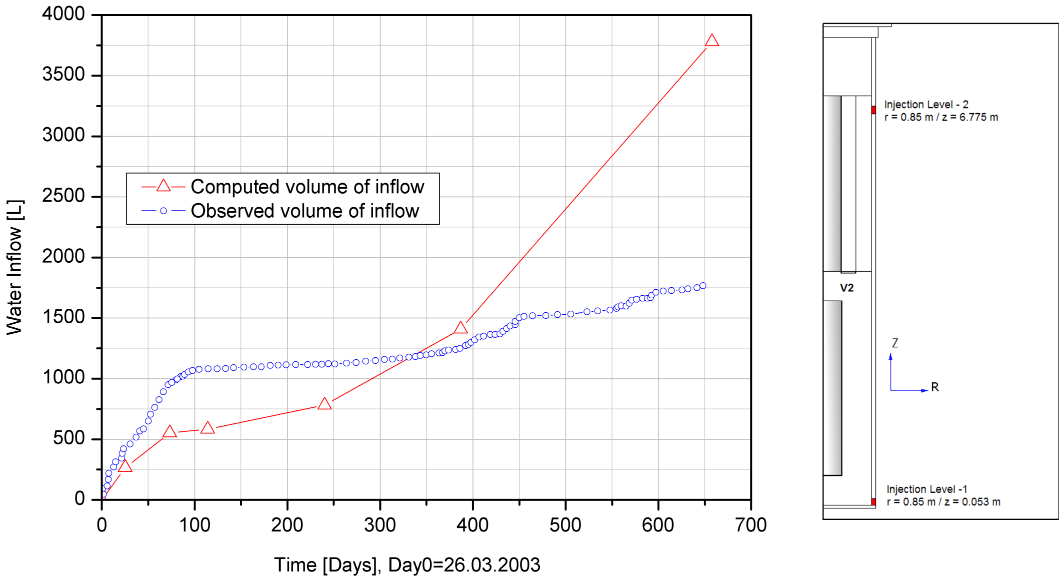

Figure 4-6: **Water inflow curves at sand filter (injection level-1, x = 0.85 m/ z = 0.053 m), comparison of computed and observed values**

4.5 Thermal back analyses

In the first run, all materials were initialized without capillary pressure properties and as a consequence, only the sand filter was saturated completely. The complete saturation lead to a pressure build-up in the sand filter which in turn initialized the saturation process in the surrounding bentonite. This first model version was chosen as a thermal boundary condition for subsequent calculations as the saturation has a significant influence on the thermal conductivity of materials. Based on this, further calculations were performed using variations of the saturation-dependent thermal conductivities and capillary pressure properties. These calculations resulted in the "best fit" parameters listed in Tables 4-1 up to 4-5. In the following figures (Figures 4-7 and 4-8) the measured (light color) and calculated (dark color with name *calc*) temperature curves are compared (ÅKESSON et al. 2007a). The comparison of measurement and calculation values was performed at the significant measurement points starting from the symmetry axis with the radii (r) 0.36 m (near heater, ring R4 - in bentonite-1) and 0.343 m (ring R10 - in sand buffer), approximately 0.542 m (ring R4 - in bentonite-1, ring R10 – in bentonite-2) and 0.78 m (near sand filter in bentonite-1 and bentonite-2).

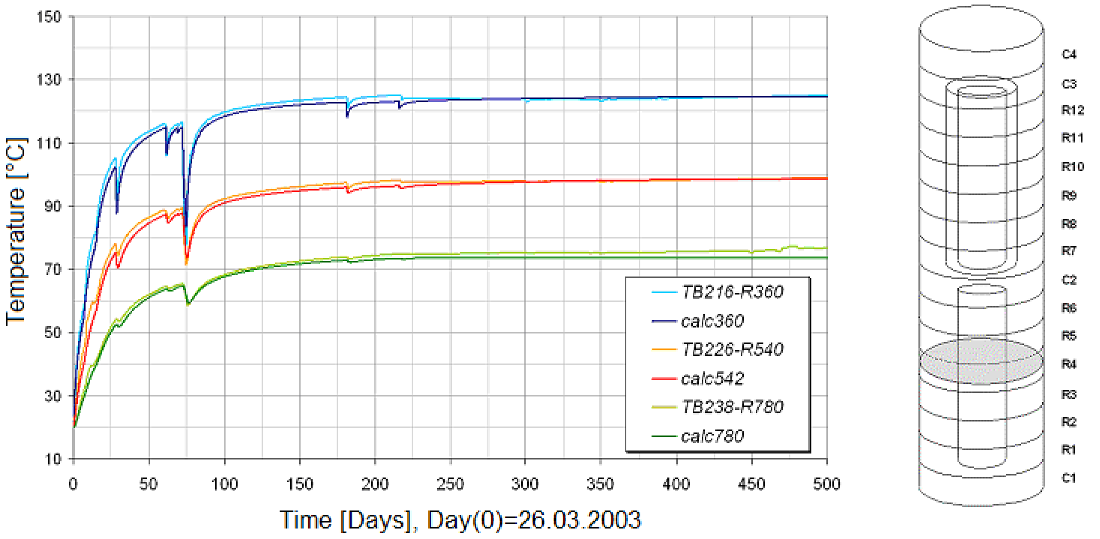

Figure 4-7: **Temperature curves at observation ring R4 (heater 1, z=2.45 m), Comparison of measured and computed values for different radii**

The measurement and calculation values show a very good fit in the area of the lower heater (measurement level heater 1, observation ring R4). The thermal conductivities in the model are saturation-dependent (as described, Table 4-1). The hydraulic approach is currently modeled using only one set of parameters per material (Table 4-2 and 4-3). A change in the saturation behavior of the sand filter would thus slightly effect the thermal conductivity.

The temperature comparison at observation ring R10 (measurement level heater 2) shows an underestimation of the temperature field in the bentonite until approximately day 250. This indicates that the initial saturation-dependent thermal conductivity in the sand buffer near the heater surface, which was set to λ_{dry}=0.4 W $m^{-1}K^{-1}$, was a bit too high. At later times, the computed temperature values in the area of the sand filter are significantly higher than the measured temperature values until simulation date t=150 days. For the rest of the calculation period (until day 500) the measurement and calculation values show a very good fit in the area of the upper heater (Figure 4-8) (ÅKESSON et al. 2007a).

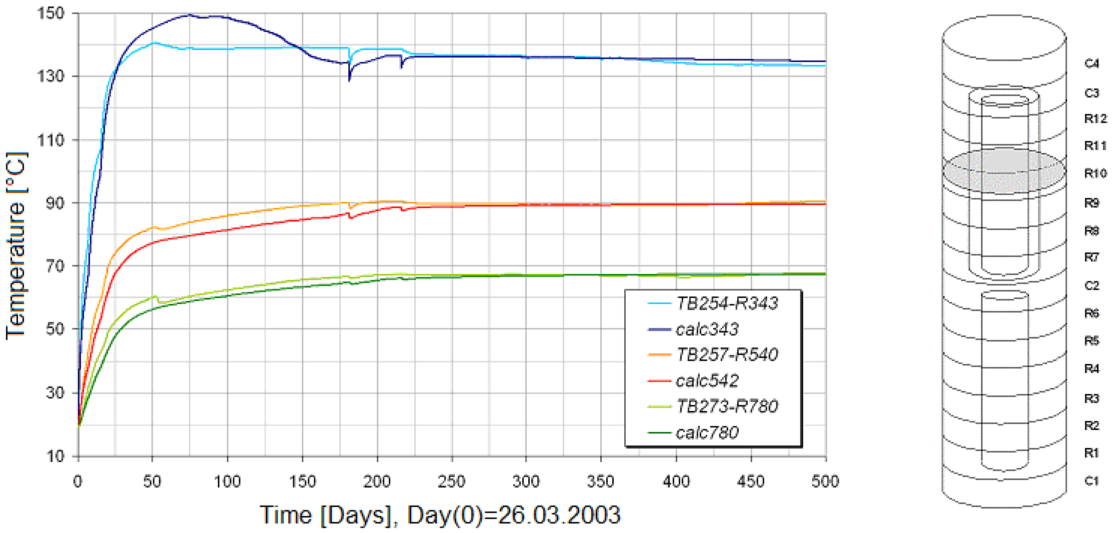

Figure 4-8: **Temperature curves at observation ring R10 (heater 2, z=5.95 m), comparison of measured and computed values for different radii**

Figure 4-9 presents the two-dimensional (2D) temperature evolution for thermal calculations (see Tables 4-1 to 4-8). In vertical and horizontal directions the temperature field shows a quite homogenous distribution except in sand buffer as it is intended. Along the sand buffer, heat flow is slowed down due to the low thermal conductivity of the sand buffer. Thus the temperature is significantly higher than in the other materials.

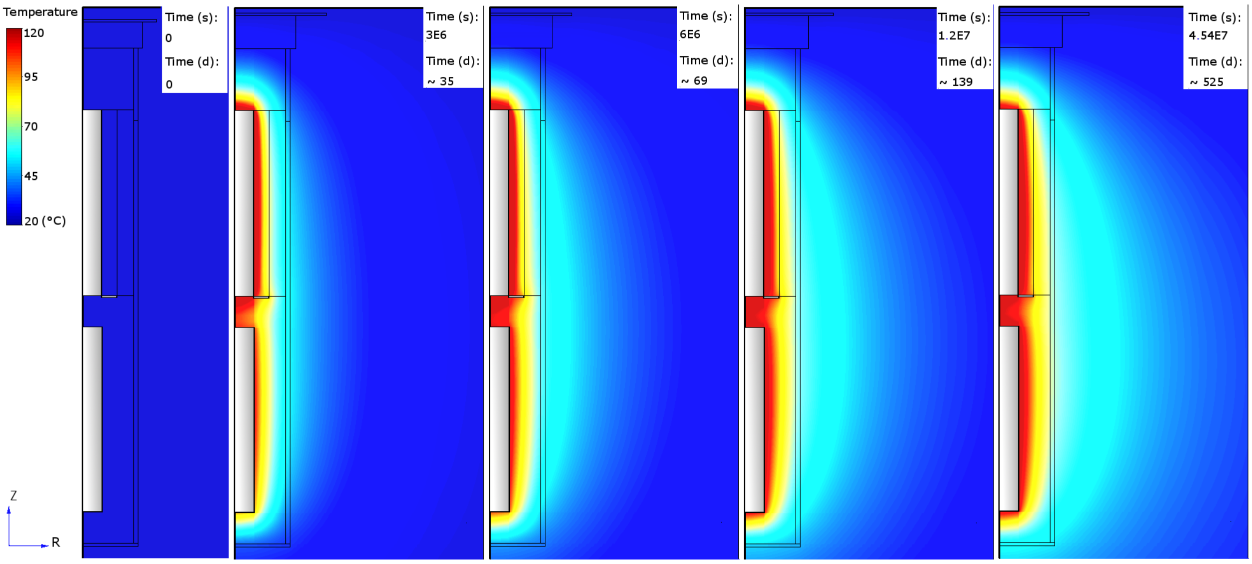

Figure 4-9: **2D isoline plots for temperature evolution in the model domain (thermal back analyses)**

During the calculations, temperature values were recorded continuously at the predetermined horizontal scan-lines (Appendix-13) and also filling process of the sand filter was recorded at the vertical scan-line V1 (Appendix-14&19). The horizontal lines start from the heater surface (r=0.305 m) and end at the contour of the solid rock (r=0.875 m). The vertical line starts at the upper edge of the base plate (z=0.00 m) and ends at the top of the sand filter (z=6.80 m). The analyses were performed at the following time steps: 0.12/ 1.16/ 11.6/ 46/ 74/ 116/ 266/ 521 days. One of the scan-line results is shown in Figure 4-11. In this figure the temperature curves show a decreasing trend for radial distances getting closer to the sand filter. However there is one exception at the time step t=74 days. This curve shows a sharp drop down due to the longest power failure (72-75 days) on heater-1 (see Table 4-7). At day 521 the maximum computed temperature value on the surface of the heater-1 is approximately 134.5°C (see Figure 2-3 for the in-situ values of temperature evolution and see Figure 4-12).

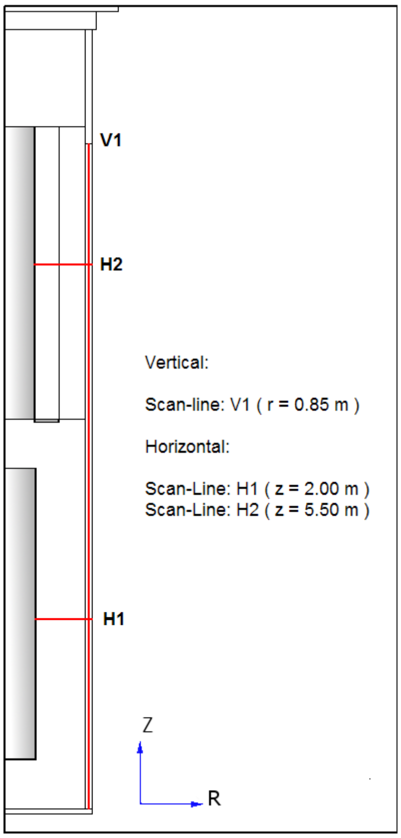

Figure 4-10: Cross-sectional view for vertical and horizontal scan-lines (thermal back analyses)

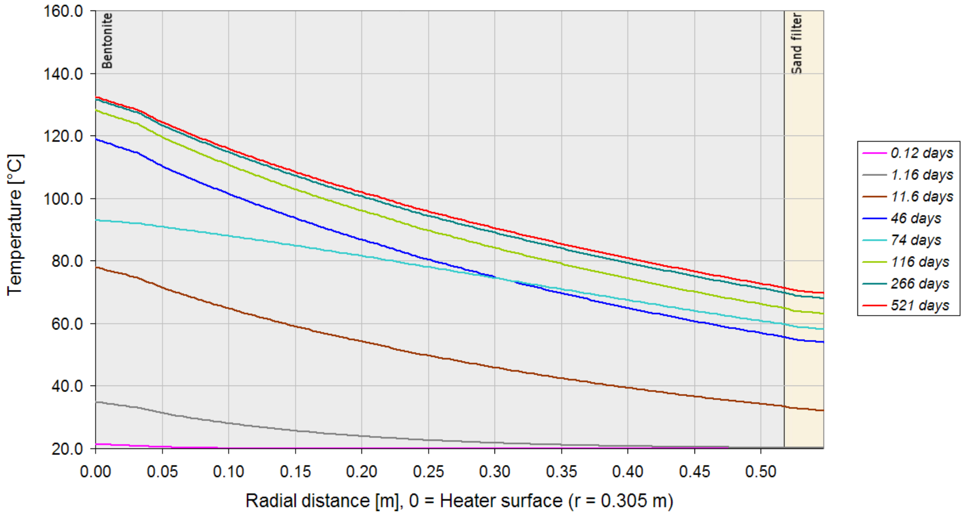

Figure 4-11 **Temperature evolution at the prescribed time steps along the scan-line H1 (thermal back analyses)**

In Figure 4-12 the computed and measured temperature values show a very good fit along the scan-line H-1 except in the range 0.3 – 0.4 m. Computed temperature values on the surface of heater-1 (r=0.3 m) is underestimated due to the model geometry adjustments.

As a main result it can be stated that, beside the deviations mentioned above in ring R10 (see Figure 4-8) during the very transient phase, the calculation results fit very well to the measurements. The validity of the computed temperature results were also proven by means of 2D isoline plots and scan-line figures. Thus, the temperature evolution in the TBT can be described sufficiently well.

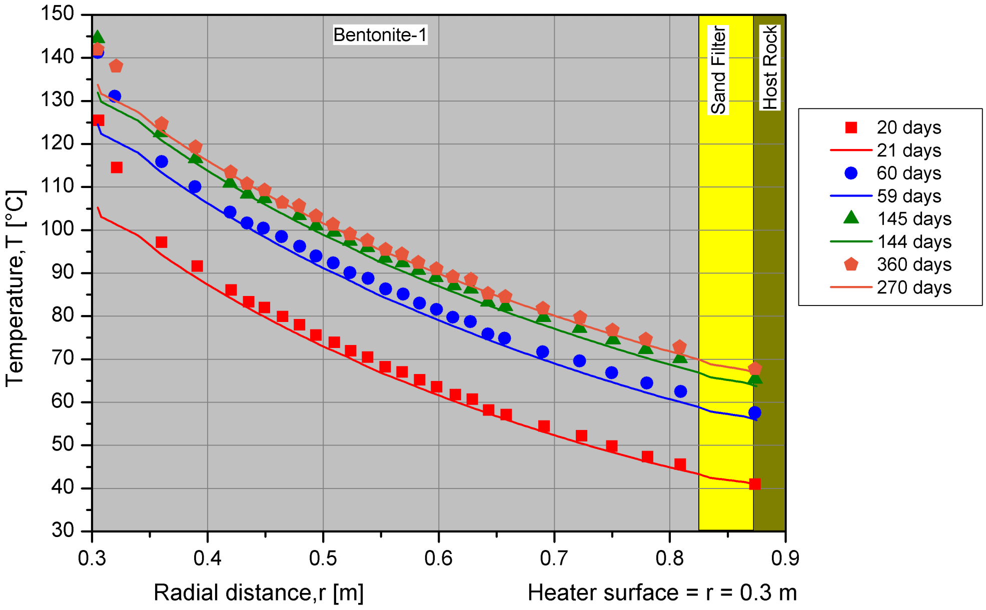

Figure 4-12 **Temperature curves along the scan-line H1, comparison of measured (points) and computed (lines) values on different time steps**

4.6 Hydraulic back analyses

During *thermal back analyses* (*Chapter 4.5*), computed capillary pressure (suction) results did still show deviations to the observed ones. In order to optimize this approach, some statistical methods were applied to analyze the parameter dependency of the capillary pressure. First, in the model domain, Bentonite–1 has been chosen for further hydraulic calibrations. During the analyses, approximately 250 simulations were carried out. Among all the sensors, the WB-215 (in Bentonite-1) is chosen as a reference location. Although this sensor has shorter observation time interval (approximately 800 days) than others, its measurement pattern is quite accurate and continuous (see Figure 4-16). (Åkesson et al. 2007b).

The work-flow during the analyses is to check the fit between the in-situ values of the specified sensor and simulation results via statistics. The parameter values from the thermal calculations (Model0038, *Chapter 4.3*) are considered as initial values for the sensitivity and for the residual analyses of the suction. Only one parameter at a time is selected and changed for a new calculation. This process continued until the end of analyzing all the parameters given below. Every numbered model represents a different value of a parameter. The most appropriate hydraulic parameters chosen for the analyses are listed below;

- Material properties:
  - Porosity Φ
  - Intrinsic permeabilities along the x and z directions; k_x , k_z
  - Pore compressibility; β
- Parameters in the relative permeability equation:
  - Van Genuchten`s notation m
  - Residual saturation of the liquid phase S_{lr}
  - Maximum saturation of the liquid phase S_{ls}
  - Residual saturation of the gas phase S_{gr}
- Parameters in the capillary pressure equation:
  - Van Genuchten`s notation m
  - Residual saturation of the liquid phase S_{lr}
  - Reciprocal of the gas (air) entry pressure P_0^{-1}
  - Upper boundary for the capillary pressure P_{max}
  - Maximum saturation of the liquid phase S_{ls}
- Initial conditions and source terms:
  - Actual saturation of the liquid phase S_L
  - Power of each of the heaters

4.6.1 Perturbation sensitivities - backward difference approximation

Backward sensitivity approximation method is adapted from POETER et al. (2005). It is one of the statistical method among perturbation sensitivities such as forward- and central- difference approximations. It is applied to analyze the effect of each parameter to the simulated variables. In backward difference approximation method, model(s) are executed once for each parameter and for each execution, one parameter value is slightly decreased (perturbed) from its unperturbed (unchanged) value, while the other parameter values are not perturbed (POETER et al. 2005). The modified formula of the backward sensitivity approximation below, presents the changing value of the simulated variable (here *absolute capillary pressure*) per decrement of the related parameter;

$$\frac{\Delta y'}{\Delta b} = \frac{1}{a}\sum_{j=1}^{a}\left(\frac{\frac{1}{n}\sum_{i=1}^{n}\left|y'(b)-y'(b')\right|_{t}}{\frac{(b-b')}{b}\times 100}\right)_{d} \qquad (4\text{-}11)$$

Δy´	[MPa] The change in the simulated value of the absolute capillary pressure caused by the parameter value change, b´; Δy´ = $\left|y'(b)-y'(b')\right|$
Δb	A vector in which all values are zero except for the one that corresponds to the variable (absolute capillary pressure) for which sensitivities are being calculated
y'(b)	[MPa] The value of the simulated variable, y`, calculated using the parameter values b
b	A vector (can be thought of as a list) of the estimated parameter values (S_L, S_{ls}, P_{max}, S_{lr}, S_{gr}, m, k_x, k_y, k_z, Φ / see Tables 4-2 to 4-5)
y'(b´)	[MPa] The value of y' calculated using the parameter values in b´
b´	Value of the parameter which is perturbed, b´= b (1-d)
a	Number of the decrements, here a is equal to 3 (90%, 45% and 10%)
n	Number of the simulation time steps, here n is equal to 4 (50,100,150 and 200 days)
d	Percent of the perturbation of the parameter for which sensitivities are being calculated, here d is equal to 0.90, 0.45 and 0.10 decrements

Table 4-9: The backward sensitivity values for the absolute capillary pressure. The change of absolute capillary pressure value per each parameter peturbation

Parameters		**Parameters**	**Backward sensitivity (Δy´/ Δb) [MPa]**
k_x	6.19	**S_{lr}- Rel.per.**	0.03
k_z	0.03	**S_{ls} - P_{cap}**	Not Available*
m - P_{cap}	3.84	**S_{ls} - Rel.per.**	0.98
m - Rel.per.	7.81	**P_{max} - P_{cap}**	0.54
S_{gr}	0.02	**P_o^{-1} - P_{cap}**	2.90
S_L	17.18	**Φ**	2.59
S_{lr} - P_{cap}	0.01		

(Note: * related parameter is not able to be handled with this method because several program crashes occurred during the sensitivity analyses therefore short term results are acquired then its value remained unchanged)

According to Table 4-9, the most sensitive parameters for the suction are respectively; *Saturation of the liquid phase* S_L, *Van Genuchten`s notation for relative permeability m (Rel.Per.)* and *intrinsic permeability along the x-direction* k_x.

4.6.2 Parameter variation sensitivity

Along with the *backward sensitivity concept*, the parameter variation sensitivity method is employed. In Figures 4-13, 4-14 and 4-15, the sensitivity of absolute capillary pressure to corresponding parameter variations is shown. The ratio of the parameter variation indicates the ratio between the final value of the related parameter to its initial (raw) value. The initial value always refers to the final adjusted parameters of the thermal calculation model (see Chapter 4.3).

$$\alpha = \frac{\alpha_{Final}}{\alpha_{Initial}} \qquad (4\text{-}12)$$

α	Ratio of the parameter variation that has influence on the variable (absolute capillary pressure)
α_{Final}	Final value of the related parameter that has influence on the variable
$\alpha_{Initial}$	Initial value of the related parameter that has influence on the variable (see Tables 4-2, 4-3, 4-4 and 4-5)

Finally, the sensitivity of absolute capillary pressure against the variation of parameters was analyzed. In Figures 4-13, 4-14 and 4-15 as long as α=1, a parameter which has influence on the variable (absolute capillary pressure) keeps its initial value and showing no deviation. When the associated line of a parameter is showing increasing or decreasing trend along the y-axis then the value of absolute capillary pressure is giving different results as a response to the variation of this parameter along the x-axis. It can be stated that the rougher and steeper the pattern of a parameter, the higher the sensitivity of absolute capillary pressure to this parameter.

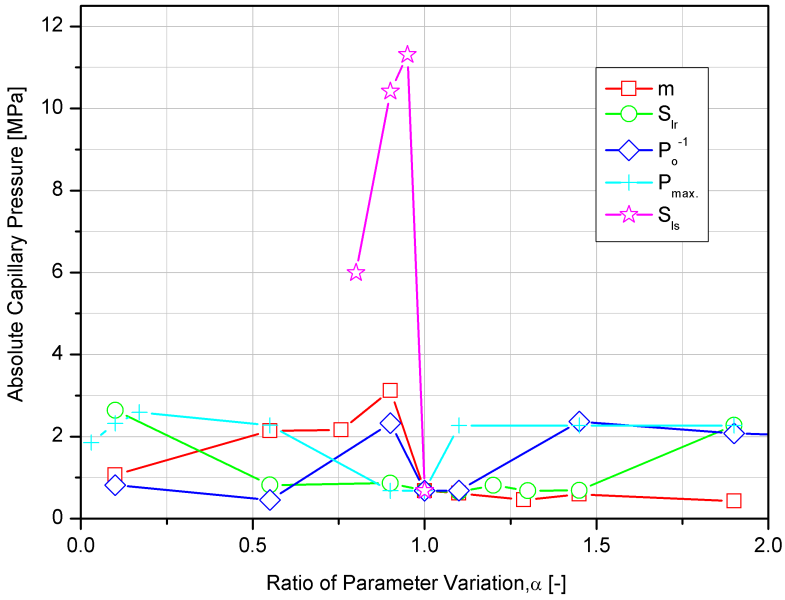

Figure 4-13: Sensitivity of absolute capillary pressure to the coefficients from Table 4-2

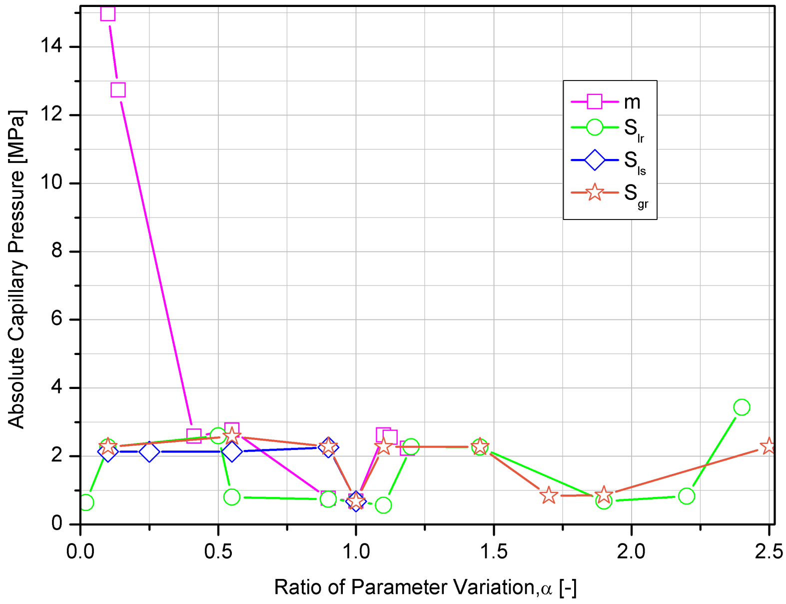

Figure 4-14: Sensitivity of absolute capillary pressure to the coefficients from Table 4-3

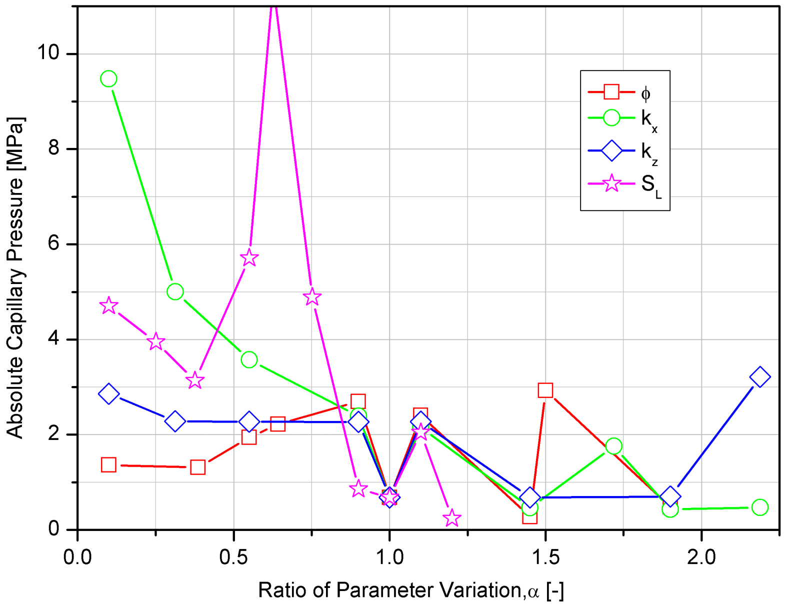

Figure 4-15: Sensitivity of absolute capillary pressure to the other hydraulic parameters from Table 4-4 and 4-5

According to Figures 4-13, 4-14 and 4-15, the most sensitive parameters are; *maximum liquid phase saturation for capillary pressure function* S_{ls} *(*P_{cap}*)*, *Van Genuchten`s notation for relative permeability m (Rel. per.)*, *intrinsic permeability along the x-direction* k_x and *saturation of the liquid phase* S_L.

4.6.3 Residual calculations

In order to obtain the best fit between the observed and computed capillary pressure values the method; *sum of the absolute values of un-weighted residuals* is adapted from SCHAAP and VAN GENUCHTEN (2005):

$$O_{Pcap}(p) = \frac{1}{N_{Pcap}} \sum_{i=1}^{N_{Pcap}} \left| P_{cap,i} - P`_{cap,i} \right| \tag{4-13}$$

O_{Pcap} Objective function for absolute capillary pressure [MPa]

p Parameter vector (S_L, S_{ls}, P_{max}, S_{lr}, S_{gr}, m, k_x, k_y, k_z, Φ)

$P_{cap,i}$ Measured absolute capillary pressure value [MPa]

$P`_{cap,i}$ Simulated absolute capillary pressure value [MPa]

Index i = number of the prescribed time steps (t = 50, 100, 150 and 200 days), i = 1,4; N_{Pcap} = Number of simulated absolute capillary pressure values per simulation session (minimum 1, maximum 4)

The objective function for absolute capillary pressure indicates the accuracy of the fitting for each parameter change. To obtain identical measured and simulated curves of absolute capillary pressure evolving with time, the objective function value must be as small as possible.

In case the objective function is zero, the measured and simulated curves are overlapping each other which does not correspond with reality.

For every simulation session and four prescribed time steps (t=50, 100, 150 and 200 days) residuals were calculated in order to obtain the most convenient parameter value(s) for the hydraulic calibration. It should be mentioned that one simulation session indicates an individual parameter change while other parameters, listed in the Section *4.3*, stay unchanged (see also Tables 4-2, 4-3, 4-4 and 4-5).

Although the parameters *saturation of the liquid phase* S_L, *porosity* Φ and *intrinsic permeability* k_x present smaller residual values than the others, they are material specific. Therefore empirical parameters such as *upper boundary for the capillary pressure* P_{max}, *reciprocal of the gas (air) entry pressure* P_o^{-1} and *Van Genuchten`s notation for capillary pressure* m (P_{cap}) were used for further fitting calculations. It has to be considered that P_{max} is an adjusted limit which constrains the possible higher capillary pressure values during simulations. Using these three selected parameters, combined models were created for further fine tuning. These indicate the simultaneous change of two or three predefined parameters $(P_{max}$, P_o^{-1} and m $(P_{cap}))$ while the others stay unchanged (see Table 4-11).

Table 4-10: Mean residual values, O_{Pcap} *(p)* for the simulation sessions

Parameters	**Best calculation values**	**Mean residuals, O_{Pcap} (p) [MPa]**	**Simulation sessions [No.]**
S_L	0.8778	0.249	TBT-1
S_{ls} (P_{cap}) *	1.00	1.531	TBT-2
P_{max}	$9 \bullet 10^6$ Pa	0.375	TBT-3
S_{lr} (P_{cap})	0.0011	1.524	TBT-4
m (P_{cap})	0.363	1.498	TBT-5
S_{gr}	0.25	1.523	TBT-6
k_x	$7 \bullet 10^{-21}$ m^2	0.472	TBT-7
k_z	$2.88 \bullet 10^{-21}$ m^2	1.523	TBT-8
P_o^{-1}	$1 \bullet 10^{-7}$ Pa^{-1}	0.464	TBT-9
S_{lr} (Rel. per.)	0.095	1.516	TBT-10
m (Rel. per.)	0.72	1.476	TBT-11
S_{ls} (Rel. per.)	1.00	1.531	TBT-12
Φ	0.15	0.365	TBT-13

(Note: ***** S_{ls} (P_{cap}) was not able to be handled with this method)

Considering the complexity of the two-phase flow computations at the model domain, this analysis is not sufficiently wide-ranging and requires more and extended calculations to cover the adequate range of the absolute capillary pressure values.

Table 4-11: Mean residual values, O_{Pcap} *(p)* for the combined models

Simulation sessions [No.]	Parameter values	Mean residuals, O_{Pcap} (p) [MPa]	Combination models
TBT-14	$P_{max} = 9\bullet 10^6$ Pa $P_o^{-1} = 1\bullet 10^{-7}$ Pa^{-1}	0.464	TBT-3 TBT-10
TBT-15	m (P_{cap}) = 0.3630 $P_{max} = 9\bullet 10^6$ Pa	0.406	TBT-5 TBT-3
TBT-16	m (P_{cap}) = 0.3630 $P_o^{-1} = 1\bullet 10^{-7}$ Pa^{-1}	0.499	TBT-5 TBT-10
TBT-17	m (P_{cap}) = 0.3630 $P_o^{-1} = 1\bullet 10^{-7}$ Pa^{-1} $P_{max} = 9\bullet 10^6$ Pa	0.521	TBT-5 TBT-10 TBT-3

4.6.4 Analyses of the results

According to the sensitivity analyses mentioned above, the most sensitive hydraulic parameters for the capillary pressure are; *saturation of the liquid phase S_L, Van Genuchten`s notation m (for relative permeability)* and *intrinsic permeability along the x direction k_x*, in turn. Both of the sensitivity analyses are giving consistent results indicating a good reliability. By means of the sensitivity analyses and the residual error calculation, TBT-3 is selected as a best fit model for the sensor WB-215. In Figure 4-16 computed and measured values show a good fit except a small overestimation which is due to the unpreventable high suction in the simulation. Computed values show a small drying cycle which takes place between 70th and 90th days, as well as measured values. This incident may happen due to the beginning of pressure drop in injection level-2. Appendices 3 through 8 show the best fit models for other suction sensors.

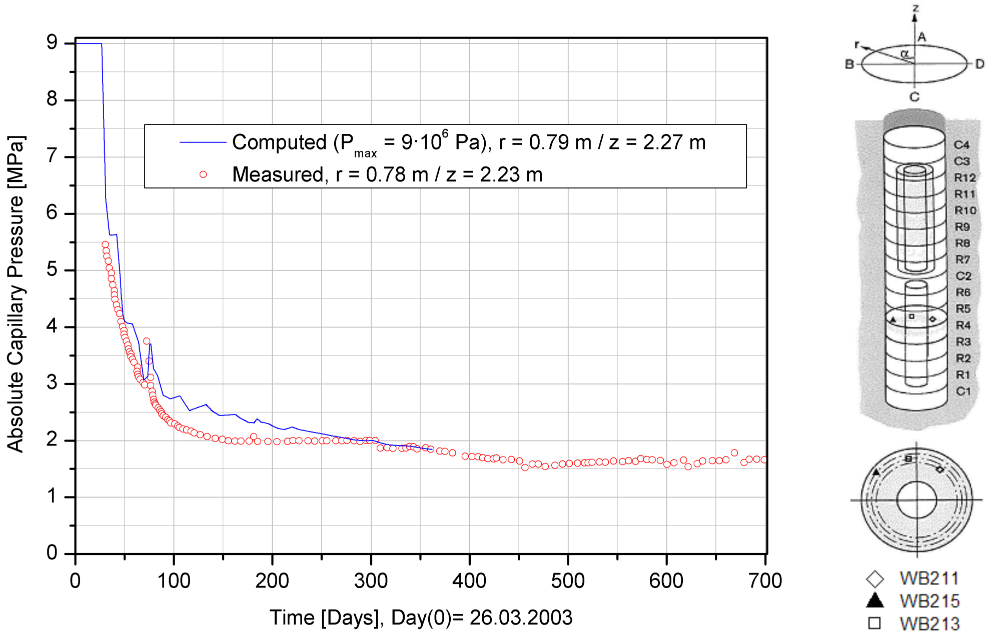

Figure 4-16: Absolute capillary pressure curves at the suction sensor WB-215, comparison of measured and computed values

For the purpose of comparison at the predefined horizontal and vertical scan-lines (Figure 4-17), absolute capillary pressure and liquid phase saturation values were recorded. The vertical line starts at the upper edge of the base plate (z=0.00 m) and ends at the bottom of the bentonite-2 (z=4 m). The horizontal line starts at the intersecting line between the bentonite-1 and heater-1 (r=0.305) and ends at the surface of the sand filter (r=0.825). In order to compare the simulation results between thermal-only and hydraulic calibration models, the most comprehensive time steps are chosen. Therefore the analyses were performed at the following time steps: 0.01/ 11.6/ 57.9/ 115.7 days. In Figures 4-18 and 4-19 evolution of absolute capillary pressure and liquid phase saturation values along the scan-line H3 for the prescribed time steps are shown. In Figure 4-18, it can be observed that thermal-only calibrated model yields higher suction than the hydraulic calibration model. Moreover, according to Figure 4-19 bentonite-1 seems to be slower saturated within the hydraulic calibration model than the thermal-only model, which occurs due to the suction decrease. Along the scan-line H-3, when it is getting closer to sand filter, liquid saturation shows higher and concurrently suction shows lower values due to the filling of bentonite through the injection level-1. Appendix-15 show the results for the other scan-line, V2.

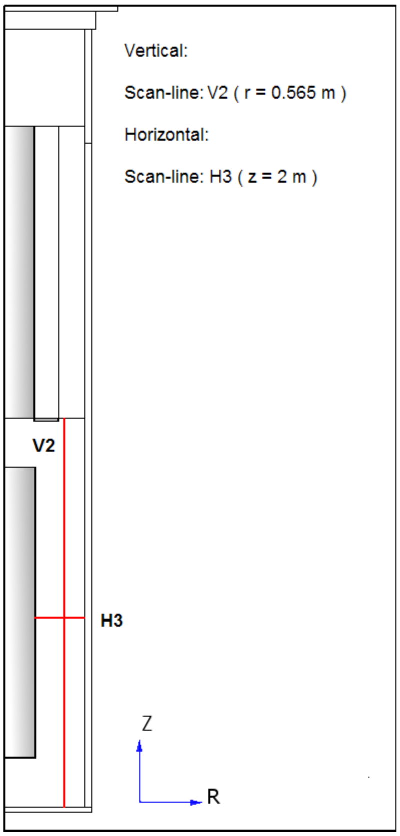

Figure 4-17: Cross-sectional view for vertical and horizontal scan-lines (hydraulic back analyses)

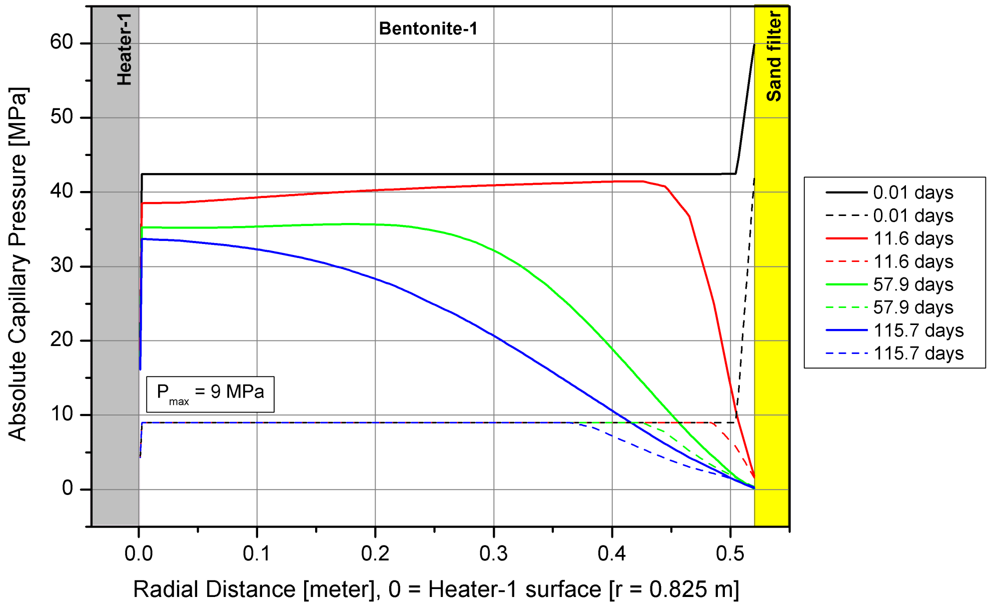

Figure 4-18: **Absolute capillary pressure curves along the scan-line H3, comparison of thermal-only model (solid lines, Model0038) with hydraulic calibration model (dashed lines, TBT-3) results for the prescribed time steps (hydraulic back analyses)**

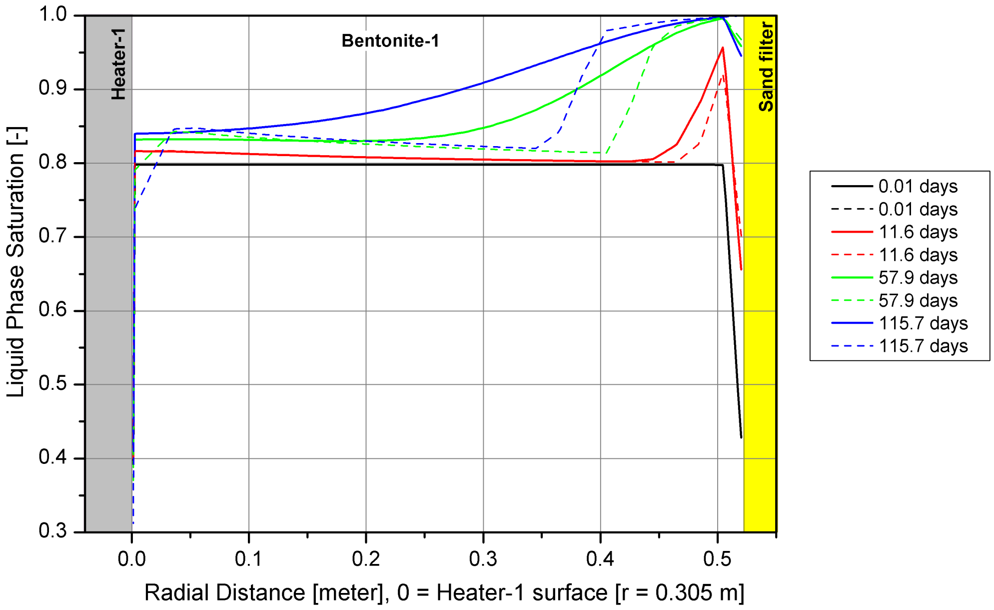

Figure 4-19: **Liquid phase saturation curves along the scan-line H3, comparison of thermal-only model (solid lines, Model0038) with hydraulic calibration model (dashed lines, TBT-3) results for the prescribed time steps (hydraulic back analyses)**

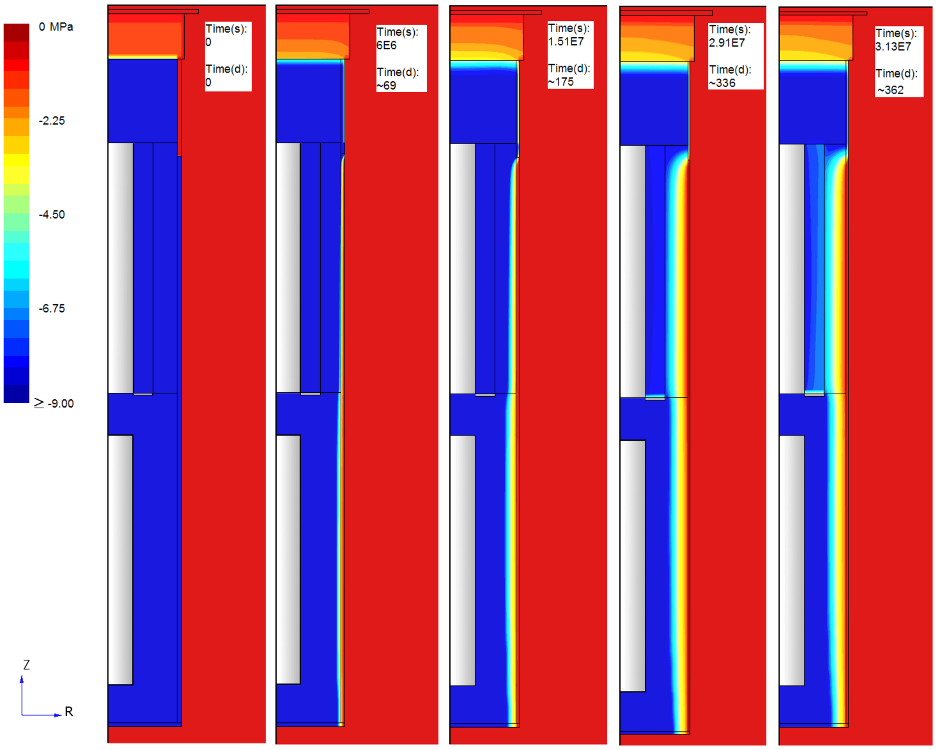

Figure 4-20: **2D isoline plots for suction evolution in the model domain (hydraulic back analyses, TBT-3)**

Figure 4-20 presents the two-dimensional (2D) suction evolution for hydraulic calculations (see Tables 4-2 to 4-5 and Table 4-10 for final parameter adjustment of suction). It should be reconsidered that capillary pressure depends on the liquid phase saturation (see Table 4-2) hence suction isolines are consistent with liquid saturation evolution. In bentonite, suction decreases gradually with the water inflow through the injection level-1 (see also Figures 4-18 and 4-19). In the Figure 4-20 on time step t=175 days, bentonite-2 shows higher suction values than bentonite-1 due to the parameter adjustments done in the hydraulic part (see *Chapter 4.6.3*). On the day 336, suction isolines in the zone between sand buffer and bentonite-2 show a wide spread compare to bentonite-1. This can be explained with the large difference between the intrinsic permeabilities of sand buffer and bentonite –2 (see Table 4-5).

Finally it can be concluded that, except the overestimation of calculated suction values for the sensor WB-235 (see Appendix-8) the calculation results fit very well to the measurements. The computed capillary pressure and liquid saturation results were shown on 2D isoline plots and scan-line figures, illustrating that the suction and liquid phase saturation evolutions in the TBT can be described sufficiently well.

4.7 Temperature effect on capillary pressure

In order to illustrate the influence of temperature on capillary pressure and liquid saturation in the model domain, different power values for each simulation session were set as a constant parameter except for the *unsteady heating regime* setting which contains the power values from the thermal-only model (see Table 4-7). As a reference value for comparing the capillary pressures, values calculated on the time step t=150th day is used and results are given in Figures 4-21 and 4-22. In these figures it can be seen that the dependency of capillary pressure on temperature is inversely proportional, but the dependency of liquid phase saturation on temperature is directly proportional. Due to the R-square values, linear dependency of suction on temperature seems to be stronger than liquid saturation on temperature. Figure 4-23 shows the range of liquid saturation as a result of different power values (temperatures) which is roughly equal to 0.0125.

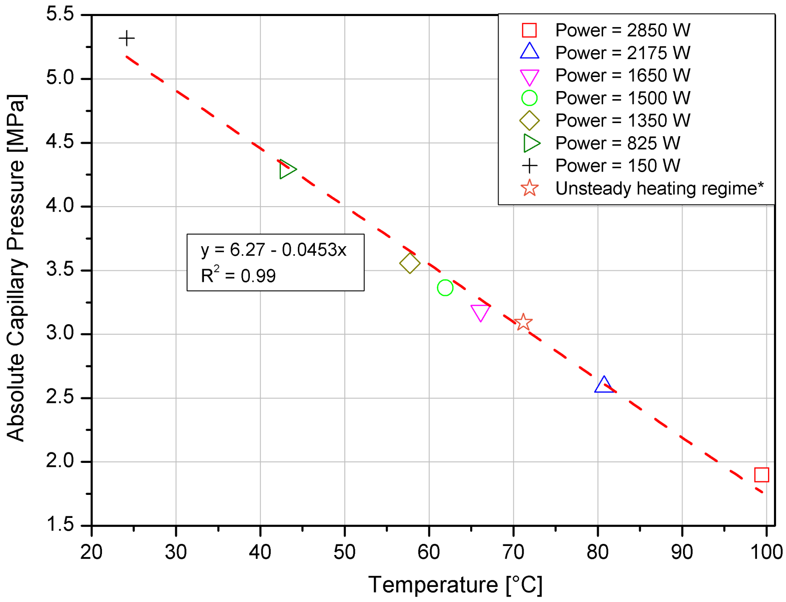

Figure 4-21: Scatter diagramme of absolute capillary pressure and power (temperature) coupling, points are calculated on the prescribed time step 150th day and at the suction sensor WB-215

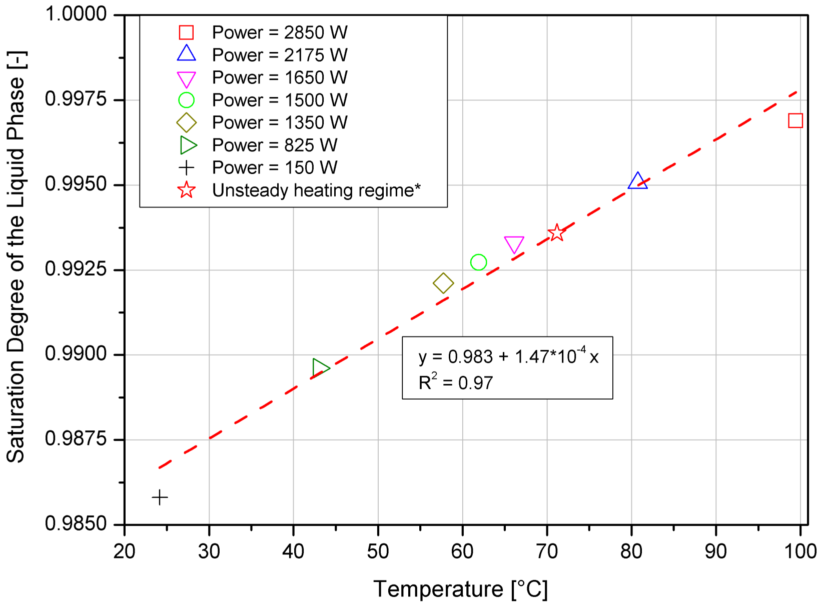

Figure 4-22: **Scatter diagramme of liquid phase saturation and power (temperature) coupling, points are calculated on the prescribed time step 150th day and at the suction sensor WB-215**

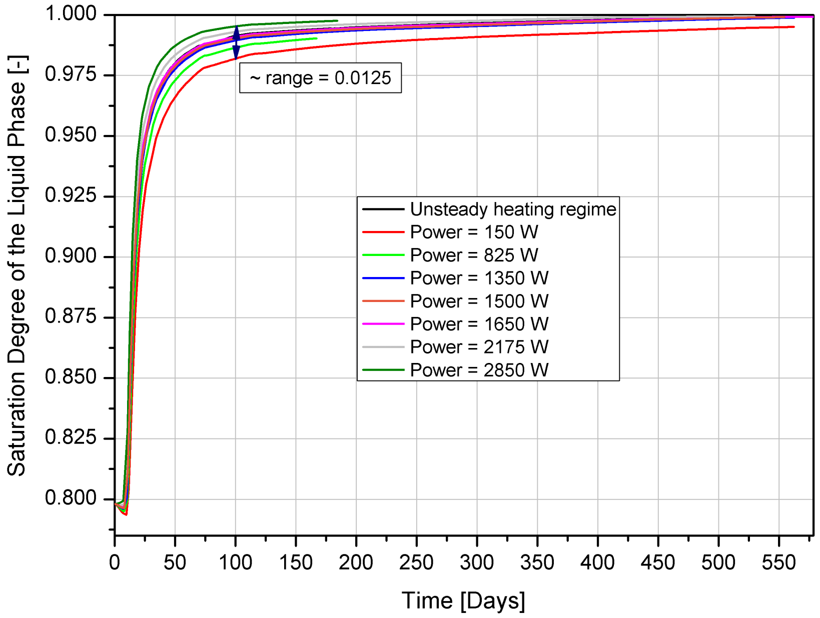

Figure 4-23: **Evolution of liquid phase saturation curves for different power (temperature) values at the suction sensor WB-215**

(Note: * *Unsteady heating regime* is taken from the Table 4-7)

Looking at the significant change of capillary pressure as a function of simulated temperature environment (Fig. 4-21), a short review for explanation is obviously required. The temperature dependency of the capillary pressure itself is mainly defined by the surface tension at the water-air interface in a porous medium and its contact angle (BEAR 1972). Intensive investigations have been performed by (GRANT & SALEHZADEH 1996) as well as (SHE & SLEEP 1998). Besides their own experiments they did a literature review and concluded that the contact angle is less sensitive on temperature than the surface tension (σ) which can be described as a linear relationship (GRANT & SALEHZADEH 1996):

$$\sigma = c_1 + c_2 T \qquad (4\text{-}14)$$

σ	Surface tension (N m^{-1})
c_1	Empirical constant (0.11766 N m^{-1})
c_2	Empirical constant ($-1.535 \cdot 10^{-4}$ N $m^{-1}K^{-1}$)
T	Temperature (K)

As shown in Figure 4-21 the capillary pressure decreases with increasing temperature down to about 1.7 MPa at the reference point due to change of saturation. Using equation (4-14) the capillary pressure at the reference point would go down to about 4.5 MPa only in case of constant saturation. This indicates that the saturation change is the dominant factor for capillary pressure change in this case.

In the code TOUGH2, there are three parameters that are temperature dependent. These are; phase viscosity (μ_β) and phase density (ρ_β) in the Darcy flux, and coefficient of binary gas diffusion ($d_\beta{}^\kappa$) in the hydrodynamic dispersion flux via molecular diffusion (PRUESS et al. 1999, KRÖHN 2004, THUNDERHEAD ENG. 2007);

$$u_\beta = -k\frac{k_{r\beta}}{\mu_\beta}\left(\nabla P_\beta - \rho_\beta g\right) \qquad (4\text{-}15)$$

$$d_\beta{}^\kappa(P,T) = d_\beta{}^\kappa(P_0,T_0)\frac{P_0}{P}\left[\frac{T+273.15}{273.15}\right]^\theta \qquad (4\text{-}16)$$

Fluid dynamic viscosity as well as fluid density are considerably temperature dependent. For liquid phase, the higher the temperature the lower the viscosity and density. The viscosity change is significantly higher and thus most dominant with regard to water mobility (BUSCH et al. 1993). The higher saturation at increased temperature at the reference point is mainly due to the lower liquid viscosity yielding a faster liquid migration and thus a higher saturation at the reference point being the reason for lower capillary pressure.

Investigations show that, in addition, there seems to be a slight temperature dependency of the residual liquid saturation (S_{lr}) leading to a different shape of the soil-water-retention curve (SHE & SLEEP 1998). The above described sensitivity analyses have shown a slight sensitivity of capillary pressure on residual liquid saturation (Figures 4-13 and 4-14). Thus further investigations on this topic are recommended.

Figure 4-24 shows the computed temperature evolution curves for different suction settings at the suction sensor WB215. It is obvious that, in bentonite-1 temperature evolution is independent from suction so capillary pressure seems to have no influence on temperature evolution. The curves showing the relations between the molecular diffusion, pore compressibility and absolute capillary pressure can be found in Appendices 9 and 10 respectively.

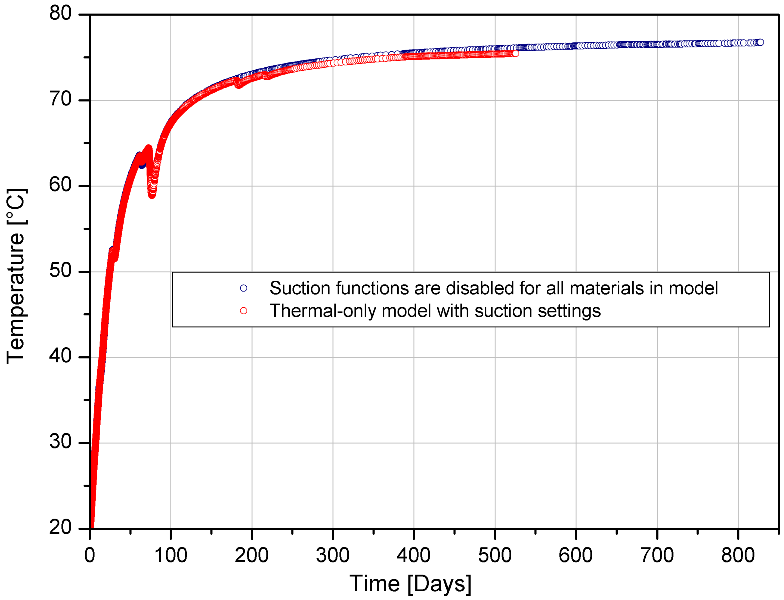

Figure 4-24: **Computed temperature curves for different suction settings at sensor WB215**

Even the temperature increase in the engineered barrier of TBT and also in a real repository is very fast compared to the fluid migration velocity - the thermal transient phase is roughly about 6 months. The influence of all temperature dependent components should carefully be evaluated. This seems to be important in order to make sure that the applied constitutive law describes the processes most suitable, especially when applied in a repository safety case.

5 CONCLUSIONS AND OUTLOOK

In the framework of Temperature Buffer Test (TBT) at the Äspö URL two canisters of 3000 mm in length and 610 mm in diameter, equipped with heating elements have been emplaced in a deposition borehole of 8.0 m depth and 1.75 m borehole diameter. Two different buffer designs are considered: The lower canister is covered by a bentonite buffer, the upper canister is covered by a sand buffer and a bentonite buffer respectively. This is the first test of a bentonite barrier under a thermal load of more than 100°C using both pure bentonite and a sand-bentonite layered buffer construction.

Measurement data are available for total pressure, pore water pressure, suction, relative humidity and temperature at different points around the upper and the lower canister in the buffer and in the host rock. However it is realized that the majority of suction sensors keep delivering signals in spite of fully saturation with the liquid phase. Supplementary measurements of forces and displacements on the plug, inflow of water, power output for the heaters and injection pressure on the filter tips are performed too. A few optical pressure and temperature sensors (8 sensors) have been installed for evaluation purposes. According to the latest in-situ data updates, 3 of 4 fiber optic sensors are out of order. Being installed in a strong temperature gradient, the temperature compensation of the pressure signal caused significant problems and some doubts in the absolute accuracy are still remaining.

Several laboratory tests have been performed on the bentonite covering the canisters. The thermal conductivity, thermal diffusivity, specific heat capacity and the heat expansion (shrinkage) were determined on samples with evolving temperature for different water contents. For the evolution of thermal conductivity and thermal diffusivity with temperature, polynomial fitting functions have been determined and applied in the simulations. For thermal conductivity and thermal expansion, significant dependencies on water contents were observed. For the specific heat capacity a linear regression was obtained at predefined water content values at a constant temperature T=30°C.

For modeling of the Temperature Buffer Test, stepwise back analyses have been applied. Due to the fact that the temperature is the driving force for a thermo-hydro-mechanical behavior, the temperature evolution was simulated first. As a result of the laboratory investigations, saturation dependent thermal conductivities of the bentonite have been considered. Thus, a suitable simulation of the saturation process is required and saturation dependent permeabilities and capillary pressure functions using the Van Genuchten model for two-phase flow conditions have been applied. For comparison and fitting of measured and calculated temperatures, sensors around both canisters in rings R4 and R10 located at different radii (0.343, 0.36, 0.542 and 0.78 m) have been used and a set of best fit parameters was found (see Tables 4-1 to 4-5). Besides some deviations in the very transient phase, the temperature evolution within the Temperature Buffer Test can be described sufficiently well.

During the second part of the model calculations, the hydraulic back analyses are performed focusing on the capillary pressure determination. By using residual calculations subsequent to sensitivity analyses, plausible fits (except at sensor WB235) ranging between 0 to 2.5 MPa were obtained for the suction sensors WB205, WB215, WB218, WB220, WB228 and WB230. For this analysis the most transient phase up to day 358 was used. In close vicinity to the modeled heater cells when the saturated vapor pressure of bulk aqueous phase (P_{sat}) exceeds the total pressure, convergence problems arise due to the fact that validity limit for the used EOS3 module for vapor pressure handling was exceeded. For further modeling works, the use of EOS4 module which includes the feature so called *vapor pressure lowering due to capillary and phase adsorption effects* is recommended.

Molecular diffusion normally has insignificant effect on subsurface flow processes. However, when advective velocities are small, e.g. water movement in bentonite with suction, then it may become an important mechanism (see Appendix-9). Diffusion effect(s) on suction should be deepened for further work. In addition, the influence of temperature on suction is recommended to be considered more deeply, since a couple of parameters are temperature dependent. Even though the dependence of most of them is rather small, in combining their effects this might lead to unexpected deviations in long term predictions.

The calculation shows that TOUGH2 is principally suited for the application to the thermo-hydraulic (TH) aspects of the "Temperature Buffer Test". However, a fully coupled thermo-hydro-mechanical (THM) calculation is not possible with this program and requires the use of different software or the combination with a mechanical calculation model. A combination of FLAC3D and TOUGH2 would be a possible option for future work. Furthermore the use of simulation integrated inverse modeling methods seems reasonable to compare the results with the variable integrated ones like the methods employed in *Chapters 4.6.1, 4.6.2* and *4.6.3*. An application of the ITHOUGH (Inverse TOUGH) computer code may result in a significant progress.

6 REFERENCES

Åkesson M., Hökmark H., Fälth B. (2004): Temperature Buffer Test (TBT) modeling program Step 2, Clay Technology AB, Lund, Sweden.

Åkesson M. (2006a): Äspö Hard Rock Laboratory (HRL), Temperature Buffer Test (TBT) – evaluation modeling - field test , SKB IPR-06-10, Clay Technology AB, p. 297, Sweden.

Åkesson M. (2006b): Äspö Hard Rock Laboratory (HRL), Temperature Buffer Test (TBT) - evaluation modeling – mock-up test, SKB IPR-06-11, Clay Technology AB, p. 121, Sweden.

Åkesson M., Goudarzi R., Hökmark H. (2006c): Äspö Hard Rock Laboratory (HRL), Temperature Buffer Test (TBT) – sensor data report, Report No: 8 (Period 26.03.03 - 01.07.06), SKB IPR-06-27, Clay Technology AB, p.105, Sweden.

Åkesson M., Hökmark H., Goudarzi R. (2007a): Äspö Hard Rock Laboratory (HRL) Temperature Buffer Test (TBT) - sensor data report, Report No: 9, SKB IPR-07-07, Clay Technology AB, p.97, Sweden.

Åkesson M., Goudarzi R., Hökmark H. (2007b): Äspö Hard Rock Laboratory (HRL), Temperature Buffer Test (TBT) – sensors data report, Report No: 10 (Period 26.03.03 - 01.07.07), SKB IPR-07-21, Clay Technology AB, p.97, Sweden.

Bear J.A. (1972): Dynamics of Fluids in Porous Media, Elsevier, New York USA.

Borradaile G. J. (2003): Statistics of earth science data: Their distribution in space, time, and orientation, Springer, p.152, Heidelberg Germany.

Buntebarth G. (2004): Bestimmung Thermophysikalischer Eigenschaften an Bentonit-Proben, Technischer Bericht, Geophysikalisch-Technisches Büro, Clausthal-Zellerfeld Germany.

Busch K.-F., Luckner L., Tiemer K. (1993): Geohydraulik, Lehrbuch der Hydrogeologie, Band 3, Gebrüder Bornträger, pp. 48-49, Berlin/Stuttgart Germany.

Börgesson L. (1982): Buffer Mass Test, Predictions of the Behavior of the Bentonite-Based Buffer Materials, Series: Stripa Project, p.92, Stockholm Sweden

Börgesson L. (1992): Interaction between Rock, Bentonite Buffer and Canisters - FEM calculations of some mechanical effects on the canister in different disposal concepts, Technical Report SKB 92-30, Clay Technology AB, p.83, Lund, Sweden.

Corey A. (1954): The Interrelation Between Gas and Oil Relative Permeabilities, Producers Monthly, Vol. 19: 38-41.

Couture W., Jomaa W., Puiggali J.-R.(1996) : Relative permeability relations, A key factor for a drying model, Transport in Porous Media Journal, Vol. 23, No. 3: 303-335, Springer Netherlands.

Fatt, I. and Klikoff W.A. (1959): Effect of fractional wettability on multiphase flow through porous media, American Institute of Mining, Metallurgical, and Petroleum Engineers (AIME) Transactions, 216-246, USA.

Fischer U., Celia M.A. (1999): Prediction of relative and absolute permeabilities for gas and water from soil water retention curves using a pore-scale network model, Water Resources Research, Vol. 35, No. 4, pp. 1089-1100, USA.

Forsmark T. (2007): Äspö Hard Rock Laboratory (HRL), prototype repository, hydraulic tests and deformation measurements during operation phase, test Campaign 7 - single hole test, SKB IPR-07-02, Clay Technology AB, p. 171, Sweden.

Grant M.A. (1977): Permeability Reduction Factors at Wairakei, paper 77-HT-52, presented at The American Institute of Chemical Engineers (AICHE) and American Society Of Mechanical Engineers (ASME) heat transfer conference, Salt Lake City, Utah, USA.

Grant S.A., Salehzadeh A. (1996): Calculation of temperature effects on wetting coefficients of porous solids and their capillary pressure functions, Water Resources Research, Vol. 32, No. 2, pp. 261-270, USA.

Herklotz M., Uhlig L., Polster M., Jobmann M. (2006): Investigation on the Thermal Hydraulic and Mechanic (THM) Behavior of the Bentonite Barrier by Measurements and Numerical Calculations, MUSTER Annual Report 2005, Deutsche Gesellschaft zum Bau und Betrieb von Endlagern für Abfallstoffe mbH (DBE) Technology, pp. 74, Germany.

Hill M.C. (1998): Methods and guidelines for effective model calibration, U.S. Geological Survey Water-Resources Investigations report 98-4005, p. 90, Denver(Colorado) USA.

Hirschfelder J.O., Curtiss C.F., Bird R.B. (1954): Molecular Theory of Gases and Liquids, John Wiley& Sons Inc., p. 1249, USA.

Hökmark H., Fälth B. (2003): Temperature Buffer Test (TBT) predictive modeling program, SKB document F12.1G-1012125, Sweden.

Hökmark H., Börgesson L., Hernelind J. (2005): Äspö Hard Rock Laboratory (HRL) - Temperature Buffer Test - scoping design calculations, Report No: F12K, SKB IPR-05-07, Clay Technology AB, p.137, Sweden

International Formulation Committee (1967): A formulation of the thermodynamic properties of ordinary water substance, IFC Secretariat, Düsseldorf Germany.

Jobmann M. (2000): Modellgrundlagen und Prognose, hydraulische Modellierungen, Deutsche Gesellschaft zum Bau und Betrieb von Endlagern für Abfallstoffe mbH (DBE), pp. 10-11, Germany.

Kahr G. and Müller-von Moos M. (1982): Wärmeleitfähigkeiten von Bentonit MX80 und von Montigel nach der Heizdrahtmethode, Technischer Bericht, NAGRA NTB 82-06, Institut für Grundbau und Bodenmechanik ETH Zürich, Switzerland.

Kröhn K.P. (2004): Modeling the re-saturation of bentonite in final repositories in crystalline rock, Final Report, GRS-199, Gesellschaft für Anlagen- und Reaktorsicherheit (GRS), pp. 22-24, 106-107, Germany.

Ledesma A., Chen G., Jacinto A. (2005): Temperature Buffer Test (TBT) modeling program Step 2 (extended version), ENRESA Contribution UPC, Barcelona, Spain.

Mualem Y. (1976): A new model for predicting the hydraulic conductivity of unsaturated porous media, Water Resources Research, Vol. 12, No. 3: 513 – 522, Washington, DC, USA.

Montes-H.G., Marty N., Fritz B., Clement A. and Michau N. (2005): Modeling of long-term diffusion-reaction in a bentonite barrier for radioactive waste confinement, Applied Clay Science 30 (2005) 181 – 198, Elsevier, Amsterdam Netherlands.

Montgomery C.D., Hines W.W.(1990) : Probability and statistics in engineering and management science, 3. Edition, John Wiley& Sons, p.732, USA.

OriginLab Cooperation (2007): Origin-8 user guide, p. 545, Northampton USA.

Poeter E.P., Hill M.C., Banta E.R., Steffen M. and Christensen S. (2005): UCODE_2005 and six other computer codes for universal sensitivity analysis, calibration, and uncertainty evaluation, U.S. Geological Survey Techniques and Methods 6-A11, p. 283, USA.

Pruess K., Oldenburg C., Moridis G. (1990): Tough2 user's guide, Lawrence Berkeley National Laboratory, University of California, Berkeley, Version 2.0, p.102, California USA.

Pruess K., Oldenburg C., Moridis G. (1999): Tough2 user's guide, Lawrence Berkeley National Laboratory, University of California, Berkeley, Version 2.0, p.197, California USA.

Rodwell W.R., Harris A.W., Horseman S.T., Lalieux P., Müller W., Amaya L.O. & Pruess K. (1999): Gas migration and two phase flow through engineered and geological barriers for a deep repository for radioactive waste European Commission, EUR 19122 EN, pp. 63 – 73, 101 – 114, Belgium.

Schaap M.G., Van Genuchten M.Th. (2005): A modified Mualem-Van Genuchten formulation for improved description of the hydraulic conductivity near saturation, Vadose Zone Journal 5:27-34 2006, pp. 27-29, Madison USA.

Schneider K. J., Bertig R. (1994): Bautabellen für Ingenieure: Mit europäischen und nationa-len Vorschriften, Werner, Germany.

Schonebeck M., Jobmann M. (2005): Investigation on the Thermal Hydraulic and Mechanic (THM) Behavior of the Bentonite Barrier by Measurements and Numerical Calculations, MUSTER Annual Report 2004, Deutsche Gesellschaft zum Bau und Betrieb von Endlagern für Abfallstoffe mbH (DBE) Technology, pp. 35, Germany.

She H.Y., Sleep B.E. (1998): The effect of temperature on capillary pressure-saturation relationships for air-water and perchloroethylene-water systems, Water Resources Research, Vol. 34, No. 10, pp. 2587-2597, USA.

Sundberg J., Gabrielsson A. (1999): Laboratory and Field Measurements of Thermal Properties of the Rocks in the Prototype Repository at Äspö Hard Rock Laboratory (HRL), SKB IPR-99-17, Clay Technology AB, Sweden.

Sundberg J. (2002): Determination of Thermal Properties at Äspö Hard Rock Laboratory (HRL) - comparison and evaluation of methods and methodologies for borehole KA 2599 G01, SKB R-02-27, Svensk Kärnbränslehantering AB, Sweden.

Thunderhead Engineering (2007): PetraSim User Manual, p.96, Manhattan USA.

Van Genuchten M. Th. (1980): A closed-form equation for predicting the hydraulic conductivity of unsaturated soils, Soil Science Society V.44, No.5: 892 – 898, Madison USA.

Zhang C.L., Rothfuchs T., Jockwer N., Wieczorek K., Dittrich J., Müller J., Hartwig L., Komischke M. (2007): Thermal Effects on the Opalinus Clay, A Joint Heating Experiment of ANDRA and GRS at the Mont Terri URL (HE-D Project), Final Report GRS – 224, Gesellschaft für Anlagen- und Reaktorsicherheit (GRS), pp. 64 – 67, Germany.

LIST OF FIGURES

LIST OF TABLES

NOMENCLATURE

a	Number of the decrements
b	A vector of the estimated parameter values
b'	Value of the parameter which is perturbed
c_1	Empirical constant (N m^{-1})
c_2	Empirical constant (N $m^{-1}K^{-1}$)
c_p (or c)	Specific heat capacity [J kg^{-1} K^{-1}]
c_v	Specific heat capacity at constant volume [J kg^{-1} K^{-1}]
D	Thermal diffusivity [m^2/s]
d	Percent of the perturbation of the parameter for which sensitivities are being calculated (0.90, 0.45 and 0.10 decrements)
d_β^{κ}	Coefficient of binary gas diffusion [m^2/s]
F	Mass [kg m^{-2} s^{-1}] or heat flux [W m^{-2}]
F_β	Mass flux in phase β [kg m^{-2} s^{-1}]
g	Vector of gravitational acceleration [m s^{-2}]
h_β	Specific enthalpy in phase β [J kg^{-1}]
k	Absolute permeability [m^2]
k_x	Intrinsic permeability along the x axis [m^2]
k_y	Intrinsic permeability along the y axis [m^2]
k_z	Intrinsic permeability along the z axis [m^2]
k_{rl}	Relative permeability to the liquid phase [-]
k_{rg}	Relative permeability to the gas phase [-]
$k_{r\beta}$	Relative permeability to phase β [-]
m	Van Genuchten`s notation [-]
n	Number of the simulation time steps
O_{Pcap}	Objective function for absolute capillary pressure [MPa]
P	Pressure [Pa]
P	Pressure of a reference phase (usually taken to be the gas phase) [Pa]
P_0	Gas phase pressure under reference conditions [Pa]
P_0^{-1}	Reciprocal of the gas(air) entry pressure [Pa^{-1}]
P_{cap}	Capillary pressure (suction) [Pa]
$P_{cap,i}$	Measured absolute capillary pressure value [MPa]
$P'_{cap,i}$	Simulated absolute capillary pressure value [MPa]
$P_{cap,\beta}$	Capillary Pressure in phase β [Pa]
P_{max}	Upper boundary for the capillary pressure [Pa]
P_{sat}	Saturated vapor pressure of bulk aqueous phase [Pa]

P_β	Fluid pressure in phase β [Pa]
p	Parameter vector
r	Radial distance [m]
S_{gr}	Residual saturation of the gas phase [-]
S_L	Actual liquid phase saturation [-]
S_{lr}	Residual liquid phase saturation [-]
S_{ls}	Maximum liquid phase saturation [-]
S^*	Effective liquid phase saturation [-]
T	Temperature [K or °C]
T_0	Temperature under reference conditions [K or °C]
u_β	Seepage velocity vector for the phase (or Darcy velocity) [m s^{-1}]
w	water content [%]
$y'(b)$	The value of the simulated variable [MPa]
$y'(b')$	The value of y' calculated using the parameter values in b´ [MPa]
∇	Del operator, gradient

Greek Symbols

α	Ratio of the parameter variation that has influence on the variable (absolute capillary pressure)
α_{Final}	Final value of the related parameter that has influence on the variable
$\alpha_{Initial}$	Initial value of the related parameter that has influence on the variable
β	Pore compressibility [Pa^{-1}]
Δb	A vector in which all values are zero except for the one that corresponds to the variable (absolute capillary pressure) for which sensitivities are being calculated
$\Delta y'$	The change in the simulated value of the absolute capillary pressure [MPa]
θ	Constant fit parameter
λ	Thermal conductivity [W m^{-1} °C^{-1} or W m^{-1} K^{-1}]
λ_{sat}	Saturated(wet) thermal conductivity [W m^{-1} K^{-1}]
λ_{dry}	Dry thermal conductivity [W m^{-1} K^{-1}]
μ_β	Dynamic viscosity of the phase β [Pa.s]
ρ_β	The density of the phase [kg m^{-3}]
σ	Surface tension (N m^{-1})
Φ	Porosity [-]

Indices

0	Reference condition
c (or cap)	Capillary
Final	Final value
g	Gas phase
i	number of the prescribed time steps
Initial	Initial value
L (or l)	Liquid phase
N_{Pcap}	Number of simulated absolute capillary pressure values per simulation session (minimum 1, maximum 4)
NK	Mass components (water, air, H2, solutes…etc.)
r	Relative
β	The fluid phase (liquid or gas)
κ	Component (water or air) (as a subscript)

APPENDIX INDEX

Investigation on the THM Behavior of a Heated Bentonite Barrier by Measurements and Numerical Calculations / MUSTER Final Report

	Locations in model domain		Instrumental positions in block (in-situ values)					
	r (m)	z (m)	Measuring section	Block	Direction	α - Degree	r (m)	z (m)
WB203	0.64	0.25	1.00	C 1	CD	235	0.64	0.25
WB205	0.78	0.25	1.00	C 1	CD	280	0.79	0.25
WB211	0.64	2.23	3.00	R 4	DA	325	0.64	2.27
WB213	0.70	2.23	3.00	R 4	A	10	0.71	2.27
WB215	0.78	2.23	3.00	R 4	AB	55	0.79	2.27
WB218	0.64	3.75	4.00	C 2	CD	235	0.64	3.78
WB220	0.78	3.75	4.00	C 2	D	280	0.79	3.78
WB226	0.68	5.78	6.00	R 10	D	280	0.69	5.81
WB228	0.74	5.78	6.00	R 10	DA	325	0.74	5.81
WB230	0.78	5.78	6.00	R 10	A	10	0.79	5.81
WB233	0.64	7.25	7.00	C 3	CD	235	0.64	7.37
WB235	0.78	7.25	7.00	C 3	D	280	0.79	7.37
UB204	0.78	1.73	2.00	R 3	D	280	0.79	1.75

Appendix 1 **Locations of sensors used for hydraulic calibration in model domain and in the TBT experiment (R=ring, C=cylinder)**

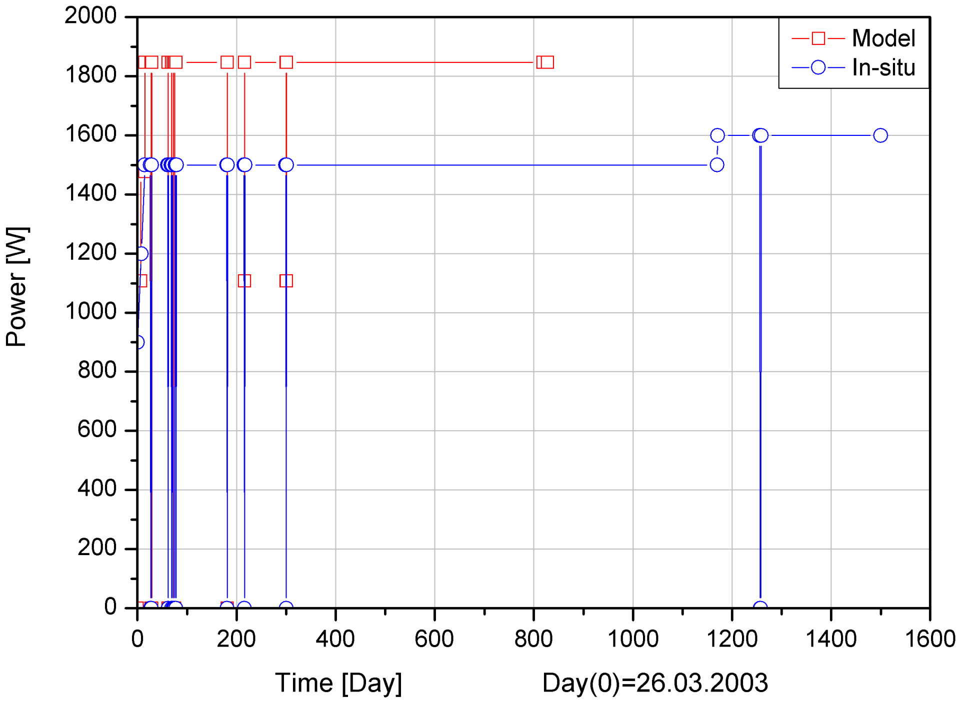

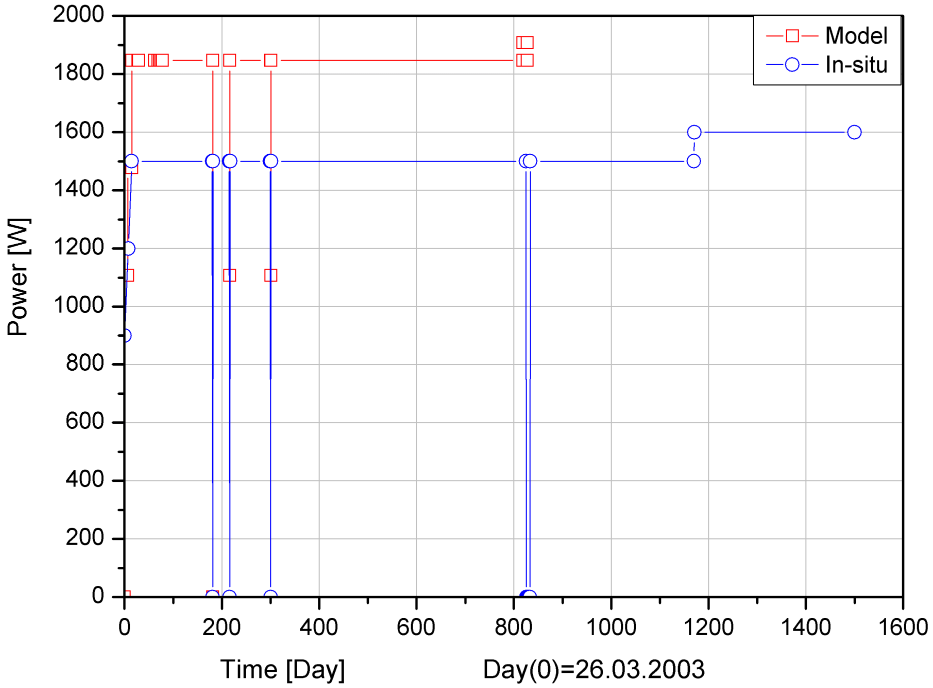

Appendix 2 **Heat output values from experiment and model on heater-1 (upper diagramme) and heater-2 (lower diagramme)**

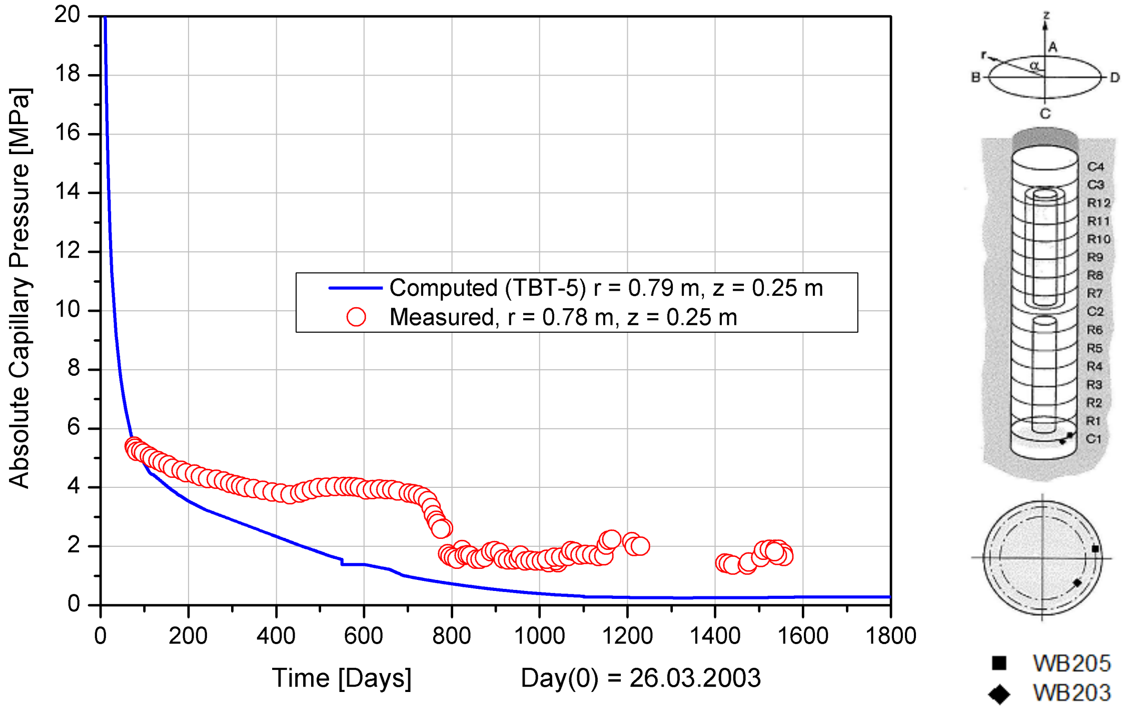

Appendix 3 **Absolute capillary pressure curves at the suction sensor WB-205, comparison of measured and computed values**

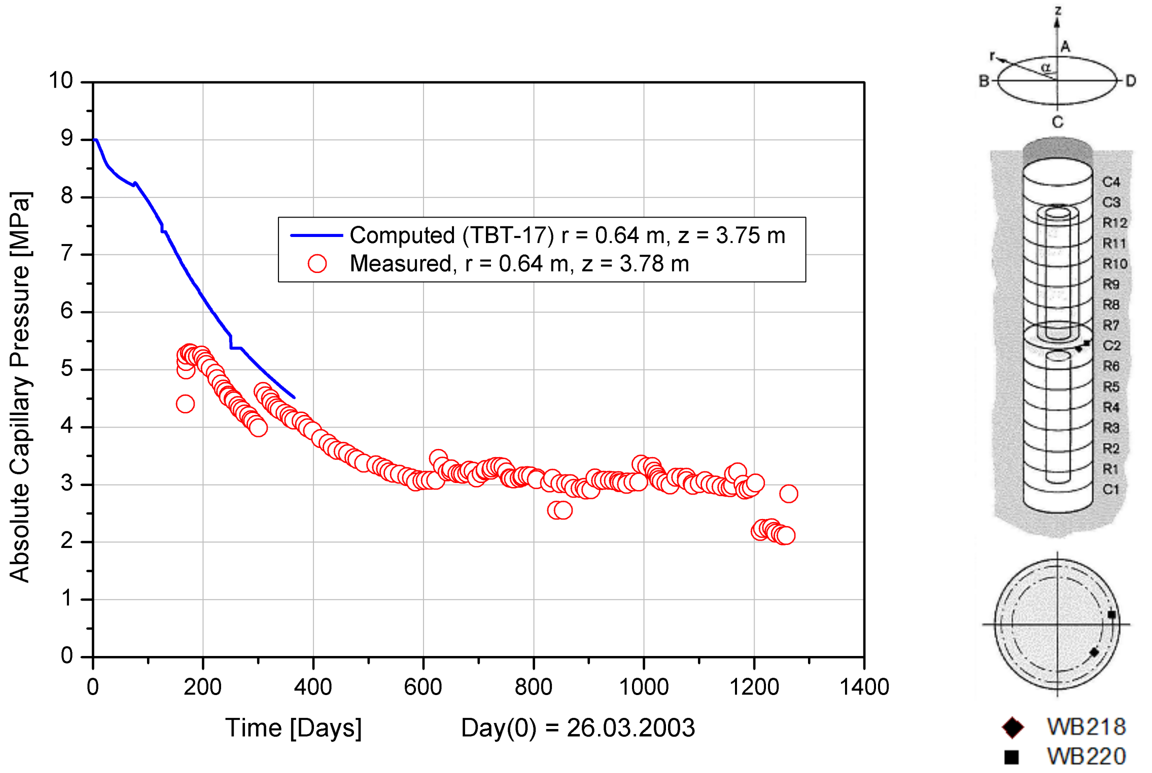

Appendix-4 **Absolute capillary pressure curves at the suction sensor WB-218, comparison of measured and computed values**

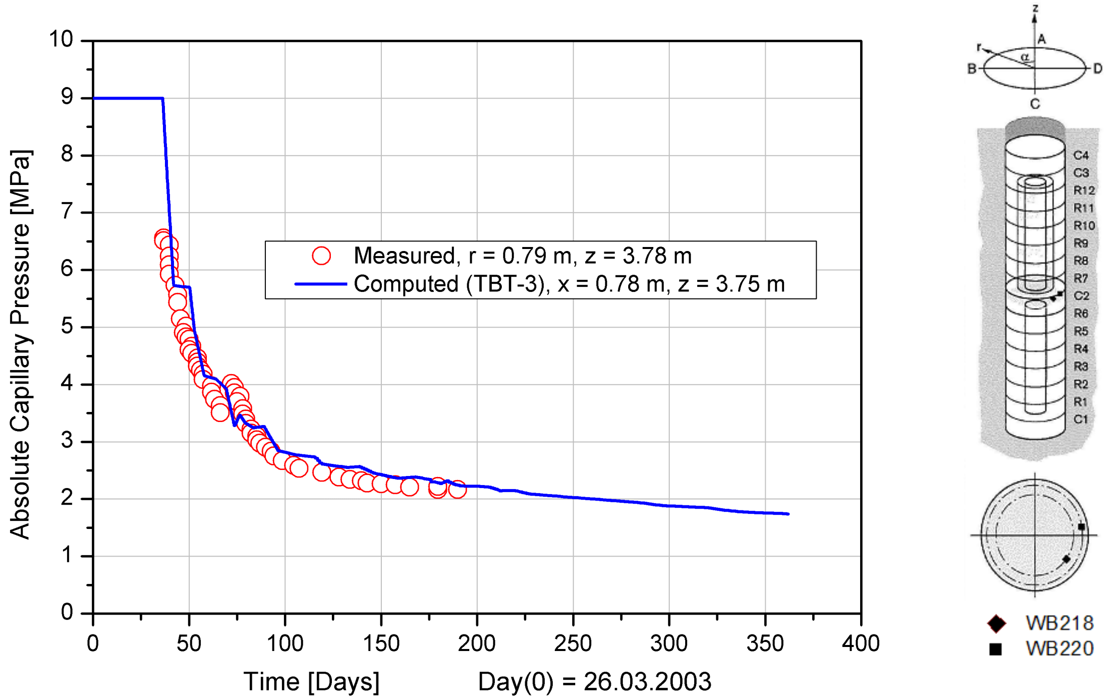

Appendix-5 **Absolute capillary pressure curves at the suction sensor WB-220, comparison of measured and computed values**

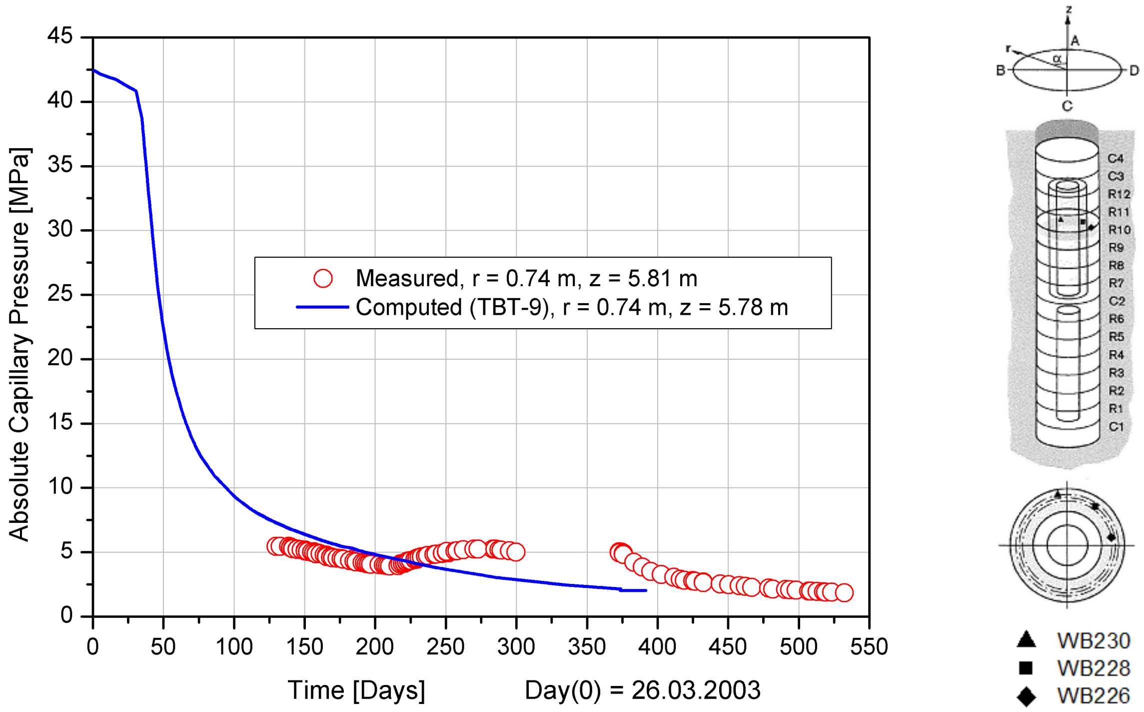

Appendix-6 **Absolute capillary pressure curves at the suction sensor WB-228, comparison of measured and computed values**

After the day 225, suction increased due to a shortage in water supply in ring R9 (ÅKESSON et al. 2007b).

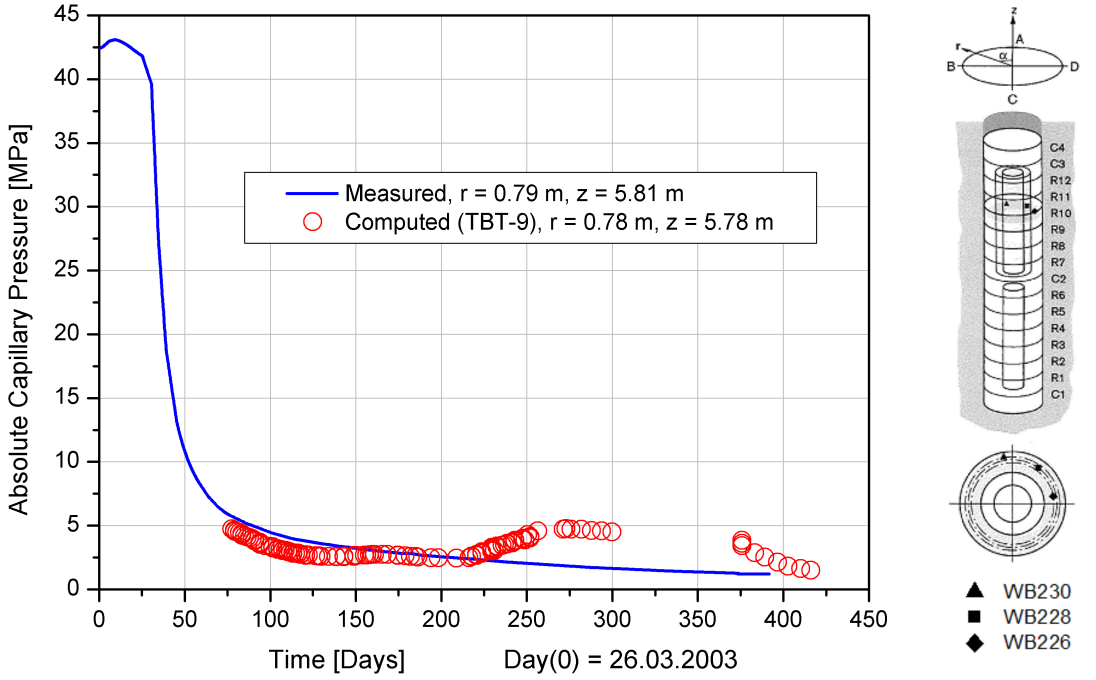

Appendix-7 **Absolute capillary pressure curves at the suction sensor WB-230, comparison of measured and computed values**

After the day 225, suction increased due to a shortage in water supply in ring R9 (ÅKESSON et al. 2007b).

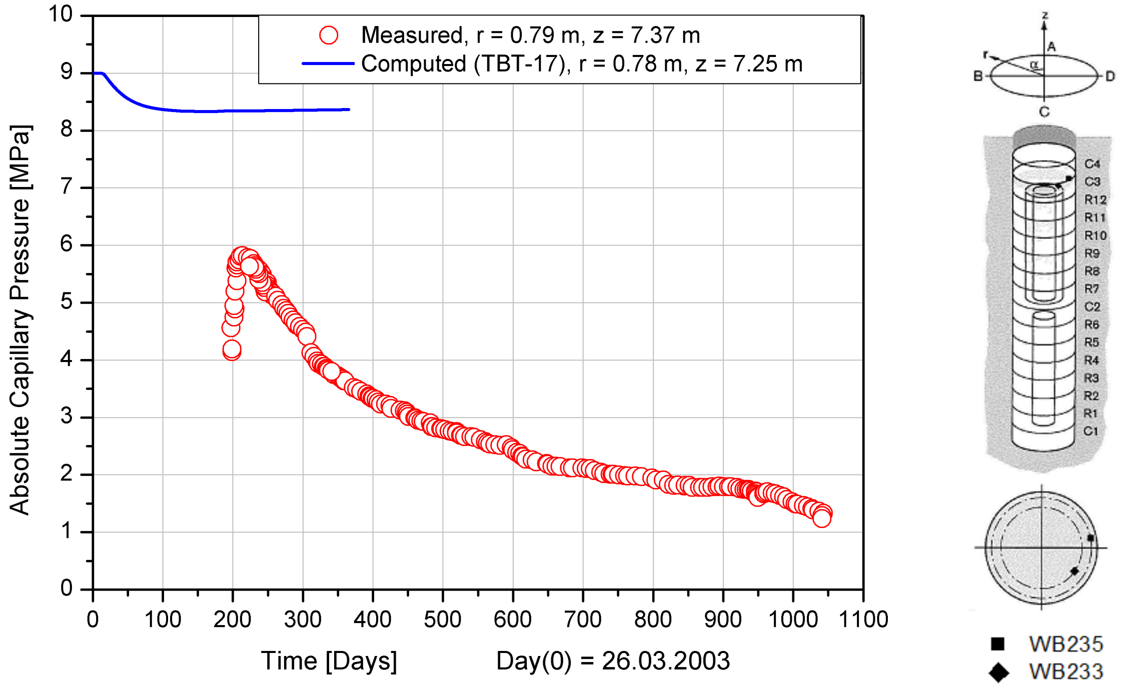

Appendix-8 **Absolute capillary pressure curves at the suction sensor WB-235, comparison of measured and computed values**

The absolute capillary pressure comparison shows a very low prediction of the suction field in the bentonite-1 due to the injection level-2 (fixed boundary condition).

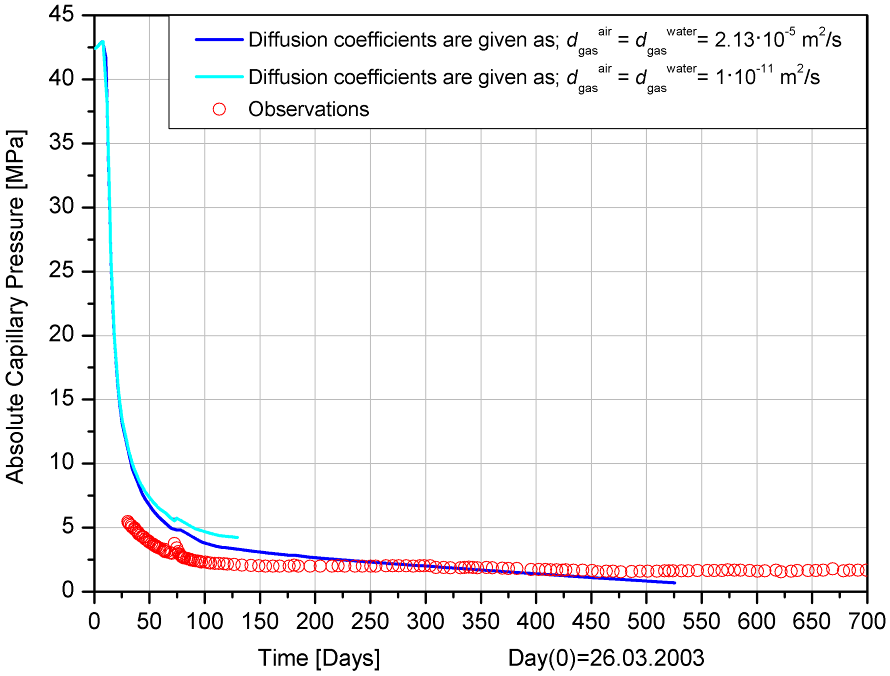

Appendix-9 **Molecular diffusion influence on absolute capillary pressure at the suction sensor WB-215**

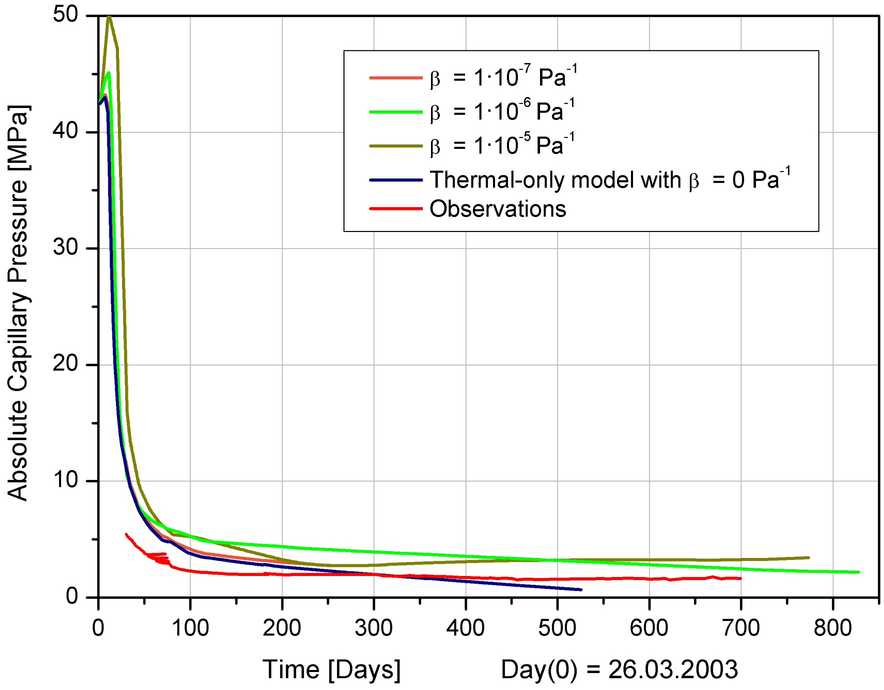

Appendix-10 **Pore Compressibility (β) influence on absolute capillary pressure at the suction sensor WB-215**

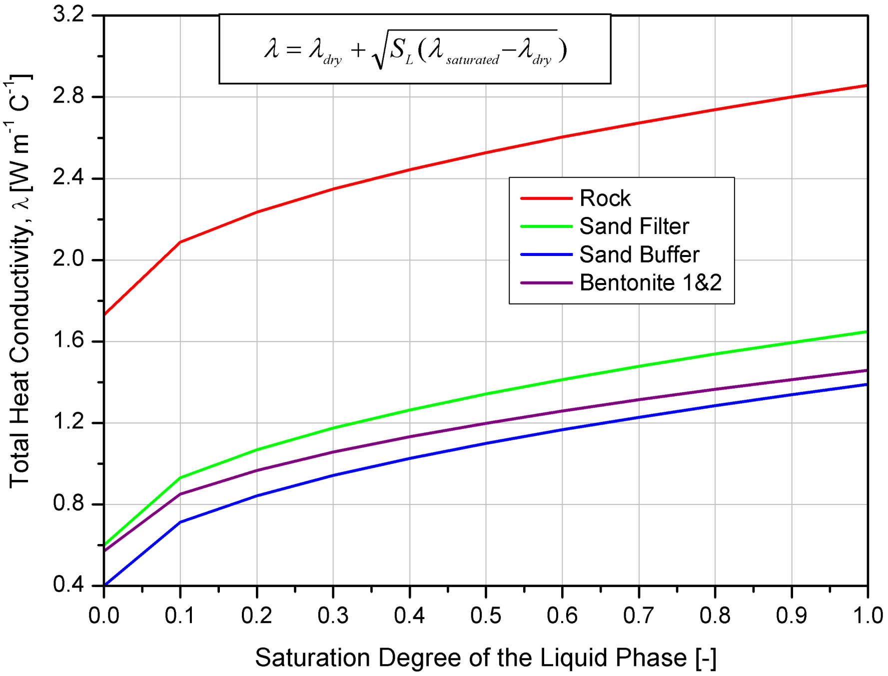

Appendix-11 **The evolution of heat conductivity with liquid saturation for different materials used in the model**

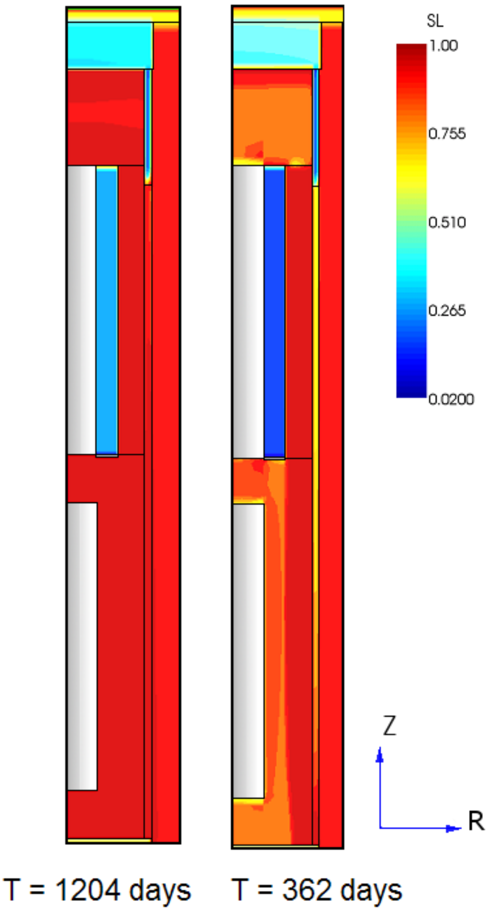

Appendix-12 The liquid saturation isolines at the end of thermal-only (Model0038, left side) and hydraulic calibration (TBT-3, right side) models

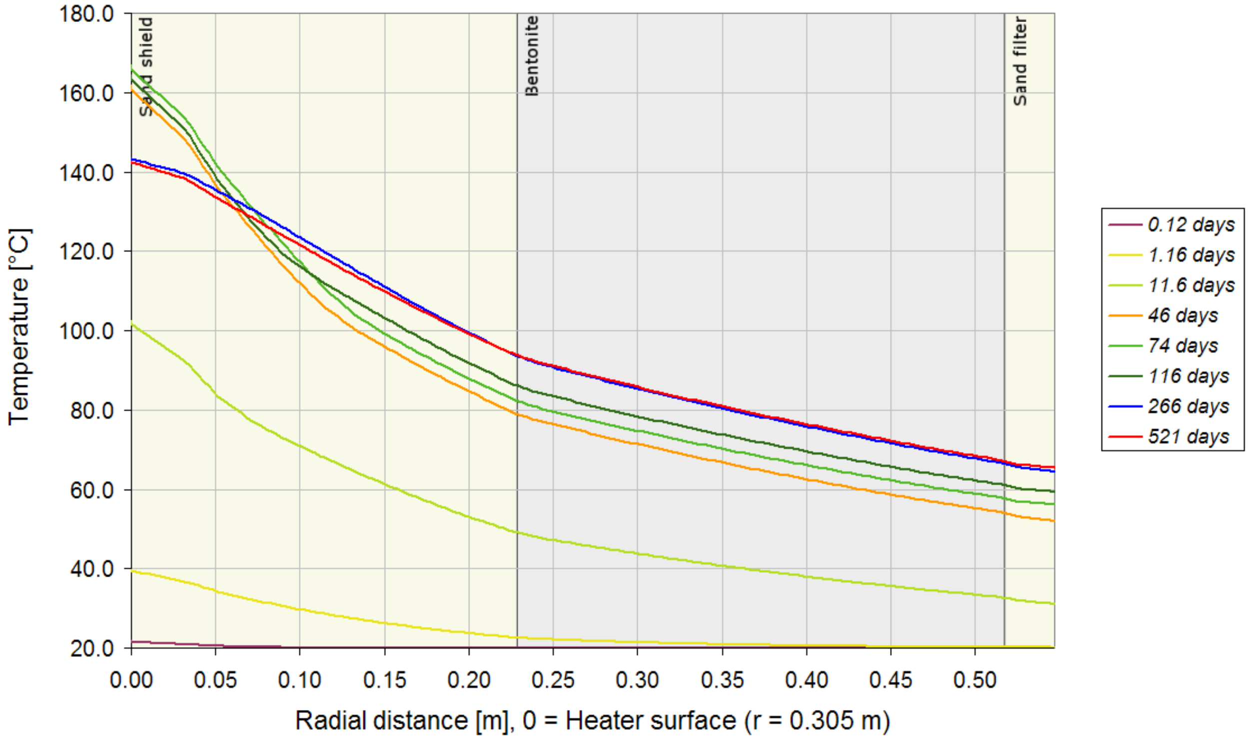

Appendix-13 **Temperature evolution at the prescribed time steps along the scan-line H2 (thermal back analyses)**

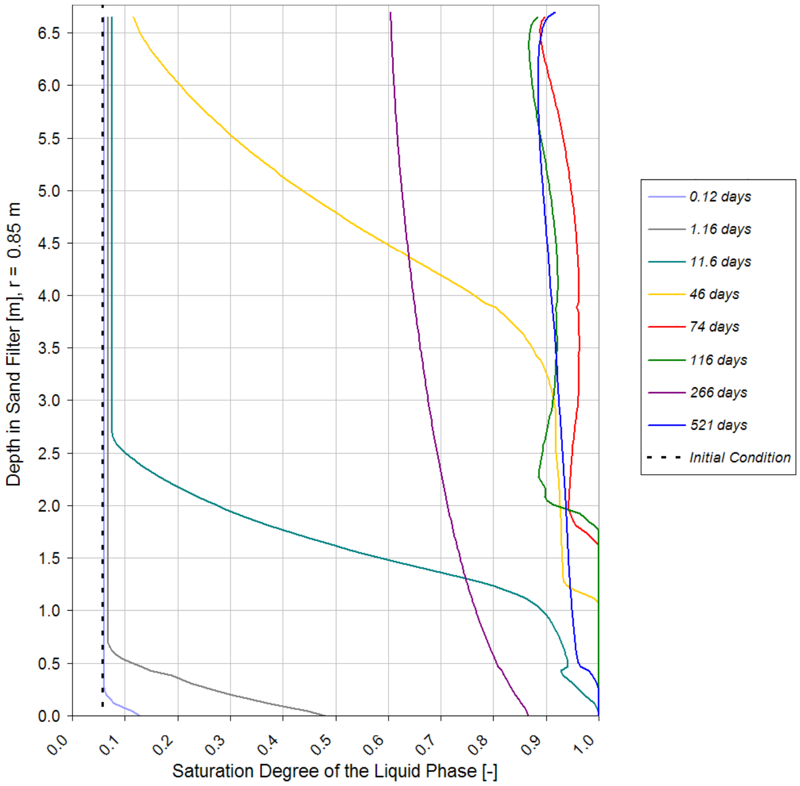

Appendix-14 **Liquid saturation evolution at the prescribed time steps along the scan-line V1 (thermal back analyses)**

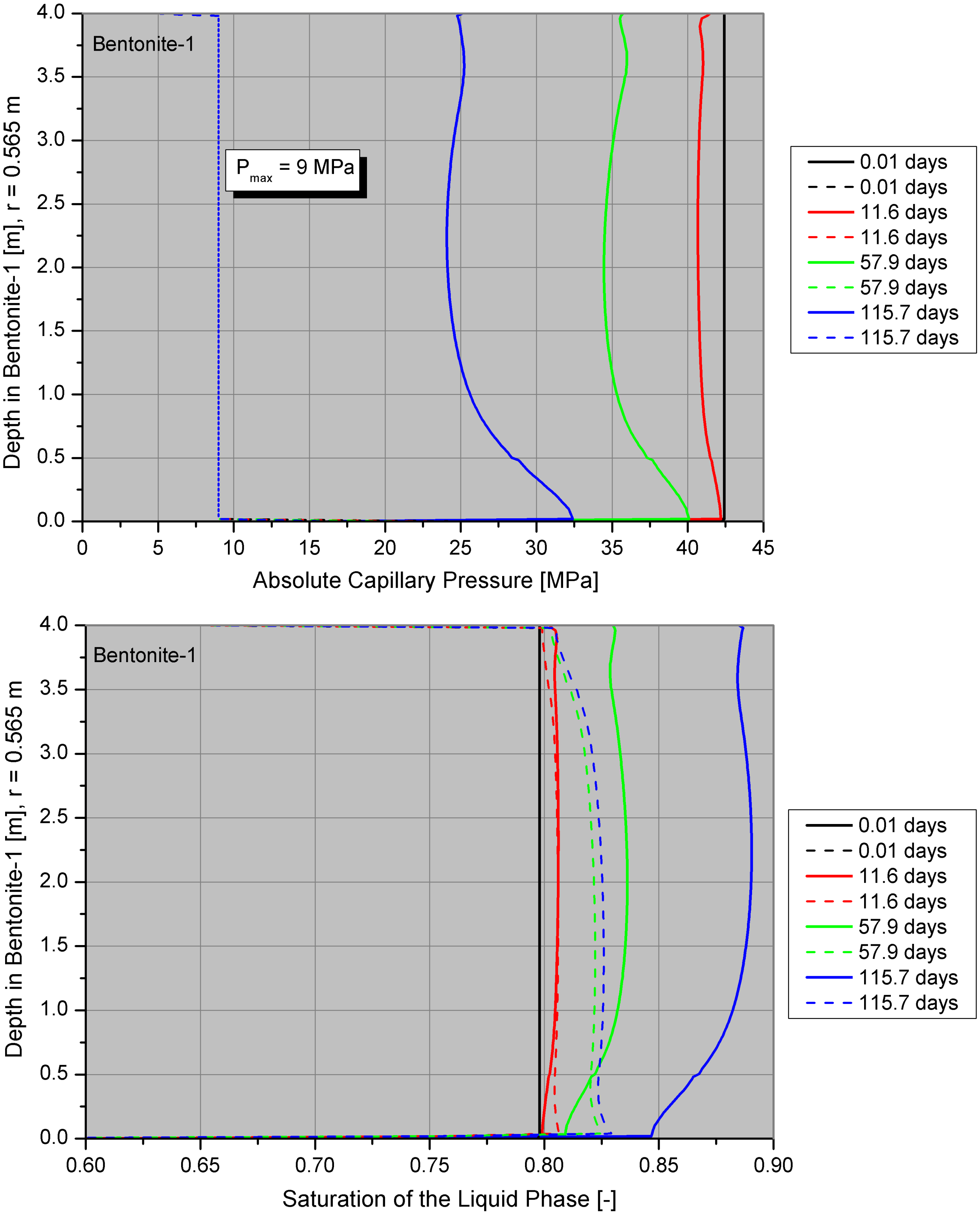

Appendix-15 Absolute capillary pressure and liquid saturation curves along the scan-line V2, comparison of thermal-only model (solid lines, Model0038) with hydraulic calibration model (dashed lines, TBT-3) results for the prescribed time steps (hydraulic back analyses)

In Appendix-15 the figure above, it can be seen that capillary pressure can not exceed the value P_{max}=9 MPa at the model TBT-3.

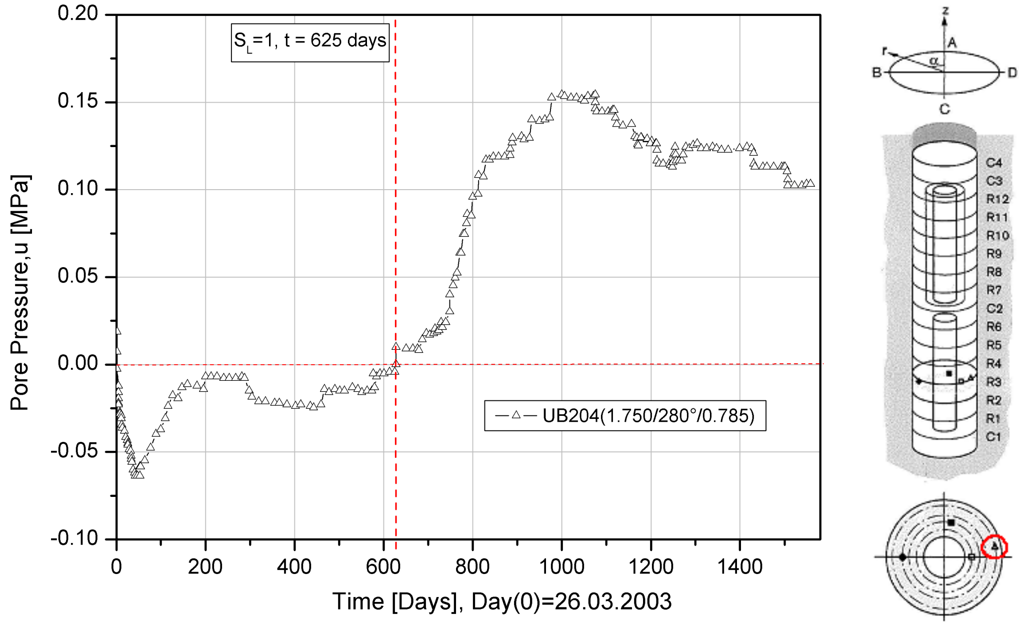

Appendix-16 **Results of pore water pressure sensor UB204, ÅKESSON et al. (2007b)**

Due to ÅKESSON et al. (2007b) when pores are fully-saturated with water (S_L=1), the pore water pressure sensors should give a remarkable pulse above the zero pressure. In figure above, it can be seen that sensor UB204 delivers increasing signal after the day t=625 whereas indicating the full saturation in its vicinity.

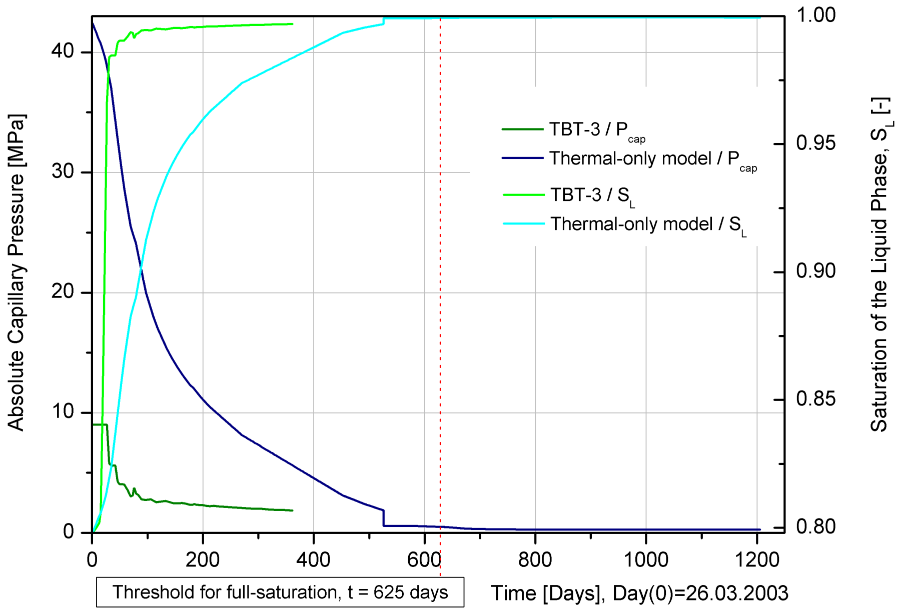

Appendix-17 **Absolute capillary pressure and liquid phase saturation evolution curves at the pore water pressure sensor-UB204. Comparison of results from hydraulic calibration model (TBT-3) and thermal-only model (Model0038)**

The Figure above shows the hydrodynamic dispersion effect. With higher suction, full-saturation front of liquid disperses more.

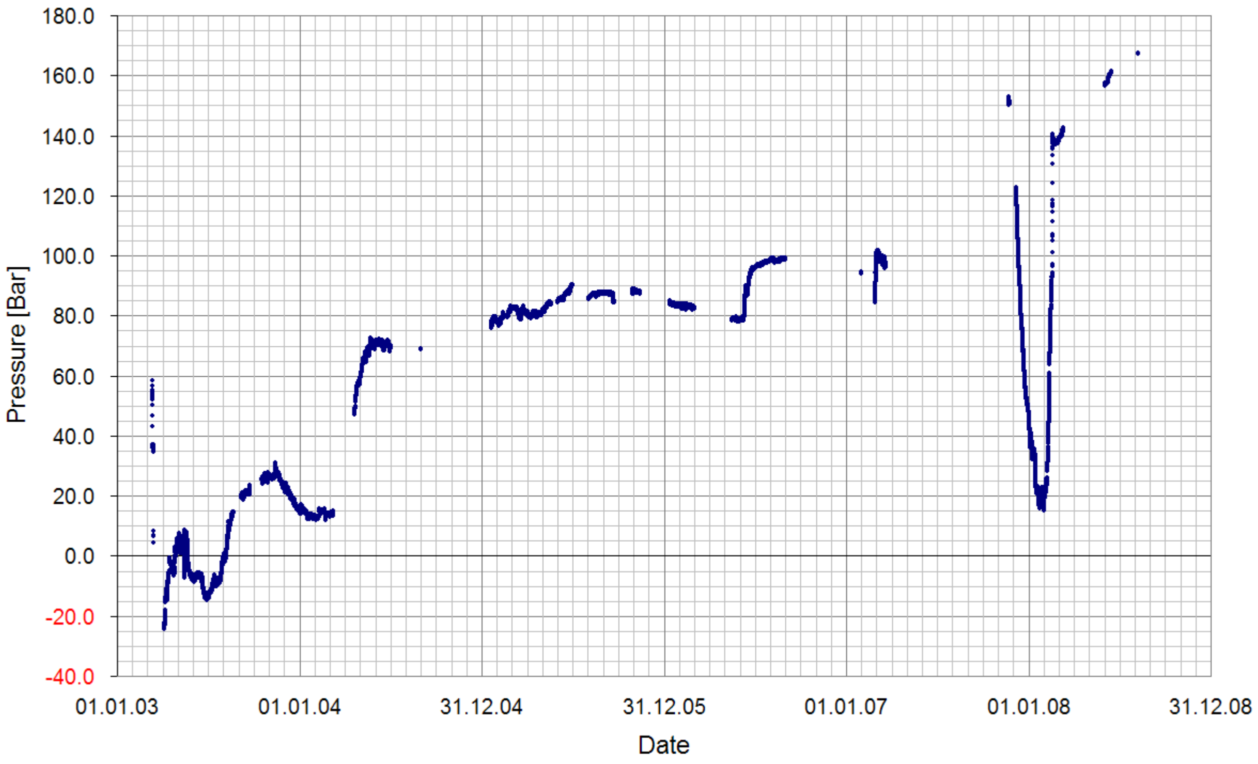

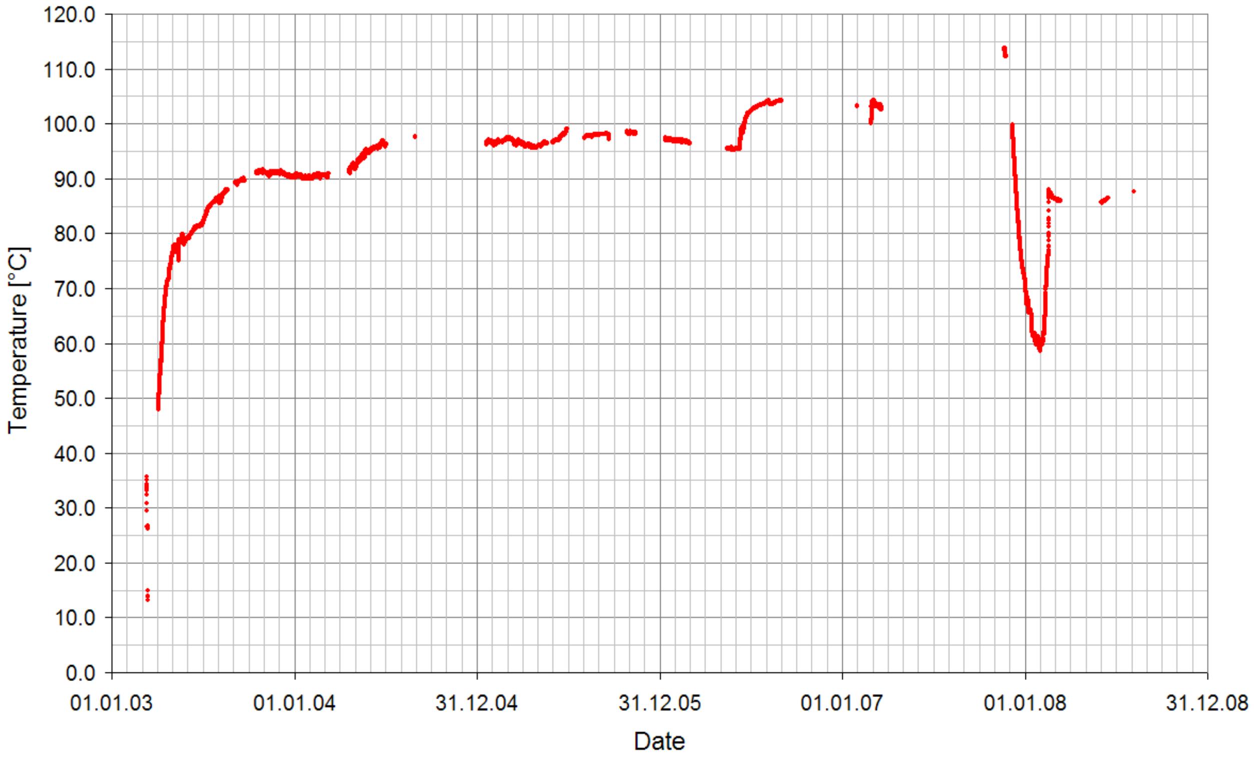

Appendix-18 **Pressure and temperature evolution of the sensor PB231 in ring R9**

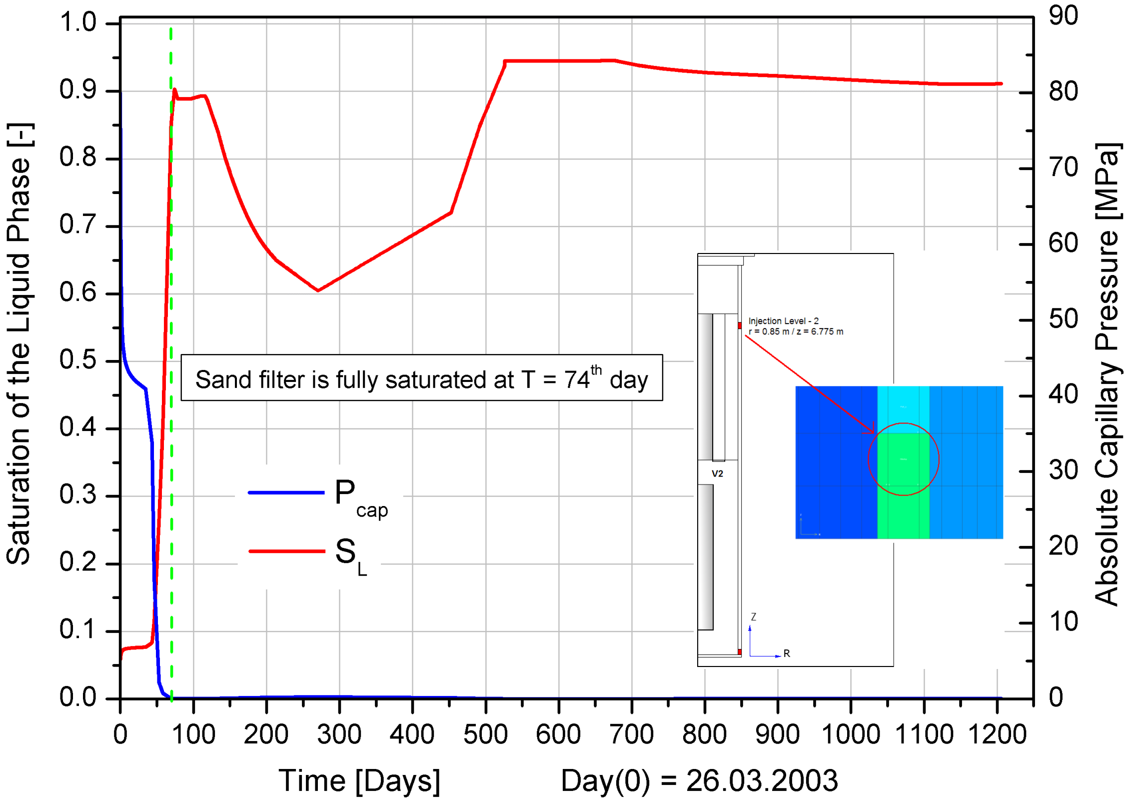

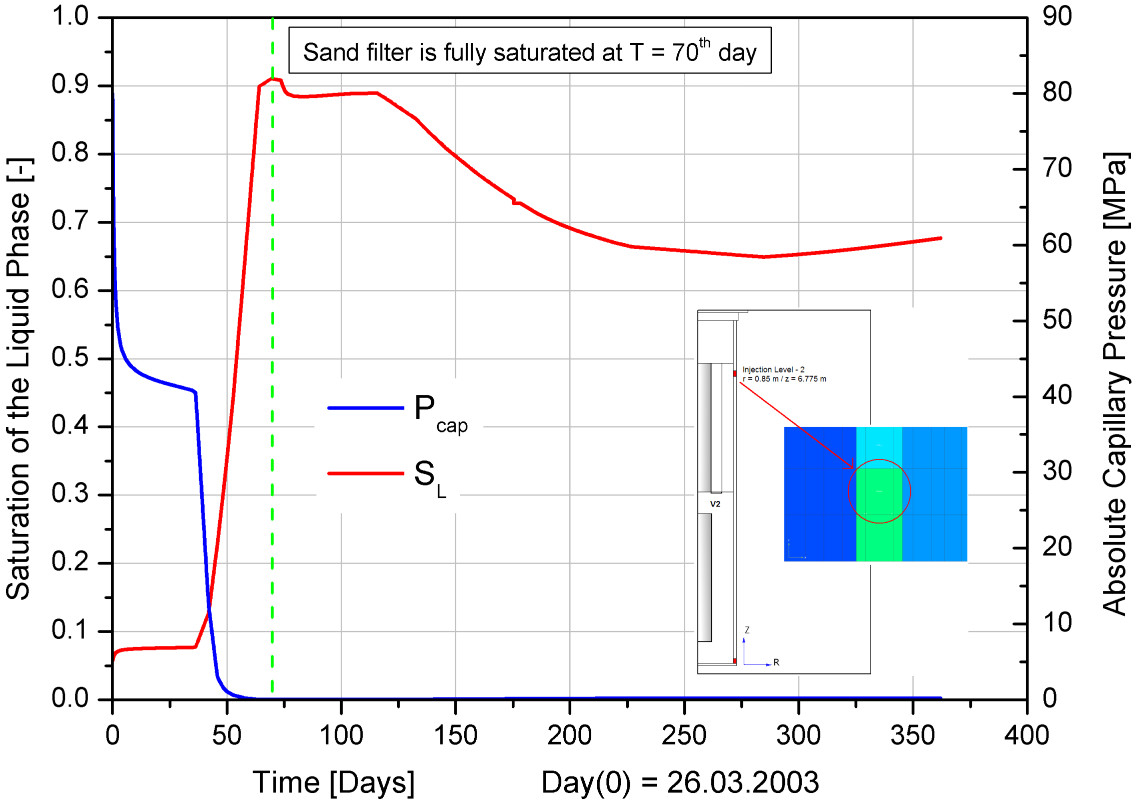

Appendix-19 **Evolution of liquid saturation and absolute capillary pressure at injection level-2 for thermal-only model (Model 0038, the figure above) and hydraulic calibration model (TBT-3, the figure below)**